A Study of the Long-term Behavior of Galactic X-ray Sources with *RXTE*

by

Linqing Wen

Submitted to the Physics Department
in partial fulfillment of the requirements for the degree of

Doctor of Philosophy in Physics

at the

MASSACHUSETTS INSTITUTE OF TECHNOLOGY

February 2001

© Linqing Wen, MMI. All rights reserved.

The author hereby grants to MIT permission to reproduce and distribute publicly paper and electronic copies of this thesis document in whole or in part, and to grant others the right to do so.

Author .....
Physics Department
December 11, 2000

Certified by .....
Hale V. D. Bradt
Professor of Physics
Thesis Supervisor

Accepted by .....
Thomas J. Greytak
Associate Department Head for Education

MASSACHUSETTS INSTITUTE OF TECHNOLOGY
MAR 0 4 2002
LIBRARIES

ARCHIVES

A Study of the Long-term Behavior of Galactic X-ray Sources with *RXTE*

by

Linqing Wen

Submitted to the Physics Department
on December 11, 2000, in partial fulfillment of the
requirements for the degree of
Doctor of Philosophy in Physics

Abstract

I have carried out several investigations of the long-term behavior of galactic X-ray sources using the 4.5-year database of the All Sky Monitor (ASM), and pointed observations made with the Proportional Counter Array (PCA) on board the *Rossi X-ray Timing Explorer* (*RXTE*). I have conducted a systematic search through the ASM data of all the 300 X-ray sources monitored for evidence of periodic behavior. Follow-up investigations are pursued on the discoveries I made in (1) the state transition and orbital modulation of the black hole candidate Cyg X-1; (2) a 4.4-d period in a previously poorly-known X-ray source X 1908+075; and (3) a 98-d period in another previously poorly known X-ray source XTE J1716-389.

In Cyg X-1, I have detected its orbital period in the low-hard state but not in the high-soft state. I show that absorption of X-rays by a stellar wind from the companion star can reproduce the observed modulations in the hard state. To explain the low orbital modulation in the soft-state data, a reduction of the wind density during the soft state would be required. In addition, I have discovered an evolution of the correlation between the 1.5–12 keV X-ray count rate of Cyg X-1 and its spectral hardness during the 1996 spectral state transition. I present a quantitative study of this evolution using both the ASM and the PCA data. Implications of our findings are discussed.

I have discovered a 4.4-d period in the ASM light curves of the X-ray source X 1908+075. We show that this source is the same as a particular Einstein IPC source (1E 1908.4+0730) detected previously. I present a study of this 4.4-d periodic modulation and a discussion of the nature of this system. A 98-d period is discovered in the ASM light curves of another X-ray source XTE J1716-389. I present the results of the investigations on this 98-d periodic modulation using both the ASM and the PCA data. The possible cause of this period and the nature of this system are discussed.

Thesis Supervisor: Hale V. D. Bradt
Title: Professor of Physics

Acknowledgments

I am indebts to my advisor Hale Bradt. I am very lucky to have him as my supervisor not only because he works closely with me on every piece of my thesis work but also because he is very supportative as an advisor. I am very grateful to Al Levine for reading through my thesis carefully and for his great help and advice on completing my thesis. I thank my thesis committee members Saul Rappaport and Fred Rasio for their useful comments and support.

I am honored to work on data mostly from the All-Sky Monitor, the most treasured treasure of Hale and the MIT/*RXTE* group. This has provided me with great opportunities to work with a group of warm-hearted and extremely devoted scientists. Besides science, I have enjoyed lots of stories from them ranging from how Hale sneaked into Navy, Al's scientific demonstration in the high school, how Ron got robbed in Rome, Ed's flat tire in the morning of his discovery of the X-ray millisecond pulsar, and Wei's new parental life.

I shared office, therefore most part of my "official" graduate student life, with graduate students Jim Kiger, Eric Pfahl, Mike Muno, Mark Snyder, and several Urops (especially Goce Zojcheski). Before them, I shared office with Bob Shirey, Don Smith, and Chris Becker, the x-graduate students. I am grateful for great conversations and helps from all of them.

I thank professors Peter Meszaros, Pablo Laguna, Lee Smolin for their earlier inspirations for my study in astrophysics. Special thanks to Wei Cui, Al Levine, Ron Remillard, Ed Morgan, Andrzej Zdziarski, Bram Boroson, Alin Panaitescu, Saul Rappaport, Maurice van Putten, and Ue-li Pen for many interesting discussions and pleasant collaborations. I also thank Peggy Berkovitz for being extremely helpful throughout my life in MIT, especially in difficult times. I thank Kenton Phillips for helping us with the computers.

I would like to thank my parents for having me and their unconditional love. Special thanks to my dearest sister Linying Wen for all her cares and understandings.

At last, words to my dear friends. Without them, life in MIT would have been

hell. Many thanks to all my friends for their heart-warming friendships. In particular, I have had unforgettable times with my four dearest friends from Harvard in yummy home-made dinners, theaters, restaurants, movies, and hours after hours of chatting. Special thanks to Alex Coventry, with whom I shared lots of fun things ranging from playing chess to raising a cat. I also thank my Go teacher Huiren Yang (professional 7 dan) for being willing to take me as his student and his great teaching. Many thanks to MIT Aikido club and MIT Jujitsu club and friends there. I have had infinite fun learning and practicing with them.

At the end, very special thanks to Tschau, Au-Li for his loving support throughout my thesis writing and his willingness in taking the responsibilities for any fault the thesis might consist of and the delay in its submission.

Linqing Wen
Washington, DC
December 8, 2000

Contents

List of Figures

List of Tables

Chapter 1

Introduction

1.1 Overview

Most of the bright galactic X-ray sources are thought to be binary systems that consist of a neutron star or a black hole accreting matter from a companion star (see [79] for a review). The observed X-rays ($E \sim$0.1–200 keV) are believed to come from the release of gravitational energy of the accreted material. In this thesis, we present a study of periodicities observed in galactic X-ray binaries and state transitions in black hole candidates (BHCs). The thesis is based on the surveying data from the All Sky Monitor (ASM) supplemented with data from pointed observations with the Proportional Counter Array (PCA) on board the *Rossi X-ray Timing Explorer* (*RXTE*) spacecraft.

The X-ray binaries are commonly classified according to the mass of the companion M_c as high-mass X-ray binaries (HMXBs) if $M_c \gtrsim 10\mathrm{M}_\odot$ and low-mass X-ray binaries (LMXBs) if $M_c \lesssim 1\mathrm{M}_\odot$. Very few companions have mass in between these values. The measurements of the companion mass are usually based on their spectral types or on the mass function from pulse arrival time measurements if the compact object is an X-ray pulsar. When these measurements are not available, observational characteristics often serve as empirical indicators. For HMXBs, these include 1) strong flaring, and

absorption variability on a timescale of minutes, 2) transient outbursts, 3) X-ray pulsations (with several exceptions), 4) hard 1–10 keV spectrum with a power-law energy index of order 0–1. For LMXBs, these include 1) type I X-ray bursts believed to result from explosive thermonuclear burning on the surface of the neutron star (NS), 2) soft 1-10 keV spectrum with characteristic temperature around 5–10 keV, and 3) less than 12 hr orbital period as higher mass companions will not fit into such small orbits.

The mass transfer from the companion star to the compact object involves wind accretion and overflow of the Roche lobe, the critical equipotential surface of both stars in the co-rotating frame that is connected through the so-called L1 point. In LMXBs, the companion star is often a late type star which does not have a natural wind strong enough to power the observed X-rays. Significant mass transfer thus will occur only if the companion fills its Roche lobe. Wind accretion could also occur if the companion is a giant. In HMXBs, the companion is an O or B star that has a substantial stellar wind. A significant fraction of the wind could be captured and accreted onto the compact object and power the X-rays. Roche lobe overflow can also power these X-ray sources. As the companion star approaches filling its Roche lobe, a wind focused towards to compact object could occur due to the reduced gravity [40].

Classification of the compact object as a black hole candidate (BHCs) or a neutron star (NS) is not trivial. The best way to identify a neutron star is to detect periodic pulsations due to its spin. The most direct evidence for a black hole is that the mass of the compact object is well in excess of $3M_\odot$, as $\sim 3\ M_\odot$ is considered to be the upper limit for a neutron star to resist gravitational collapse into a black hole. In a binary system, the mass of the compact object (or its lower limit) can be determined through the mass function:

$$f(M) = \frac{M_X^3 \sin^3(i)}{(M_X + M_B)^2} = \frac{T}{2\pi G}(V \sin(i))^3, \tag{1.1}$$

where M_X is the mass for the X-ray emitting compact object, and M_B is the mass of the companion star, i is the inclination angle of the binary, $V \sin i$ is the projected orbital velocity of the companion based on Doppler shifts of its spectral lines, and T is the orbital period of the binary.

In the absence of a mass function, the characteristics often used to estimate the possibility that the compact object in a binary is a BH are: (1) ultrasoft spectra; (2) high-energy power-law tail above 20 keV; (3) low-hard and high-soft spectral state transitions similar to those in Cyg X-1 (see section 1.2.2 and Chapter 5); (4) millisecond variability and " flickering" in the low-hard state.

X-rays are strongly absorbed by the Earth's atmosphere; therefore it is impossible to observe X-rays from astronomical sources with ground-based instruments. The first generation technology that enabled significant research to be conducted from above a significant fraction of the atmosphere were sounding rockets and high-altitude balloons. The first celestial X-ray source (other than the Sun), Scorpius X-1, was discovered in 1962 with a rocket-borne detector [41]. The first space satellite devoted entirely to X-ray observations, *Uhuru*, was launched in December 1970. It established the binary nature of galactic X-ray sources and diffuse emission from clusters of galaxies [43]. Over 27 X-ray satellites have been launched since the *Uhuru*. These X-ray missions generally fall into two categories, those with no imaging capability but suitable for high-resolution timing and spectral analyses or for all-sky survey (e.g., *Uhuru*, *RXTE*), and those with imaging capability and often also suitable for high resolution spectroscopy (e.g., *Einstein*, *ASCA*, *Chandra*, and *XMM-Newton*).

Several all-sky monitors have provided years of coverage for many galactic X-ray sources and therefore are excellent tools for the study of the long-term variability of X-ray sources. Among these are the All-Sky Monitor (ASM) (3-6 keV) and the Sky Survey Instrument (SSI) (2.4-19.8 keV) on board *Ariel V* (1974, October–1980 March), the ASM (3–12 keV, a scintillation X-ray detector) on board *Vela-5B* (1969 May –1979 June), BATSE (30 keV–30 GeV) on board *CGRO* (1991 April–2000 June),

and the currently active detector, the ASM (1.5–12 keV) on board the *Rossi X-ray Timing Explorer* (*RXTE*) (1995 December to present). This thesis is based in large part on the *RXTE*/ASM database.

1.2 Intensity Variability

It is well known that galactic X-ray sources exhibit intensity variability on many different time scales and in different ways. On long time scales, for instance, about one third of the $\sim$ 200 known X-ray binaries in our galaxy are detected as transient sources, which often appear on a timescale of a few days, and then decay over many tens or hundreds of days (e.g., [126, 9]). These are believed to be caused by instabilities in the accretion disk, or a mass ejection episode from the companion. On shorter time scales, rapid intensity fluctuations, or quasi-periodic oscillations (e.g., [134]), as well as X-ray bursts or flares (e.g., [124]) are also commonly observed. The fastest variability is manifest in the kilohertz QPOs found recently in LMXBs (see [135] for a review). These undoubtedly represent instabilities or motions of matter in the immediate environments of the compact object.

This thesis will focus on two particular kinds of long-term variability: the periodic behavior of X-ray binaries and state transitions in BHCs, specifically in Cyg X-1. An overview of these two subjects is given in the following.

1.2.1 Periodicities

Periodic modulation of X-rays has been observed in many binary systems (see a general discussion in [148]). The time scales of the modulation range from milliseconds [16] to hundreds of days [33]. The detected X-ray periodicities are known as one of the following three types: (1) a neutron star spin period, (2) an orbital period of the binary system, (3) a super-orbital period that exceeds the orbital period.

The spin periods are found mostly in HMXBs and in a few LMXBs. The pulse

periods range from a few milliseconds to tens of minutes. The accreted mass from the companion is channeled by the neutron star's magnetosphere onto the magnetic poles where it releases its gravitational potential energy in X-rays at the polar surface and forms a hot spot. If the magnetic pole is misaligned with the spin axis, the hot spot will rotate with the neutron star and give rise to periodic emission into the line of sight.

The orbital period has been detected via the study of X-ray light curves in many systems. In the LMXBs, the known orbital periods range from 0.19 hr to 398 hr, with the majority between 1 hr –2 days. The observed properties of the orbital modulation in X-rays depend on the viewing angle. At a low orbital inclination angles ($< 70°$), X-ray orbital periods are rarely observed probably because of the absence of dips or eclipses. At an intermediate inclination, periodic dipping behavior, and in a few cases, brief eclipses of the X-rays by the companion are observed. The dips may be caused by obscuration of materials splashed above the disk plane when the gas stream from the companion hits the accretion disk. For high inclination systems ($> 80°$), X-ray eclipses have been observed in several systems but the number is fewer than might be expected if the systems simply consist of a dwarf companion overflowing its Roche lobe and transferring material to a compact object via a thin accretion disk [63]. To resolve this discrepancy, it has been proposed [91] that the central X-ray source is hidden behind a thick accretion disk rim, but X-rays are scattered via a photo-ionized corona above the disk and can still be seen. The source thus appears extended and partially eclipsed periodically by the bulge at the disk rim caused by the impact of the accretion flow on the disk.

The known orbital periods of HMXBs range from 4.8 hr to 300 days, with the majority above 1 day. All but one of the supergiant systems have nearly circular orbits with periods less than 15 d, whereas most Be star systems have long-period eccentric orbits with periods of several tens or hundreds of days. The orbital periods are detected in X-rays via several effects. These include an eclipse of the X-rays

by the companion, phase-dependent absorption and scattering of X-rays by a stellar wind from the companion, absorption dips caused by impact of the accretion stream upon the disk, and periodic X-ray outbursts due to enhanced accretion caused by the compact object's periastron passage around the Be star.

Superorbital periods have been observed in both HMXBs and LMXBs, they are sometimes quite coherent and sometimes quasi-periodic. In some cases, this periodicity is detected at a high level of significance. A well-established example is the 35 day super-orbital period in Her X-1, much longer than its 1.7 day orbital period or its 1.24 s spin period. A small number of other systems (e.g., LMC X-4 and SMC X-1) show similar modulations. The modulation is mostly likely due to occultation of the X-ray source by a precessing tilted accretion disk (e.g., [65, 77]). It is unclear though why the disk is tilted and what drives the precession. In other sources, the modulation is very weak and/or long compared with the observation duration, so its stability and significance are not well established. Examples include previously reported periodicities from Vela 5-B, such as a 187.5 day period in 4U 1145-61, a 294-day period in Cyg X-1, a 132-day period in GX 304-1 [107], a 199 day period in X 1916-053, and a possible 42 day period in X 1907+09 [108].

The periodic modulations in individual X-ray binaries therefore reveal important information about the geometry, environment, and nature of the system. For instance, the orbital modulations caused by scattering of the X-rays through the wind from the companion star reflect information about the inclination angle, the size of the orbit, and the ionization state and density of the wind (see Chapter 5). A determination of orbital period together with the inclination angle can yield the mass of the compact object (see Equation 1.1). A new period from an unknown X-ray source, once determined to originate from the orbital motion, would establish the binary nature of the system (see Chapter 7). The super-orbital periods reveal the dynamics of a precessing accretion disk (see Chapter 8). A confirmed spin period would indicate that the accreting object is a NS.

Systematic studies of the periodicities of a collection of many sources provide insight on, and illustrate the differences in, the nature of the modulations. Periodicities longer than 1 day have been searched for in low-mass X-ray binaries by Smale and Lochner (1992) [120] using data from Vela 5B. They confirmed the 174.6 day period in X 1820-303 (see also [105]), and reported a non-detection of the 199 day period in X 1916-053, a 77.34 day period in Cyg X-2, and non-detection of long-term periods in 13 other systems. They therefore concluded that long-term cyclic variability is rare in LMXBs. Other examples of systematic periodicity studies can be found in [106] on 8 bright X-ray binaries detected by WATCH/Eureca, and in [108] on 9 galactic X-ray sources in the Aquila-Serpens-Scutum region during 1969–1976 with the Vela 5B satellite.

1.2.2 State Transitions in BH systems

A state transition in Cyg X-1, the first galactic black hole candidate, was first clearly demonstrated by Tananbaum et al. (1972) [127]. The Uhuru data showed that the soft X-ray flux (2–6 keV) decreased by a factor of 4, the average intensity in the 10–20 keV band increased by a factor of 2 within tens of days, and a weak radio source suddenly appeared. This transition in X-rays was later recognized as a transition from the high-soft to the low-hard state, where the high-soft state refers to the state with relatively soft spectrum and high 1.5-12 keV X-ray luminosity, and where the low-hard state refers to the state with relatively low 1.5-12 keV X-ray flux but harder spectrum. Four other such state transitions of Cyg X-1 have been observed during 1975 April–May [50, 53, 116], 1975 November – 1976 February [54], 1980 June [95, 96], and 1996 May–August [25]. They appear to occur randomly in time. Similar state transition behaviors are now known in several other black hole candidates such as GS 1124-68 (Nova Muscae)(e.g. [126]), GS 2000+25 [132], GRS 1915+105 [92], and GX 339-4 [87]. Such transitions are often considered to be related to the change in the mass accretion rate.

The energy spectrum of the low-hard state is characterized by a power-law component with a photon index $\sim$ 1.5–2 and exponential cut-off near 100–150 keV, and sometimes with an additional weak blackbody component with a characteristic temperature of 0.1–0.3 keV. For the high-soft state, the energy spectrum is dominated by an ultrasoft blackbody-like component with a characteristic temperature of 0.5–2 keV (e.g. [126]). In addition, there is often a power-law component with a photon index $\sim$2–3. No exponential cut-off of the power law has been observed; it could extend beyond 500 keV. A summary of the energy spectra of Cyg X-1 in its high-soft, low-hard, and intermediate states can be found in [45].

The timing behavior is found to be distinct for different spectral states (see a review in [134]). In the low-soft state, the rms variability is strong and the power density spectra (PDS) are characterized by a flat top at low frequencies with a high-frequency cut-off around 0.1-1 Hz, and with a power-law component at higher frequencies. In the high-soft state, the variability is relatively weak, and the PDS is characterized by a simple power law component.

Additional states beyond the high and the low states have also been defined with distinct luminosity, spectral, and timing properties. A so-called "very high" state has been reported in GX 339-4 and GS 1124-68 systems, because of its higher 2-10 keV luminosity than the high state observed in the same systems and its peculiar timing behavior (presence of QPOs). An "intermediate" state has also been found in both sources and Cyg X-1 because of its intermediate spectral and timing behavior between the high and low states. They are all believed to be linked to the evolution of the high-soft and low-hard states.

1.3 Role of the *RXTE*

The *RXTE*/ASM, compared with other sky monitors, has relatively good sensitivity (with a threshold sensitivity of $\sim$ 10 mCrab in a day), frequent data sampling

rate (a source is typically observed 10–15 times a day), and more than 4.5 years' of monitoring baseline (Chapter 2). Therefore, compared with the previous periodicity studies [148], we expect from the *RXTE*/ASM: (1) new periodicities to be discovered (Chapter 4), (2) better detections of periods from many systems, and more detailed studies of modulations in different energy bands and in different states (Chapter 5). In addition, with a higher quality database and detections of many more X-ray sources, the *RXTE*/ASM would also be useful for a systematic study of X-ray periodicities (Chapter 4).

Despite theoretical and observational studies, the cause of the state transitions in black hole systems is still unknown (see an overview in Chapter 5). More observational constraints are needed for a full understanding of the transition. Thanks to the alert from the *RXTE*/ASM, there has been a first complete coverage of a state transition episode in Cyg X-1 during 1996 May–August in a broad energy band with the *RXTE*/ASM(1.5–12 keV) and the *CGRO*/BATSE (20–200 keV). Moreover, there have been several snapshots covering the entire episode from a pointed instrument (PCA) on board *RXTE* with high-quality timing and spectral resolution. This allows a comprehensive study of Cyg X-1 and a more detailed characterization of the state transition (e.g., Chapter 6). As the state transition is a common phenomenon among BHCs, a study of a canonical BHC such as Cyg X-1 could lead to a better understanding of other BHCs.

1.4 Thesis Goal and Outline

I joined the *RXTE*/ASM group in MIT as a graduate student in the summer of 1997, 1.5 years after the launch of the *RXTE*. I carried out the first search of the ASM data for X-ray counterparts of gamma-ray bursts and found several candidates in the archival ASM data (see [121]). This later became part of the Ph.D. thesis for then-graduate student Don Smith who had been playing an essential role in this ASM

program. From time to time, I also carried out searches for periodicities in the ASM database. Chapter 4 is a summary of these searches, as well as the results reported independently by others (since the ASM data are publically accessible). During the periodicity searches, I decided to pursue follow-up studies in four cases of three sources (Chapters 5–8) using both the ASM monitoring data and higher quality data from the PCA. Results of three case studies have been published [145, 146, 144] and one is in preparation. In addition, we have succeeded in proposing for *RXTE*/PCA observing times for Cyg X-1 (200 ks), X 1908+075 (80 ks), and XTE J1716-389 (300 ks). Results of the PCA analyses of XTE J1716-389 are included in this thesis. The PCA studies of Cyg X-1 and X 1908+075 will be published later.

In this thesis I study, mainly from an observational point of view, the long-term periodic or quasi-periodic intensity variability in galactic X-ray binaries and spectral state transitions in black hole candidates, specifically in Cyg X-1. The project consists of a global search for periodicities using the *RXTE*/ASM database and the follow-up studies for three individual sources, Cyg X-1 (Chapters 5, 6), X 1908+075 (Chapter 7), and XTE J1716-389 (Chapter 8). The goal for the global periodicity search is to obtain an overall understanding of the characteristics of the periodic modulations in X-ray binaries and to discover new periods. The scientific goals of our study of Cyg X-1 are (1) to explore the observational characteristics of state transition episode, (2) to study the cause of the X-ray orbital modulations and use it to constrain the system parameters, such as the inclination angle of the system, and (3) to explore the environmental radiative process, e.g., scattering and absorption of the X-rays by a dense stellar wind. The goals of the X 1908+075 and XTE J1716-389 studies are (1) to identify the nature of the system, and (2) to study the mechanism that causes the periodic modulations. The data used in these studies are primarily from the *RXTE*/ASM and, in two follow-up case studies, from the pointed instrument *RXTE*/PCA.

The present chapter gives an overview of the project. Chapter 2 describes the

instrumentation of the *Rossi X-ray Timing Explorer* mission and the several observational periodic artifacts introduced by it. Chapter 3 presents the technical aspects of the timing and spectral analyses. It includes methods for detecting the periodicities and correlations, and the basic principles of spectral fitting. Chapter 4 presents a summary of the periodicities detected from the *RXTE*/ASM database.

Chapter 5 presents an overview of the BHC Cyg X-1, and a study of the orbital modulation of X-rays from Cyg X-1 in its hard and soft states with the *RXTE*/ASM data (also published in [145]). We show that absorption of X-rays by a stellar wind from the companion star is able to reproduce the observed X-ray orbital modulations in the low-hard state. However, it can not explain the non-detection of the orbital modulation in the high-soft state. Chapter 6 presents a quantitative study of the flux-hardness correlation of Cyg X-1 during the state transitions with both the *RXTE*/ASM and the PCA data (accepted for publication in ApJ Letter (2000)) [144]. We have found that the correlation shows an interesting evolution during the 1996 episode of spectral state transitions. We discuss the implications of our findings.

Chapter 7 presents a new 4.4 -d period discovered in the X-ray source X 1908+075 from the ASM data (published in [146]). This establishes the binary nature of this previously poorly understood source. We also suggest that X 1908+075 is an X-ray binary with a high mass companion star and that the modulation is caused by the wind from the companion. Chapter 8 presents a new 98-d period discovered from the ASM data of another previously poorly studied source XTE J1716-389. A detailed follow-up study with the *RXTE*/PCA data is also presented. The nature of this system and the mechanism that causes the 98-d periodic dip will be discussed. Chapter 9 presents the conclusion of this thesis.

Chapter 2

The X-Ray Timing Explorer

2.1 Mission Background

The *Rossi X-ray Timing Explorer* (*RXTE*) spacecraft was built at Goddard Space Flight Center (GSFC) and was launched on 1995 December 30 by a Delta II rocket into a circular orbit at an altitude of 580 km corresponding to an orbital period of about 96 minutes, with an inclination of 23 degrees. On board this spacecraft are three X-ray collecting instruments (Figure 2-1): the All Sky Monitor (ASM), built (proudly) at MIT by the *RXTE* group (PI: Professor Hale Bradt), the Proportional Counter Array (PCA) built at GSFC (PI: Dr. Jean Swank), and the High Energy X-ray Timing Experiment (HEXTE), built at UCSD (PI: Dr. Richard Rothschild). Data from the PCA and ASM are processed on board by the microprocessor-based electronic package, the Experiment Data System (EDS), also built (again proudly) at MIT. Data links are established through NASA's Tracking and Data Relay Satellite System (TDRSS), beamed to a ground station at White Sands, New Mexico, then to GSFC. After nearly five years of operation, the spacecraft is still functioning well at the time of this writing.

The scientific strength of the *RXTE* lies in its capability of measuring variability over time scales ranging from milliseconds to years. This is aided by its moderate

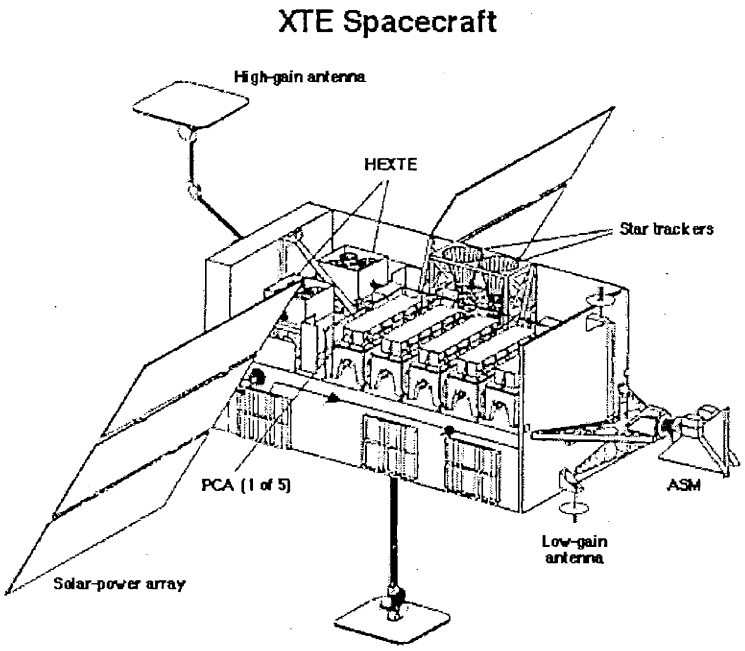

Figure 2-1 The *RXTE* Spacecraft.

energy resolution and good sensitivity. On short time scales, the PCA has made unique discoveries of kilohertz QPOs in low mass X-ray binaries (e.g. [135]), a millisecond X-ray pulsar [16] and numerous contributions to the understanding of the spectral and timing behavior of black hole and neutron-star systems (e.g., [92, 28, 113, 78]). On longer time scales, the ASM on board has discovered numerous transient sources [9], monitored over 100 persistent X-ray sources for the past five years, and localized over a dozen X-ray counterparts of gamma-ray bursts [121]. Because of their key roles in the development of the *Rossi X-ray Timing Explorer* (*RXTE*), Professor Hale Bradt of MIT and Dr. Jean Swank of GSFC/NASA were awarded the 1999 Rossi Prize from the High Energy Astrophysics Division of the American Astronomical Society (AAS).

This thesis work is mainly based on observations from the ASM aided with data from the PCA. The rest of this chapter therefore focuses on the capability of the ASM and the relevant observational artifacts introduced into the data by it. A brief introduction to the instrumentation of the PCA is also given.

2.2 The All Sky Monitor

The All-Sky Monitor (ASM) on board *RXTE* [10] has been monitoring the sky routinely since 1996 March. It consists of 3 Scanning Shadow Cameras (SSCs) on one rotating boom with a total net effective area of 90 cm^2 (180 cm^2 without masks) (Figure 2-2). Each SSC consists of a 1-dimensional coded mask and a 1-dimensional position-sensitive proportional counter (PSPC). Two of the units view perpendicular to the rotation axis and are each rotated by $\pm 12°$ relative to the rotation axis. The third SSC unit views along the axis of rotation and surveys one of the 2 poles not scanned by the other two SSCs. A motorized drive will rotate the three SSC's from field to field in 6° steps. At each resting position, a $\sim$ 100-s exposure of the X-ray sky will be made (90 s steady exposure); a complete rotation is thus completed in about

one orbit ($\sim$ 100 min). The ASM rotation axis shifts every time the XTE spacecraft is reoriented to point the PCA and HEXTE to a new target. Normally, during each orbit, $\sim$80% of the sky will be surveyed to a depth of 20 mCrab. In one day, the limiting sensitivity becomes $\sim$ 15 mCrab at 3σ for a cataloged source. A source is typically observed 10–20 times a day with uneven data sampling in time.

Each SSC detector is a sealed positional sensitive proportional counter (PSPC) filled to 1.2 atm with xenon-CO_2. Each PSPC contains 8 resistive anodes, which are aligned perpendicular to the direction of the coded mask slits. The steel walls of the counter are held at -1800 Volts relative to the anodes. When X-rays penetrate through the window, they interact with gas atoms via the photoelectric effect, with the immediate release of a primary photoelectron. The photo-electron releases its energy through ionizing more atoms. The resulting electrons are accelerated toward the anode. Near the anode, they gain enough energy between collisions to cause further ionization along the path. The resultant avalanche of electrons is collected on the anode. The approximate total energy is indicated by the amplitude of the pulse. The relative amounts of current measured at each end of the anode reflect the location of the impact site of the avalanche. In this manner, the impact location along each anode for each incident X-ray photon is recorded. The sensitivity of the ASM is limited to the energy range of 1.5–12 keV, caused by the absorption of the low energy photons by the beryllium window and reduction of the interaction cross-section of X-rays with the gas atoms at higher energies. The photon energies are recorded in three channels: 1.5–3 keV, 3–5 keV, and 5–12 keV.

The field of view (FOV) of a single SSC is $6^\circ \times 90^\circ$ FWHM. A 90-s integration of X-ray photons from a point source yields a shadow pattern of the coded mask on the anodes, displaced according to the direction of the incident photons (Figure 2-3). The 1-mm elements in the mask pattern yield a moderately high angular resolution of 0.2° in the narrow direction of the SSCs. The six different mask patterns along the long direction of the SSCs (Figure 2-2) provide a crude angular resolution of 15°

in this direction for the weak sources. For one SSC, a faint source near the detection threshold could thus be located with one SSC within an accuracy of $0.2^\circ \times 15^\circ$. A very bright source could be located to an accuracy of $3' \times 30'$. In this manner, a line of position of a source is obtained. The crossed fields of the two SSC units provide an angular resolution of $0.2^\circ \times 1^\circ$ for a weak source and $3' \times 15'$ for a $\sim 5\sigma$ detection. This could be reduced to $3' \times 3'$ by a spacecraft maneuver. With high-statistics detections, precisions $< 1'$ should be attainable.

A linear least squares fit to the shadow patterns cast by X-rays from a source with known position over a 90-s observation by one of the three cameras of the ASM yields the source intensity in the three energy bands. The intensity is usually given in units of the count rate expected if the source were at the center of the field of view in one of the cameras; in these units, the 1.5–12 keV Crab nebula flux is about 75 ASM ct/s. The estimated errors of the source intensities include the uncertainties due to counting statistics and a systematic error taken to be 1.9% of the intensities. In the present analysis, we have used source intensities of 90-s time resolution derived at MIT by the *RXTE*/ASM team. A detailed description of the ASM and the light curves can be found in Levine et al. (1996) and Levine (1998).

2.3 The Proportional Counter Array

The PCA [62] consists of an array of five identical sealed and collimated proportional counter units (PCUs) with a total collecting area of 6250 cm^2. It covers an energy range of roughly 2–60 keV with a moderate energy resolution of $\delta E/E < 18\%$ at 6 keV with 255 energy channels. The 1° FOV (FWHM circular) of the hexagonal collimators yields a source confusion limit at 0.1 mCrab at 2–10 keV. The Crab nebula will yield 8700 ct/s at 2–10 keV and 1200 ct/s at 10–30 keV in the PCA. The PCA is capable of detecting sources down to a flux level of a few mCrab and is much more sensitive than the ASM. The data system can tag the relative time of arrival of each

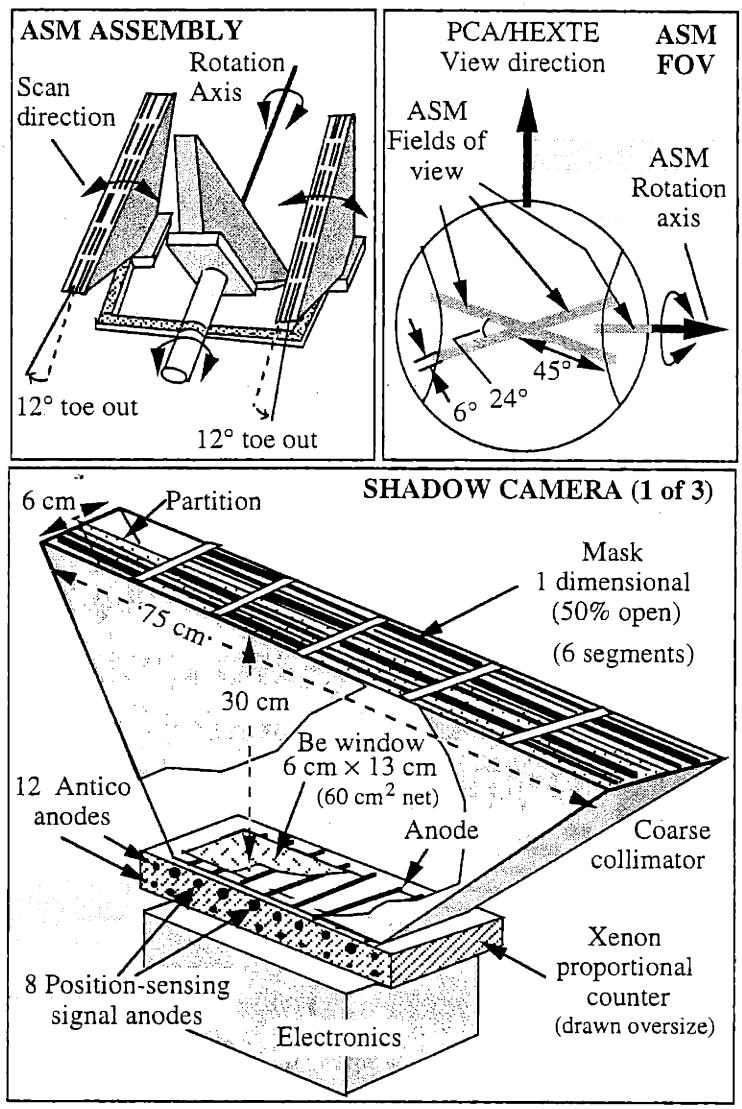

Figure 2-2 The All Sky Monitor Assembly and the Cameras.

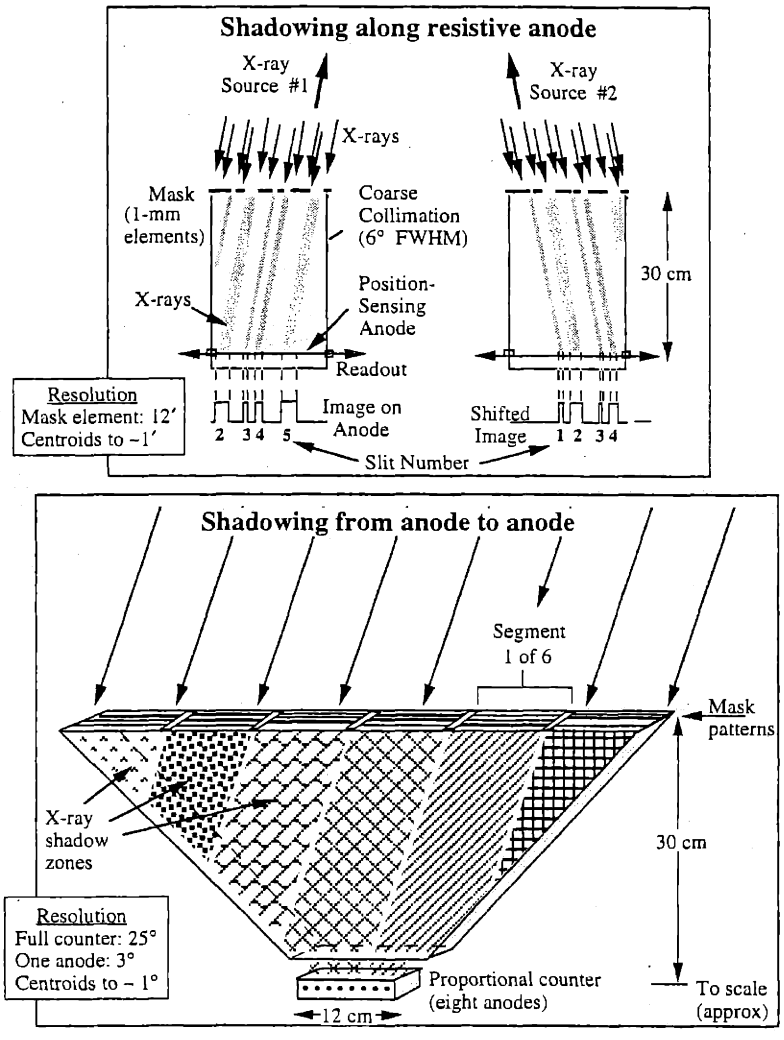

Figure 2-3 The X-ray Shadowing in the ASM Cameras.

event with a precision of 1 μs. The absolute time accuracy is maintained by the spacecraft to better than 1 ms. Although the PCA has no imaging capability, the collimator limits the field of view to 1° FOV (FWHM circular).

The capabilities of the PCA are well-suited for studies of fast variability ($\sim$ 1 ms–1000 s) and energy spectra with moderate energy resolution. A typical observation in our studies lasts a few kiloseconds. To avoid breakdown, the high voltage was regularly turned off for three PCUs. Therefore only a subset of the five PCUs were turned on for each observation, and the number of the PCUs that were turned on varied from observation to observation.

2.4 Observational Artifacts

In practice, the ASM data sampling rate is modulated via several effects. On time scales longer than 1 hr, these effects include the orbit of the satellite, occultation of the FOV by the Earth, the South Atlantic Anomaly (SAA) passage of the satellite, spacecraft maneuvers, the limited rotation range of the ASM drive assembly, and sometimes the constraints caused by the fact that PCA observations could concentrate in one part of the sky. Each of these can yield artifacts in the periodograms used to search for intrinsic periodicities from X-ray sources. The sampling rates are apparently modulated by the $\sim$ 100 minute orbit of the spacecraft. In addition, up to 6 of the 14–15 orbits per day of the *RXTE* satellite will pass through the SAA high particle flux areas, which is the nearby portion of the Van Allen Belt. No data will be sampled during the passage which could last up to 20 minutes for each pass. The 1-d^{-1} rotation of the earth causes the SAA area to periodically move through the satellite's orbit. This therefore will modulate the sampling rate at nearly a 1-d period.

The sampling rate of the ASM is also affected by the presence of the Earth and the Sun in the viewing directions. Sources not near the orbit poles will suffer Earth

occultation for typically about 30 minutes for each 100 minute satellite orbit. The ASM would have to be turned off when the sun is in the FOV. Also, the PCA will not point closer to the Sun than 30°, which constrains the rotation axis of the ASM and therefore its sky coverage. This results in ASM data gaps once a year for sources near the ecliptic plane, each of which lasts typically $\sim$ 20 days. The effect of the high noise produced is often still obvious near the gap in the ASM light curves of X-ray sources observed. Also, when the sun is in the opposite viewing direction to the source observed, contaminations in the ASM data have been found; these are likely caused by the backscattering of solar X-rays off the Earth's atmosphere and the instrument. These cause a modulation in the data sampling rate with a $\sim$182 d or a $\sim$365 d period.

The Earth's oblateness perturbs the $\frac{1}{r}$ gravitational potential and has noticeable effects on the orbit of the satellite. There is a regression of the line of the nodes, where the equatorial plane intersects with the plane of the satellite orbit, caused by the torque induced on the orbit. For *RXTE*, the period of regression of the line of nodes is about 53 days and the period of the precession of the orbit (perigee) is 30.2 days. The former has a major effect on the data sampling as it affects the portion of the sky the satellite views. The latter has little effect as the orbit is essentially circular.

Chapter 3

Analysis Techniques

This thesis involves timing and spectral analyses of X-ray photons. The timing analyses consist of searches for periodic signals, correlations between two data sets, and characteristics of the power density spectra. The spectral analyses consist of searches for the best-fit physical models to the energy spectra and the tracking the evolution of the model parameters with time and flux.

In this Chapter, we present the methods used.

3.1 Timing Analyses

We mainly used the periodogram described below for timing analyses in the frequency domain. A classical periodogram is calculated based on the discrete Fourier Transform (DFT), which can be defined for an arbitrarily sampled data set $x(t_j)$, $j = 0, ..., N-1$ as

$$P(\omega) = \frac{1}{N}|\sum_{j=1}^{n} x(t_j)\exp(-i\omega t_j)|^2 = \frac{1}{N}[(\sum_j x_j \cos\omega t_j)^2 + (\sum_j x_j \sin\omega t_j)^2]. \quad (3.1)$$

The idea is that if there is a sinusoidal signal of frequency ω_0 present in the data, it would resonant with the $\exp(-i\omega t_j)$ term at and near $\omega = \omega_0$ and yield a large

power $P(\omega = \omega_0)$. At other values of ω, it would generate randomly positive and negative numbers and the power would be very small. When the sampling times t_j are equally spaced, Equation 3.1 can be quickly evaluated using a Fast Fourier Transform (FFT) at frequencies $\omega_n = 2\pi n/T$ $(n = 0, N/2)$, where T is the total duration of the observation.

The signal-to-noise ratio of the power at the signal frequency in a periodogram increases with the number of data points N and the signal-to-noise ratio of the signal. For data consisting of a sinusoidal wave with an amplitude of X_0, frequency ω_0, and a random noise with variance of σ_0^2, the expected signal-to-noise ratio of the power P_X/P_R in the periodogram defined in Equation 3.1 is:

$$P_X/P_R = N(X_0/(2\sigma_0))^2. \tag{3.2}$$

The statistical behavior of the periodogram is simple and well-known for evenly sampled data (see the FFT method in subsection 3.1.2). The most important result is that if a set of time series data $x(t_j)$ $(j = 1, n)$ consists of pure Gaussian noise, the powers P_j are exponentially distributed. The analogous results for unevenly-sampled data were first derived by Lomb (1976) [83] and later developed by Scargle (1982) [119, 104]. They proposed a slightly modified periodogram, the Lomb-Scargle (L-S) periodogram, which has the same exponential distribution as in the evenly-sampled case (see next subsection). We used the periodogram to detect periodicities in the ASM data mostly because of its simple statistical behavior, which would allow relatively reliable evaluation of the probability of a spurious detection.

3.1.1 The Lomb-Scargle Periodogram

The Lomb-Scargle (L-S) periodogram is defined for a set of time series data $x(t_j)$ $(j = 1, n)$ as

$$P(\omega) = \frac{1}{2\sigma^2}[\frac{[\sum_j x(t_j)\cos\omega(t_j-\tau)]^2}{\sum_j \cos^2\omega(t_j-\tau)} + \frac{[\sum x(t_j)\sin\omega(t_j-\tau)]^2}{\sum_j \sin^2\omega(t_j-\tau)}], \tag{3.3}$$

where ω is the frequency, σ^2 is the variance of the data points $x(t_j)$ (with zero mean), and τ is defined by

$$\tan(2\omega\tau) = \sum_j \sin 2\omega t_j / \sum_j \cos 2\omega t_j. \tag{3.4}$$

It is easily shown from this equation that if t_j becomes $t_j + T_0$, then τ becomes $\tau + T_0$; hence T_0 cancels out in the arguments $\omega(t_j - \tau)$ in Equation 3.3. Therefore the variable τ ensures the time-translational invariance of the periodogram. That is, the power calculated in Equation 3.3 would be the same regardless of the phase of the model sinusoidal signal.

The normalization terms in the denominator of Equation 3.3 were chosen in such a way that if t_j is taken to be evenly spaced (τ=0), this periodogram is reduced to the classical periodogram (Equation 3.1) with even data sampling. The normalizations also ensure that if x_j is Gaussian noise, the variances of the two terms in the summation would be the same. This way the powers are summations of the squares of two normal variables with the same variances and thus follow the exponential distribution if the data x_j are pure Gaussian noise.

The L-S periodogram is equivalent to a harmonic least-squares analysis [83]. Let's define the model $x_f(t) = a\cos\omega t + b\sin\omega t$ and minimize $E(\omega) = \sum_j [x(t_j) - x_f(t_j)]^2$ to determine the coefficients a and b and then $E_{min}(\omega)$, the power calculated in Equation 3.3 (assuming $\sigma^2 = 1$) is exactly equivalent to $\Delta E(\omega) = \sum_j [x(t_j)]^2 - E_{min}(\omega)$. That is, finding the maximum power in the periodogram is equivalent to finding the minimum $E_{min}(\omega)$ over a set of frequencies ω.

The powers are evaluated at a set of frequencies chosen to be the same as that

for the FFT, i.e., $\omega_n = 2\pi n/T \quad n = 0, 1, ..., N/2$. In the case of the FFT, the power contains half of the original information, as the phase information is lost in the calculation of the power. Moreover, the selection of the frequencies ω_n ensures a set of mutually independent set of $P(\omega_n)$. In the case of the L-S periodogram, the independence of the $P(\omega_n)$ is not necessarily true. However, the correlation coefficient between $P(\omega_n)$ and $P(\omega_n')$ is equal to the window function evaluated at $\omega - \omega'$, as long as the window function has a set of nulls (or small values) at the set of frequencies evaluated. In this case, the $P(\omega_n)$ are approximately uncorrelated (independent in the case of the Gaussian noise). It is shown [119] that for a wide variety of sampling schemes, the window function for the L-S periodogram is generally null or small at these evenly spaced frequencies. In theory, it is possible to evaluate the periodogram at frequencies at the nulls or minima of the spectral window up to $\omega = \pi/dt_{min}$. Once the independence between powers at different ω_n is established, the probability for detecting a power $P > P_0$ from a set of N powers is

$$\text{Prob} = 1 - (1 - e^{-P_0})^N. \tag{3.5}$$

3.1.2 Power Density Spectrum Based on FFT

For evenly sampled data, e.g., for the PCA data, it is advantageous to use the FFT method to evaluate the periodogram (commonly called the power density spectrum (PDS) in this case) because of its speed. For a data set $x(t_j), j = 0, ..., N-1$ evenly sampled at $t_j = jT/N$, where T is the total duration of the data set, the Fourier transform pair is defined as :

$$a_k = \sum_{j=0}^{N-1} x_j e^{2\pi ijk/N} \qquad k = -\frac{N}{2}, ..., \frac{N}{2} - 1, \tag{3.6}$$

$$x_j = \frac{1}{N} \sum_{k=-\frac{N}{2}}^{\frac{N}{2}-1} a_k e^{-2\pi ijk/N} \qquad k = 0, ..., N-1, \tag{3.7}$$

Two useful conclusions follow immediately from this set of equations,

$$a_0 = \sum_j x_j = N_{ph}, \tag{3.8}$$

$$\sum_{j=0}^{N-1} |x_j|^2 = 1/N \sum_{k=-\frac{N}{2}}^{\frac{N}{2}-1} |a_k|^2, \tag{3.9}$$

where N_{ph} is the total number of photon detected, and the second one is known as the Parseval's theorem. The variance of the data is then

$$Var(x_j) = \sum_j (x_j - \overline{x})^2 = 1/N \sum_{k=-\frac{N}{2}, k\neq 0}^{\frac{N}{2}-1} |a_k|^2. \tag{3.10}$$

With Leahy normalization [73], the power is defined as:

$$P_k = \frac{2}{N_{ph}} |a_k|^2 \qquad j = 0, ..., \frac{N}{2}. \tag{3.11}$$

Therefore, the power density spectrum is defined the same way as the periodogram except for the normalization. The statistical properties discussed in subsection 3.1 therefore also apply here.

The power density spectrum is often used to calculate the fractional root-mean-square (rms) variation r in the data x_j where

$$r = \frac{\sqrt{\mathrm{Var}(x_j)}}{\bar{x}}, \tag{3.12}$$

Two important factors have to be taken into account in the calculations. One is the dead-time, which occurs when the previous pulse height is high or the arriving time of the next photon is too close. As a result, the electronics are not ready to register the next photon arrivals for a short period of time (typically tens to hundreds of microseconds for the PCA). However, the PCA count rates involved in our data

are low enough so that the dead-time corrections are insignificant. The other factor is the binning factor. Binning of the data causes suppression of the high frequency features in the power spectrum. The fractional rms variation in the signal corrected for binning only is:

$$r = \frac{\pi\overline{\nu}\delta t}{\sin \pi\overline{\nu}\delta t}\sqrt{\frac{\int P_{signal}(\nu)d\nu}{I}} \tag{3.13}$$

where the first term is for the binning with the binsize δt [133], $I = N_{ph}/T$ is the average intensity, and $\overline{\nu}$ the average frequency of the signal feature in the power spectrum. The signal power is defined as $P_{signal} = P_j - P_{j,noise}$, where the noise power $P_{j,noise}$ is determined by the significance level (see [133] for details).

3.1.3 Correlations

The correlation for a pair of quantities (x_i,y_i, $i = 1, ..., N$) is a test of how one set of data responds to variations in the other. Intuitively, one could calculate the slope a of a least square fit to $y_i = ax_i + b$, or a_1 in the fit $x_i = a_1 y_i + b_1$ to see if it is significantly non-zero. The linear correlation coefficient derived from this idea (i.e., the Pearson's r) is:

$$r = sign(a)\sqrt{aa_1} = \frac{\sum_i (x_i - \overline{x})(y_i - \overline{y})}{\sqrt{\sum_i (x_i - \overline{x})^2}\sqrt{\sum_i (y_i - \overline{y})^2}}. \tag{3.14}$$

The value of r lies between −1 and 1, a coefficient $r = \pm 1$ means a complete correlation; that is, the data points can be fit to a straight line in the first-degree approximation with x and y increasing (decreasing) together. Two completely uncorrelated data set would yield $r = 0$. Under certain restrictions on the probability distribution functions from which the data sets x_i and y_i were drawn, e.g., a binormal distribution, the probability distribution of r can be estimated [104], and the significance of the detection and strength of the correlation can be tested. However, the distributions of the data are often not well known.

The Spearman ranking method [104] is a non-parametric ranking method. It not only yields correlation strength but also its level of significance reliably, which does not depend the original distribution of the data. For each data set, the value of each data point is replaced by the value of its rank among all other data points. That is, for N data points, the smallest value would be replaced with value 1 and the largest with N. If some of the data points have identical values, they would be assigned the mean of the ranks they would have if they were to be slightly different. For instance, the assigned ranks would be $[1, 2.5, 2.5, 4]$ for the data set $[1, 2, 2, 3]$. The correlation coefficient r_s is defined as

$$r_s = \frac{\sum_i (R_i - \overline{R})(S_i - \overline{S})}{\sqrt{\sum_i (R_i - \overline{R})^2}\sqrt{\sum_i (S_i - \overline{S})^2}}, \tag{3.15}$$

where R_i and S_i are the assigned ranks for the data points in each of the two data sets. The significance of a non-zero value of r_s is tested by computing:

$$t = r_s \sqrt{\frac{N-2}{1-r_s^2}} \tag{3.16}$$

which is distributed approximately as Student's distribution with $N-2$ degrees of freedom.

The main advantage of the Spearman-ranking method is that the significance level of the correlation does not depend on the the original probability distribution of the data. Because of this, the significance level of the correlation can be reliably computed even if the number of the data points used is small. Despite some loss of information in the substitution of ranks for the original values, the method is reliable in the sense that when a correlation is demonstrated to be present non-parametrically, it is really there. On the other hand, there exist examples where correlations could be detected parametrically but could not be detected non-parametrically. However, such examples are believed to be very rare in practice [104].

3.2 Spectral Analyses

The X-ray photons were recorded in the $RXTE$/PCA as counts per second $C(I)$ for each energy channel I. To obtain the incident flux $f(E)$, the energy response $R(E, I)$ of the instrument to the X-rays must be taken into account. We have

$$C(I) = \int_0^\infty R(E, I) f(E) dE \tag{3.17}$$

This is actually an $A\vec{x} = \vec{b}$ problem and ideally $f(E)$ can be solved directly by inversion. However, this is not possible in practice as the inversion often turn out to be ill-posed in the sense that the solution is unstable to small changes in C(I). It is therefore common in astrophysical data analyses that the $f(E)$ is obtained instead by best-fit analyses of the proposed models to the data. The "best-fit" is determined by varying p model parameters to minimize the quantity

$$S = \sum (C(I) - C_p(I))^2 / \sigma^2(I) \tag{3.18}$$

where $\sigma(I)^2$ is the expected variance, and $C_p(I)$ is the model predicted count rate. Each term of this sum is of the form of a deviation squared divided by the expected variance. Under the hypothesis that the deviations are approximately Gaussian, the quantity S is χ^2 distributed with N degrees of freedom. The minimal value of S (S_{min}) is theoretically χ^2 distributed with $N - p$ degrees of freedom, under the same hypothesis. The significance level of the fit for an observed $S_{min} \leq \gamma$ is therefore

$$\alpha = \int_\gamma^\infty f(\chi^2) d\chi^2 \tag{3.19}$$

where $f(\chi^2)$ is the density distribution of the χ^2_{N-p}.

Under the same hypothesis, the quantity $\Delta S = S - S_{min}$ is distributed as a χ^2 distribution with p degrees of freedom [68]. The contour for significance level α is

exactly

$$S_L = S_{min} + \chi^2_p(\alpha) \tag{3.20}$$

where tabulated values of $\chi^2_p(\alpha)$ can be found in [68] and in many statistics books. The parameter estimation methods described above cannot be expected to function reliably when the hypothesis is no longer true. Therefore, It is required that S_{min} be reasonably ranked in the χ^2_{N-p} distribution, i.e., that S_{min} not greatly exceed $N - p$.

Chapter 4

Periodicities Detected with the *RXTE*/ASM

4.1 Introduction

The All-Sky Monitor (ASM) on board *RXTE* has monitored over 300 X-ray sources in its 4.5 years of operation. Among them, about 150 X-ray sources have been detected with weekly average intensity above 10 mCrab. We have conducted a global search through the ASM data of all the 300 sources for evidence of periodic behavior using the first 3.5 years' ASM data (1996 March–1999 August). Updated results will be presented in future publications. The search has been conducted in light curves in all three ASM energy bands and the sum bands as well as light curves in 1-d timebins. The periodicity search was conducted by means of the Lomb-Scargle (L-S) periodogram (see Chapter 3). The periods we have searched range from about 1 hour to 1 year with exceptions for known short periods, such as the 837 s period in X Per. The spectrum is oversampled so that the frequencies are more closely spaced than $1/T$, where T is the total duration of the data used. The goal is to ensure the detection of a peak for a signal that is of border-line statistical significance and to best locate the peak.

Due to the nature of the detector operation, several artifacts have to be taken into account to determine whether or not a discovered period is intrinsic to the X-ray source. The well known observational constraints that might cause the artifacts have been described in chapter 2. In the periodicity search, we have detected the following "artificial" periods or the beats between them in many ASM light curves: (1) the $\sim$ 100 minute satellite orbit, (2) the 1 d spin period of the Earth, and (3) the 54 d precession period of the satellite orbit.

Most X-ray sources show low frequency red noise in its periodogram. This appears as a continuous rise of the average power level towards lower frequencies (most significantly at $\nu < 0.02$ cycles per day). This hinders detections of peaks at low frequencies as the source noise is no longer Gaussian. Therefore the statistics used to evaluate the significance of the detections has to be reconsidered in this range.

4.2 Detection Strategy

Once a L-S periodogram is calculated, peaks are examined to find signals against statistical fluctuations. We assume that noise in the data is mostly Gaussian noise convolved with the red noise. The periodogram of Gaussian noise can therefore be recovered if we divide the spectrum by the power of the red noise. Evaluation of the underlying red-noise power is purely empirical; it is approximated as the local average through a method similar to that of the Israel & Stella (1996) [61]. In this method, the red noise power at a frequency bin j is the local average of the underlying power calculated within a fixed number of frequency bins (the bandwidth) Δj_t. To better evaluate the shape of the red noise at low frequencies, the number of frequency bins to the right (Δj_R) of bin j and to the left ($\Delta j_t - \Delta j_R$) are set equal on a logarithmic scale, i.e., $\log(j + \Delta j_R) - \log j = \log j - \log(j - (\Delta j_t - \Delta j_R))$. The average noise power is then calculated in the left and right frequency bands respectively (with bins $j - 2$ to $j + 2$ excluded) and an average of these two numbers serves as the local

red noise power $P_{red}(j)$. The powers are then rescaled as $P(j) = P(j)/P_{red}(j)$. We choose the bandwidth Δj_t in a manner such that it maximizes the probability that the distribution of the rescaled powers is exponential expected for a Gaussian noise. To do so, we increase the bandwidth Δj_t by factors of 2.5 from 30 frequency bins up to one tenth of the total number of frequency bins in the data and calculate, for each binsize, the significance level that the rescaled powers follows an exponential distribution using the Kolmogorov-Smirnov (K-S) test [104]. Once the optimal bandwidth is found, the search for significant signals is carried out in the rescaled powers. In practice, the significance level that the rescaled powers follow the exponential distribution mostly vary in the range of 10% to 90%. Occasionally, the probability is very low ($< 1\%$), normally caused by the presence of strong signals, real or artificial, their harmonics, and beats between signals. As the estimated local average power is still reasonable, we still assume an exponential distribution for the rescaled powers. We also have found that detections of the low-frequency (< 0.1 cycles per day) signals are relatively more sensitive to the choice of the bandwidths; therefore, we also conduct separate searches for low frequency signals using the same procedure except that the bandwidth is increased by a smaller factor of 1.3 and within a smaller frequency range (< 1 cycle per day) for efficiency. In addition, for sources with dramatic transient outbursts or state transitions, separate searches for different intensity levels are performed.

The preliminary threshold to select candidate signals was chosen to give a false-alarm probability of $< 10\%$ in the entire periodogram. This probability is based on the assumption that the distribution of the rescaled powers is exponential. A detection is considered significant if (1) the false alarm probability is $< 10^{-3}$ in the entire periodogram, or (2) it is also confirmed by other independent means, such as in other wavelengths or other detectors. The criterion in (1) is proven to be very reliable in practise (see next subsection). Criterion (2) is reasonable because a detection at a previously known period is a factor of $\sim 10^4$ (proportional to the number of data points used) less probable for a spurious detection than a blind search for a unknown

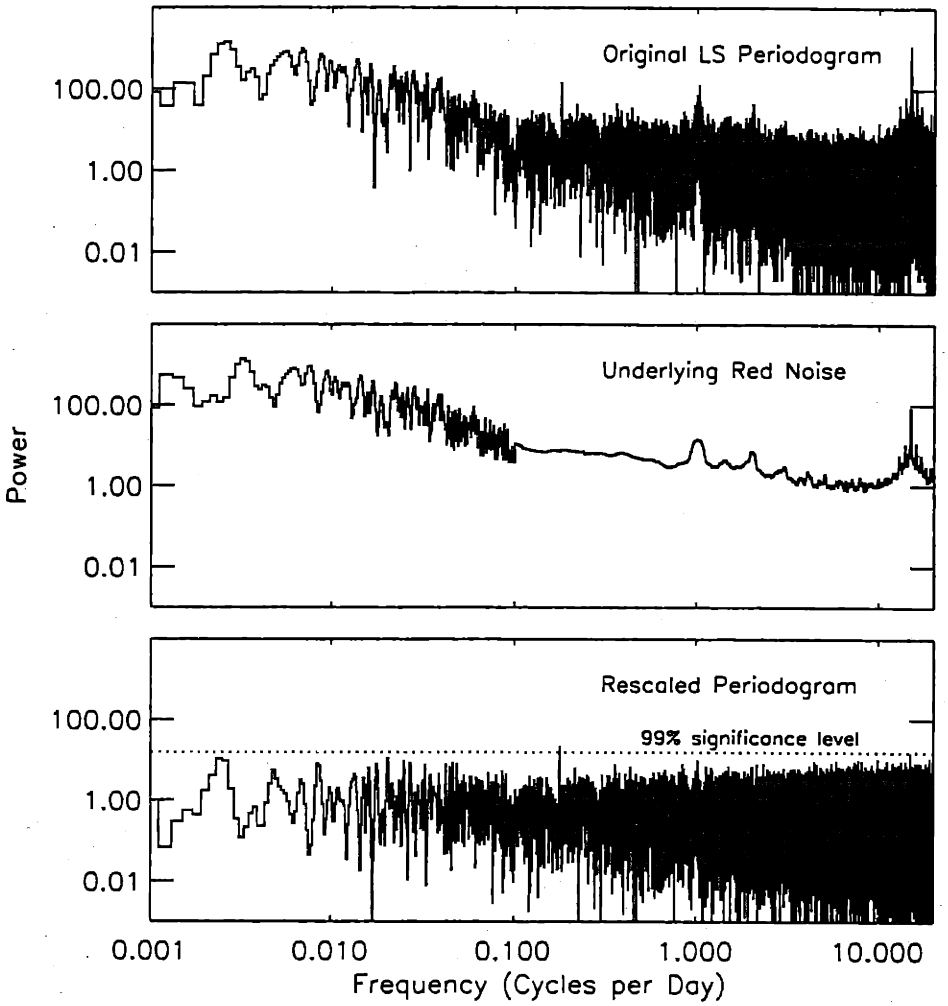

Figure 4-1 The Lomb-Scargle power density spectra of Cyg X-1. The calculated underlying noise, the rescaled periodogram and the threshold for a 99% significant detection are also shown (see text)

period. We reject periods that are longer than one-fourth of the duration of the ASM light curve and those caused by known artifacts described in the previous section. We also require that periods > 100 days that are previously unknown are selected only if they are detected in both searches of different binsizes. Detections are also examined by eye. An example of the periodogram, both original and rescaled, for the source Cyg X-1 in the low state, is shown in Figure 4-1. The original periodogram is shown in the upper panel; the known 5.6-d orbital period is apparent. In addition, the 1-day earth rotational period and the $\sim$ 100 min satellite orbit with its first harmonic are clearly present. The second panel shows the calculated local power level and the lower panel shows the rescaled periodogram. The 5.6-d period is clearly detected with the false alarm probability $P < 0.01$. The artificial frequencies (1 d^{-1}, 15 d^{-1}) which we introduced and their harmonics are well suppressed by our local background substitution technique due to the rising level of the local average towards the peaks. It is apparent that this method is generally conservative for detecting sharp coherent signals and is not favorable for detecting signals with broad features. This method therefore serves to minimize the false detections.

The detection sensitivity can be estimated with Equation 3.2. For data modulated with a sinusoidal signal of an amplitude of X_0, the peak-to-peak fractional modulation $(2X_0/\bar{I})$ required for a detection in a L-S periodogram with a rescaled power P_X $(P_R = 1)$ at the signal frequency can be written as:

$$2X_0/\bar{I} = 4\sqrt{\frac{P_X}{N}} \times \frac{\sigma_0}{\bar{I}}, \tag{4.1}$$

where $\bar{I}$ is the average intensity of the data, σ is the standard deviation of the Gaussian noise, and N is number of data points.

For the faint source AM her, we have $N = 33195$, a signal to noise ratio in the ASM intensity $\sigma_0/\bar{I}$=4.8, and a detection of the 3.09 hr orbital period in the rescaled periodogram with $P_X = 53$ (false alarm probability $\lesssim$ 1.8e-19). This indicates a 77%

peak-to-peak orbital modulation according to Equation 4.1. This is consistent with a calculated value of 72% from the folded light curve. For a luminous source such as Sco X-1, on the other hand, with the signal to noise ratio of the intensity $\bar{I}/\sigma_0 = 47.4$, a non-detection in a 90% confidence level (i.e. $P_X < 11.8$ for $N = 25887$) would indicate a $< 0.2\%$ peak-to-peak periodic modulation. Therefore, the periodogram could provide a simple estimation to the upper limit of the modulations for the non-detections from the ASM data.

4.3 Results and Discussions

We have selected a number of candidate periods depending on different detection criteria. At a 90% confidence level (within each periodogram), our periodicity search (in 1550 periodograms for 310 sources) has yielded 147 candidate periods in 114 sources. This confidence level is thus not sufficient to distinguish the real signals from spurious detections (10% chance). At a 99% confidence level, our search yields 46 candidate periods in 44 sources. Applying a threshold of 99.9% confidence level yields 35 periods in 33 sources. A total of 26 of these 35 periods are known from observations of other wavelengths or X-ray observations from other satellites. Two out of the remaining 9 periods are harmonics of periodic signals due to the known long-term quasi-periodic strong outbursts in Aql X-1 ($\sim$ 200 d apart) and in X 1608-522 ($\sim$ 900 d apart). The remaining seven are new detections with no other confirmations but all are detected with very low false alarm probability levels (10^{-5}–10^{-9}). Among them, X 1908+075 and XTE J1716-389 will be further investigated in this thesis (Chapters 7,8), while X 0114+650, XTE J1855-0237, X 0726-260, GRO J2058+42, and 3A 1942+274 have been published elsewhere (see references in Table 4-1). An additional search for previously known periods yields 4 significant detections. The false alarm probabilities for these detection at known periods are $< 10^{-5}$ even though the probabilities would be $\lesssim 10\%$ for a blind search among all frequencies. Long

periods (> 100 days) from 5 sources were thrown out because they have been detected with > 90% confidence level in one search but not in the other search. These are X 0614+091 (63.7 d), XTE J1550-564 (40 d), x1916-053 (83.6 d), GS 1843+009 (112 d), and Cyg X-1 (120 d). The periodograms show multiple peaks of similar strength around these periods. In summary, we have a total of 37 significant detections from our search.

A summary of the periodicities detected significantly (see above) in the ASM data is listed in Tables 4-1. The periodicities are classified according to the nature of their binary systems and possible causes. Column 1 contains the source names. New periods discovered with the ASM are indicated with double bullets. Periods detected for the first time in X-rays with the ASM but known previously at other wavelengths are indicated in single bullets. Column 2 and 3 list the detected periods and epochs, which are the best-determined values from refereed journals (listed in Column 6 and references therein). They include new periods determined from the ASM data but published in refereed journals by other authors. Note that optical or radio observations generally yield periods with higher precision than X-ray observations. We provide in the table three best-determined periods for the sources X 1908+075, XTE J1716-389, and 4U 1624-490 respectively. The first two periods are studied in Chapters 7 and 8 (see also [146]). For the so-called "big-dipper" 4U 1624-490, the orbital period was previously determined to be 21 ± 2 hr (see Table 4-1). This period has not been revised since then. We therefore provide a new estimate using the 4.5 years of ASM data with a method described in Chapters 7 or Chapter 8. Column 4 lists the average X-ray intensity in mCrab through the empirical formula 75 ASM ct/s = 1 Crab. Column 5 contains comments, which include the nature of the systems or mechanisms that have been proposed for the modulation. The question marks are added if the mechanisms proposed were highly speculative. Note that this table only lists results of our systematic search in the 3.5 years' ASM data (1996 March–1999 August). An updated version of a systematic study of periodicities from the ASM

data will be published elsewhere.

It is apparent that the ASM observations have provided a very useful database to study periodic effects in X-ray binaries and to discover new periods in many systems. At least 37 periods have been detected with high confidence in our method (with an additional one determined using other method, see [97]). Seven of these are new periods and four others were not previously known in X-rays (although known from studies at other wavelengths). The detected periods range from minutes, i.e., the 835 seconds rotational period of the neutron star in X Per, to hundreds of days, i.e., the 176-d superorbital period of NGC 6624. Remarkably, periods have been detected from sources as faint as LSI+61303 (daily average of 3 mCrab or 0.2 ASM ct/s), AM Her (4 mCrab) and X 1908+075 (8 mCrab) despite the fact that these sources are only marginally detected by the ASM. The narrowest eclipse detected is from EXO 0748-676 ($\bar{I}$=8 mCrab), the width of the eclipse is about 3.5% (FWHM) of the orbit, the detection is made with 94% confidence level.

Out of the $\sim$ 300 X-ray sources monitored with the ASM, over 100 of them are believed to be LMXBs and only < 60 are believed to be HMXBs. Yet it is apparent from the ASM results, there are far fewer orbital periodicities detected in the LMXBs than those in HMXBs. This, in part, perhaps can be accounted for in general by the lack of strong winds, periastron outbursts, and eclipses in the LMXBs. Partial eclipses of an accretion disk coronae (ADC) may be the cause of some of the modulations. These are consistent with previous considerations that LMXBs probably contain a thick accretion disk that blocks the line of the sight directly to the X-rays when the viewing angle is near the plane and that the partial eclipses are those of the scattered X-rays from the disk corona.

Superorbital periods reported in [79] have been especially examined in the ASM data. The confirmed significant detections are also listed in Table 4-1. There has been previously reported a 77 d period in Cyg X-2 [120], however, no peak has been found at this period. Instead, multiple peaks are apparent in the L-S periodogram

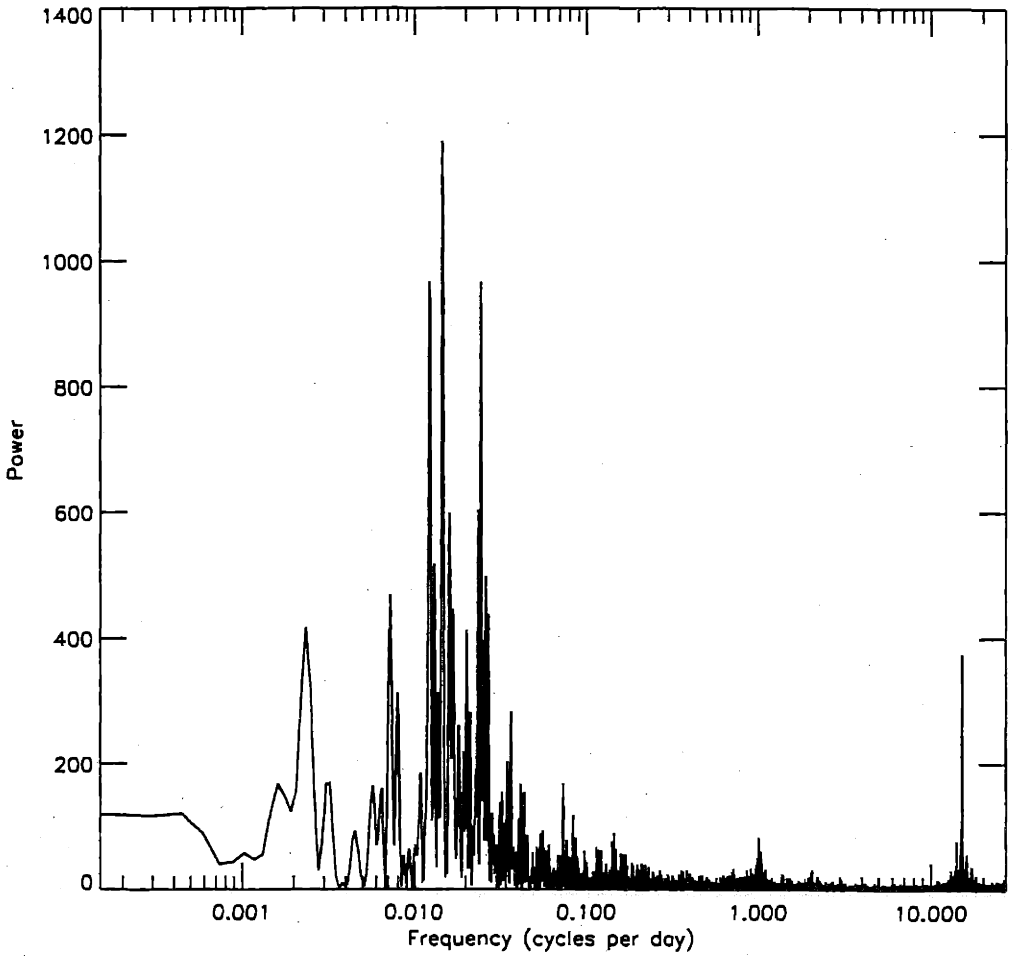

Figure 4-2 The Lomb-Scargle power density spectra of Cyg X-2. There are multiple peaks at frequencies < 0.03 cycles per day. The peaks at 1 cycles d^{-1} and 15 cycles d^{-1} are artifacts (see text).

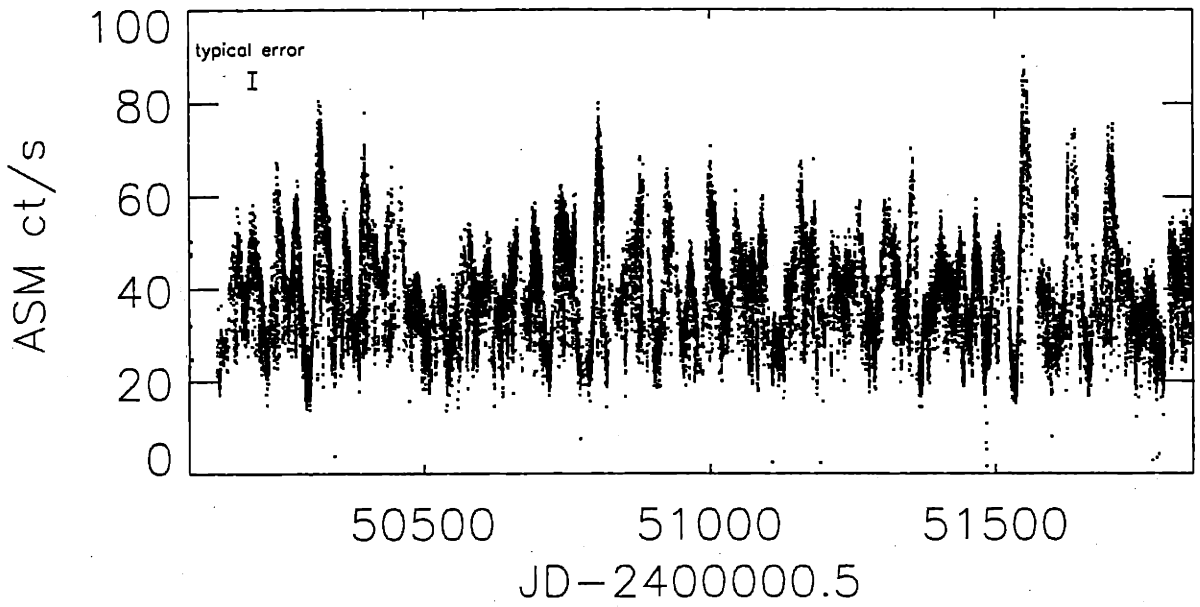

Figure 4-3 The ASM Light Curve of Cyg X-2. Quasi-periodic intensity variations on time scales between 60–90 days are clear.

(Figure 4-2). The three largest peaks are at (1) 81.96 d, (2) 40.98 d (the first harmonic of (1); the second harmonic is at 27.43 d), and (3) 68.71 d (perhaps the first harmonic of a 138.83 d peak). This erratic periodic behavior is also apparent in the light curve of Cyg X-2 (Figure 4-3). Besides, there is evidently no detection of a 42 d period in X 1907+097. We have not detected the reported 200 d period in X 1916-053 or in LMC X-3. Multiple peaks were found in the periodogram of X 1916-053 for periods > 40 d, and of LMC X-3 for periods > 100 d, evident of long-term intensity variability (e.g., Figure 4-4). Also, we have not observed the reported 294-d period in Cyg X-1 (Figure 4-1).

The ASM data is accessible to the public; therefore the data have been constantly searched for periodicities by various researchers around the world. Discoveries of new periods have often been claimed at marginal significance levels through the IAU Circ

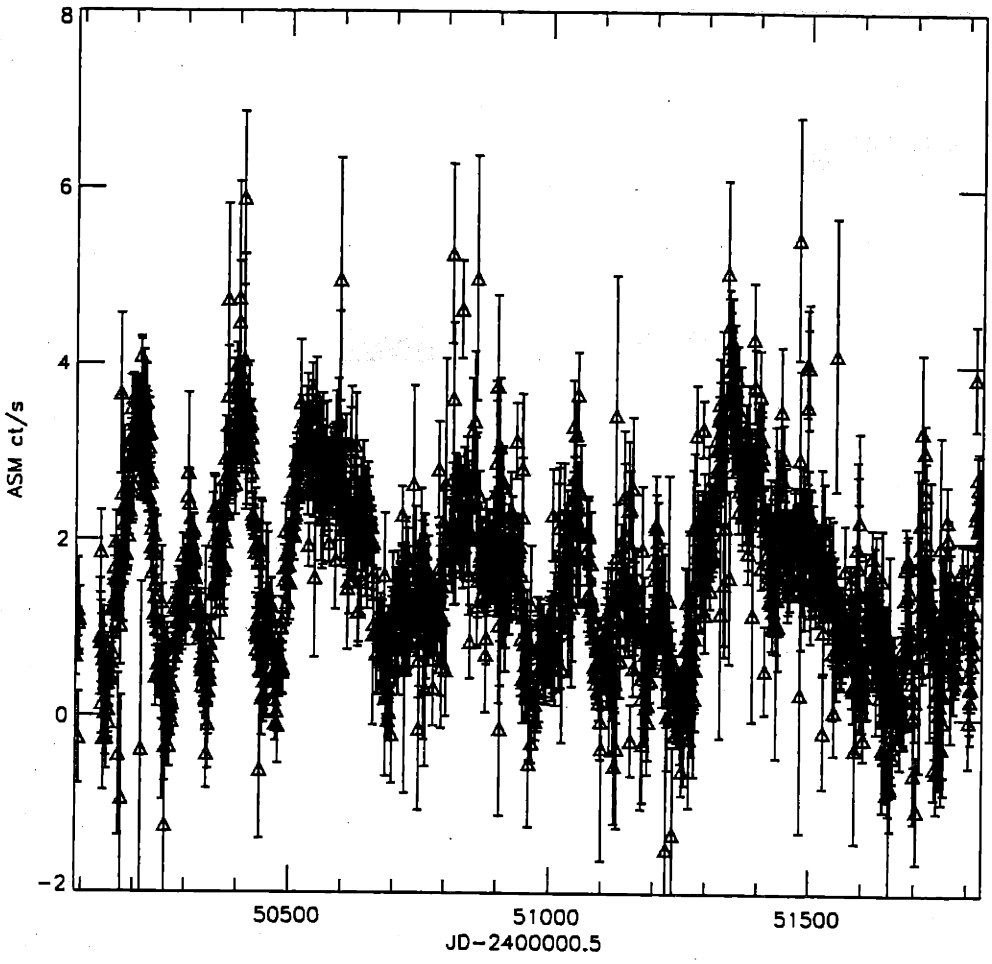

Figure 4-4 The ASM Light Curve of LMC X-3. Intensity fluctuations on time scales > 100 days are clear.

telegrams. With the accumulation of the ASM data over years, these results can be confirmed or dismissed. Our systematic search therefore plays an important role in clarifying the authenticity of the periodicities claimed previously. Besides this, the main goal of our work is to search for new periods and to better study the existing periodic phenomena in X-ray sources. The rest of this thesis therefore focuses on the new periods we have discovered in the X-ray sources X 1908+075 and XTE J1716-389 (Chapters 7,8) as well as on studies of the orbital modulations and state transitions in the BHC Cyg X-1 (Chapters 5 and 6).

Table 4-1: Periodicities Detected with the *RXTE*/ASM

	Source name	Period	Epoch [1] (MJD)	I_X (mCrab)	Comments	References
NS spin periods						
	X Per	837.6712(3) s	51215.5(5)	10	HMXB/Be	[33]
••	X 0114+650	2.73(1) h	50363.859	5	HMXB/SG?	[49]
Orbital periods: CVs						
	AM Her	0.128927041(5) d	43014.26614(4)	4	Polar	[51]
Orbital periods (in Units of days): LMXBs						
	EXO 0748-676	0.1593377316(25)	46111.0745687(42)	8	Eclipse	[100, 99]
	Her X-1	1.700167412(40)	48799.61235(1)	12	Eclipse	[31]
	X 1822-371	0.232110(3)	44105.168(5)	23	ADC	[89, 147]
	X 2127+119	0.713014(1)	47790.463(18)	14	ADC	[59]
	4U 1624-490	0.8699(3)	50001.124 (9)	49	Dip, ADC	[142], ch.4
	Cir X-1	16.54694(353)	50082.04 [2]	1258	Flares & dips	[122]
Orbital periods (in Units of days) : HMXB supergiant systems						
	LMC X-4	1.40839(1)	47741.9904(2)	6	Eclipse	[75]
	Cen X-3	2.08706533(49)	48561.656702	74	Eclipse	[38]
	4U 1538-522	3.72844(2)	47221.474(2)	14	Eclipse	[22]
	SMC X-1	3.89229118(48)	47740.35906(3)	20	Eclipse	[74]
	Vela X-1	8.964416(49)	48563.5364(33)	56	Eclipse	[32, 38]
	OAO 1657-415	10.44809(30)	48515.99(5)	14	Eclipse	[15, 38]
	Cyg X-3	0.19968196(42)	40949.4013(16)	164	Wind ?	[136]
	X 1700-377	3.41180(3)	42476.1803(37)	58	Wind	[11]
••	X 1908+075	4.400(1)	50439.919(68)	8	Wind?	[144], ch. 7
	Cyg X-1[3]	5.599829(16)	41163.029(9)	370	Wind	[12]
••	XTE J1855-0237	6.067(4)	50289.10(15)[4]	6	Wind ?	[19]
•	GRO J1655-40 [5]	2.62157(15)	49838.5763(55)[6]	497	Dip	[97]
	GX 301-2	41.508(7)	43906.06(16) [7]	26	Outburst/dip	[117]
	4U 1907+097	8.3765(16)	45578.64(3)	13		[85]
•	X 0114+650	11.588(3)	44136.698	5		[23]
Orbital periods (in Units of days) : HMXB Be-star systems						
	4U 0115+634 [8]	24.309(10)	48335.206(4)	9	Outburst	[110, 18]
•	LSI+61303	26.4917(25)	43366.275[9]	2		[98, 129]
••	X 0726-260	34.46(12)	50365.5(8)	2	Outburst	[20]
	EXO 2030+375	46.016(3)	48936.3(3)	5	Outburst	[123]
••	GRO J2058+42	110(3)[10]	50301.5	3	Outburst	[149]
•	RX J0812.4-3114	81	51261(2)	3	Outburst	[21]
••	3A 1942+274	87(6)	51080.5	10	Outburst	[13]

Table 4-1: Periodicities Detected with the *RXTE*/ASM (Continued)

	Source name	Period	Epoch (MJD)	I_X (mCrab)	Comments	References
Super-orbital Periods (in Units of days)						
	LMC X-4	30.50(5)	43393.16	6	HMXB/P	[69, 60]
	Her X-1	34.88(12)	41639.6(1.7)	12	LMXB/P	[42]
	SMC X-1	59.1 (50–60)		20	HMXB/P	[150]
	Cyg X-2	63 (60-90)		503	LMXB	[120]
••	XTE J1716-389	97.51(12)	50174.24(72)	23	LMXB(?)	ch.8
	SS 433	164(3)		8	HMXB/jet	[86]
	X 1820-303	175		253	LMXB	[120, 105]

•• indicates a new period discovered with the ASM.
• indicates a period discovered in X-rays for the first time with the ASM, but known from other wavelengths previously.

[1]Unless specified, for non-HMXB/Be systems, the epoch is at the minimal X-ray intensity or superior conjunction of X-ray source. For HMXB/Be star systems, it refers to the periastron of the orbit or time at maximum X-ray intensity. [2]Radio ephemeris at periastron passage. [3]Detected in the low state only. [4]At maximum light in X-ray orbital light curve. [5]Not detected by our method. Detected from the light curves during the outburst [6]Spectroscopic, at maximum radial velocity. [7]At periastron passage. [8]Detected with outburst data excluded (data at < 51200 MJD) only. [9]Radio observations, arbitrary chosen. [10]The ASM detected $\frac{1}{2}$ the period.

Table 4-2: Possible Periodicities Detected with the *RXTE*/ASM

Source name	Period
Algol	1.922 d
SAO 085590	1.657 hr
Cen X-3	7.557 d
E 17407-2942	6.171 d
GX 349+2	2.159 d
GX 354-0	40.64 d
HR 1099	2.485 hr
KS 1947+300	1.68 hr
N 5548	1.344 hr
NGC 2992	45.7 d
Noph 77	2.03 d

Note: these periods are listed for references only. No further investigations have been conducted on these periods.

Chapter 5

Orbital Modulation of X-rays from Cyg X-1

5.1 Introduction

In this chapter, we present a detailed study of the orbital modulation in the 1.5–12 keV energy band using data from the All-Sky Monitor (ASM) on board the *Rossi X-ray Timing Explorer* (*RXTE*). Our analysis focuses on the X-ray orbital modulation with the goal of investigating the cause of the broad intensity dip, an understanding of which may ultimately help constrain the system parameters. Specifically, we present (1) the results of a periodicity search; (2) the folded and individual orbital light curves; (3) a comparison of the orbital modulations in the soft and hard states; and (4) the results from a simulation of the orbital modulation caused by a partially ionized stellar wind from the companion. An earlier report of the detection of the 5.6 day period in the *RXTE*/ASM data was made by Zhang et al. (1996) [155]. We begin with a brief overview of our current knowledge of Cyg X-1 in section 5.2. The remaining of the chapter is adapted from *The Astrophysical Journal*, **525**, 968 (1999) by Wen et. al.

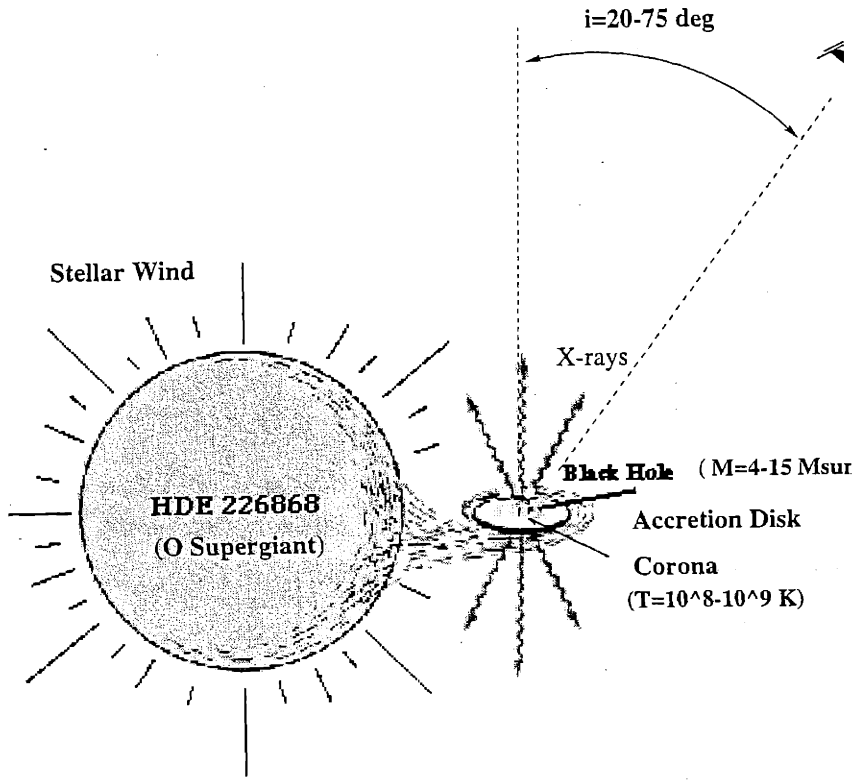

Figure 5-1 Schematic Illustration of the Binary System Cygnus X-1.

5.2 Overview of Cygnus X-1

Cyg X-1, discovered in a 1964 rocket flight [8], has been identified as a binary system of 5.6-day orbital period which contains an O9.7 Iab supergiant and a compact object that is believed to be a black hole [6, 143] (Figure 5-1). The distance to this system is estimated to be 2.5 kpc, based on extinction measurements. The X-ray luminosity is $L_x \sim$ a few $\times 10^{37}$ ergs s^{-1}.

The observed intense X-ray flux from this system is thought to be produced close to the black hole in an accretion disk which emits soft X-ray photons and in a hot corona ($T \sim 10^8$–10^9 K) that inverse-Compton scatters low energy photons to higher energies (e.g., [82, 125] and references therein). The accretion flow from the supergiant is probably intermediate between Roche-lobe overflow and stellar wind accretion (e.g., [48]).

5.2.1 System Parameters

The most direct evidence for a blackhole in Cyg X-1 is the mass of the compact object. As the companion is identified in optical as an O star, which typically has mass of 20–30 $M_\odot$, and the projected velocity of the companion is measured as $V \sin i = 72$km/s from optical spectroscopy, we have $M_X > 9\ M_\odot$ (see Equation 1.1).

The mass of this system remains one of the most interesting parameters for this system. Gies and Bolton (1986a) [47] determined the minimum masses of the visible star and the compact object to be 20 $M_\odot$ and 7 $M_\odot$ with probable values of 33 $M_\odot$ and 16 $M_\odot$ respectively. In their analysis, the inclination angle was determined primarily by fitting the ellipsoidal photometric light curve variation of a tidally distorted visible star. The masses were then determined for a given inclination angle by model-fitting of the observed rotational line broadening of the photospheric absorption lines under certain assumptions of the Roche lobe fill-out factor and the synchronism parameter of the optical star. It was found that the inclination angle ranged from 27° to 39° for Roche lobe fill-out factors of 1.0–0.9. However, larger inclinations could not be ruled out; the only reliable upper limit on the inclination angle was imposed by the absence of an X-ray eclipse.

Herrero et al. (1995) [52] reported that possible masses for the black hole lie between 4.8 $M_\odot$ and 14.7 $M_\odot$ with a probable mass of 10 $M_\odot$. In their calculation, the mass of the supergiant was inferred from its spectrum, and the inclination angle of the system was assumed to be in the range $27° < i < 67°$. One of the larger uncertainties in the determination of the masses comes again through the inclination angle i, which remains relatively poorly constrained. The various existing techniques to determine i, such as those using the variation of the polarization of the optical light, allow it to be in a wide range of 25–70° (e.g., [84]).

The 5.6-day orbital period of Cyg X-1 is well-established and may be detected via several effects. In the optical band, this period manifests itself as radial velocity variations of the absorption/emission lines [7] and as ellipsoidal light variation (e.g.,

[139]). Phase-dependent variations of the equivalent width of the UV lines of Si IV and C IV have been reported by Treves (1980) [131] and attributed to the orbital motion of the X-ray heated region of the stellar wind. Orbital modulations in the near-infrared J and K band [72] and in radio at 15 GHz [101] have also been reported. The causes of these modulations are still speculative.

X-ray orbital modulations in the hard-state data of several investigations show an intensity minimum around superior conjunction in the folded light curves. A 1300-day record of Ariel 5 ASM observations in the 3–6 keV band yielded an intensity minimum near superior conjunction even though the 5.6 day period was not detected at a convincing level of statistical significance in a power density spectrum [55]. The existence of a broad dip near superior conjunction was confirmed in 100 days of hard state data from the WATCH/Eureca wide field X-ray monitor [106]. In the 9–12, 12–17 and 17–33 keV bands, the dips had depths of $\sim$ 21%, 20%, and 10% respectively. The width (FWHM) is 26% of the period in the 9–12 keV band. It is unclear how this type of broad dip is related to the shorter irregular dips discussed in subsection 5.2.3. A 5% peak-to-peak orbital modulation was also found in 3 years of BATSE data in the 45–200 keV band [114].

5.2.2 X-ray Emitting Mechanism and Environment

Like many other hot luminous stars, there is believed to be a dense radiatively driven stellar wind from the companion O star of Cyg X-1. The O star emits most of its radiation in the ultraviolet, the momentum of which is transferred to the gas, starting in the lower layer of the star's atmosphere, via specific absorbing ions, mainly those of C, N, O, Ne, Si, P, S and Fe-group elements. The momentum gained by these ions are then shared with the surrounding gas particles through Coulomb coupling. If the outer layer of the wind is moving outwards, the gas sees photons red-shifted in the comoving frame. The Doppler effect therefore allows the outer atmosphere to absorb the photons which have initially higher frequencies than the lines and are not

attenuated by the layers in between the photosphere and the outer atmosphere. For a O star, radiation acceleration due to lines in the star's atmosphere is found to be very efficient for driving a stellar wind.

The accretion flow from the supergiant onto the blackhole is believed to be intermediate between Roche-lobe overflow and stellar wind accretion (e.g., [48]). Gies and Bolton (1986a) [47] found that the O star in Cyg X-1 nearly (about 90%) fills the Roche lobe. They also [48] have observed a He II λ 4648 emission line that exhibits orbital Doppler shift. The derived orbital velocity (near the photosphere of the optical star) and flow velocity indicate that the emission is from the L1 point. This is consistent with the hypothesis that the wind is focused along the line joining the center of the two star through the L1 point.

The inverse Comptonization model so far has best produced the observed hard state X-ray energy spectra in Cyg X-1. In this model, the soft photons, with temperature $T_0 < 1$ keV, are Compton upscattering by a hot thermal electron plasma with temperature $T_e \sim 100$ keV and a optical depth $\tau < 1$ [130]. The model reproduces the observed spectrum in X-rays with a power law component, with an index that depends on the T_e and τ only, and a high energy cut-off above T_e. This model also predicts that, during the state transition from the hard to the soft state, the increased supply of the soft photons cools the electrons and result in a steeper power law. However, the observed soft-state spectrum could extend up to 600 keV without cut-off, this contradicts the picture described above. The addition of a non-thermal electron distribution to the thermal plasma could produce the hard tail [45].

5.2.3 State Transition and Other Intensity Variability

Two physically distinct states of Cyg X-1 have been observed: the hard state and the soft state. Most of the time, Cyg X-1 stays in the hard state where its 2–10 keV luminosity is low and the energy spectrum is hard. Every few years, Cyg X-1 undergoes a transition to the soft state and stays there for weeks to months before returning

to the hard state. During the transition to the soft state, the 2–10 keV luminosity increases, often by a factor of more than 4, and the energy spectrum becomes softer (see reviews by [94, 82] and references therein; also the *RXTE*/ASM light curves in Figure 5-2). Interestingly, the total 1.3–200 keV luminosity remained unchanged to within $\sim$ 15% during the 1996 hard-to-soft and soft-to-hard state transitions [154]. The transition between states lasts from less than a day to more than a week.

A number of models have been proposed to explain the spectral evolution of Cyg X-1 during the state transitions. For instance, Ichimaru (1977) [58] suggested that the physical condition of the accreted gas near the disk outer-boundary could drive the disk into either an optically thick state or an optically thin state, which correspond to the soft and hard state respectively. Zhang, Cui, & Chen (1997) [153] argued, based on the effects of black hole rotation, that the state transition of Cyg X-1 may be caused by a temporary reversal of the disk from being retrograde (hard state) to prograde (soft state), which can occur in wind accretion systems (e.g., [90, 115]).

In the magnetic flare model [34], the soft (hard) state corresponds to a lower (higher) scale height of magnetic flares above the accretion disk. The flares are energized by the reconnection of magnetic flux tubes rising from the accretion disk due to magnetic buoyancy instability. In the soft state, intense flares close to the disk greatly enhance the soft photon field which results in a soft X-ray spectrum. In the hard state, the flare is triggered high above the disk, the system is "photon starved" and thus results in a hard, Comptonized spectrum. In the framework of advection-dominated accretion flows (ADAFs), Esin et al. (1998) [37] argue that the spectral states of Cyg X-1 are uniquely determined by the mass accretion rate $\dot{m}$. In the hard state, $\dot{m}$ is relatively low, the inner edge of the thin disk is far away from the black hole and thus the emission from the disk is weak compared to that from the large, optically thin ADAF region. In the soft state, the $\dot{m}$ is higher, which causes the ADAF region to shrink and the thin disk to extend closer to the black hole. Therefore, at low energies the emission from the disk dominates over that from

the smaller ADAF region. More data are needed to distinguish these models.

The ASM light curve of Cyg X-1 clearly indicates long term variability on time scales ranging from 90 s to hundreds of days (see light curves in Wen et al. 1999 [145]) besides the observed state transition and orbital modulations. In the hard state, Cyg X-1 frequently exhibits short, irregular, absorption-like X-ray intensity dips. These dips usually last seconds to hours and seem to occur preferentially near superior conjunction of the X-ray source. They are often thought to be due to absorption in inhomogeneities in the stellar wind from the companion (e.g., [103, 111, 67, 3, 36]). Intensity flares seem to occur randomly every few tens of days, and relatively large soft flares on time scales of hundreds of days. It was reported [12] that during these flares, there are correlative behavior between the X-rays and radio variation, and the variation varies from time to time. Within the soft state, intrinsic variation is also apparent. The rms variation of the light curve in the 1.5–12 keV band is about 35% in the hard state, and 22% in the soft state; both are much larger than the expected uncertainties in the data based on counting statistics and systematic uncertainties (7% and 3% respectively). The spectral hardness seems to vary with the intensity. For instance, in the hard state, both the sharp absorption dips and some of the large flares show visible anti-correlation between the intensity and the spectral hardness.

5.3 Data

The X-ray light curves and hardness ratios from the ASM observations of Cyg X-1 (1996 March – 1998 September) are shown in Figure 5-2. During 1996 May (MJD $\sim$ 50220, where MJD=JD-2400000.5), a transition into the soft state is evident [25]. After about 80 days in the soft state, Cyg X-1 returned to the hard state and remained there through 1998 September. The hard-state light curve shows long-term variations on time scale of 100–200 days and rapid flares that seem to occur every 20 to 40 days (see also [26]). For the analyses discussed below, the hard-state data are taken from

a 470-day interval (MJD 50367.432–50837.324) and the soft-state data from a 80-day interval (MJD 50227.324–50307.324).

In this paper, the hardness ratio HR1 is defined as the ratio of the ASM count rates in the 3–5 keV band to that of the 1.5–3 keV band, and the hardness ratio HR2 as the ratio of the count rates of the 5–12 keV band to that of the 3–5 keV band.

5.4 Analysis and Results

Periodicities in both the hard state and the soft state have been sought by means of Lomb-Scargle periodograms of both the light curves and the derived hardness ratios. The Lomb-Scargle periodogram [83, 119, 104] was used to estimate the power density spectrum instead of the classic periodogram based on the Fast Fourier Transform (FFT) since the ASM data points are unevenly spaced in time. In the Lomb-Scargle periodogram, a maximum in the power occurs at the frequency which gives the least squares fit of a sinusoidal wave to the data. We oversampled the spectrum so that the frequencies are more closely spaced than $1/T$, where T is the total duration of the data used. The goal is to ensure the detection of a peak for a signal that is of border-line statistical significance and to best locate the peak. The frequency range we have searched is up to (or beyond) $\sim N/(2T)$, where N is the number of data points.

5.4.1 Hard State

The Lomb-Scargle periodograms for the hard state are shown in Figure 5-3. There is a distinct peak in the periodogram at a frequency that is consistent with Cyg X-1's optically determined orbital period, i.e., 5.599829 ± 0.000016 days [12, 46, 71]. The peak is much more apparent in the periodograms of the hardness ratios than in those of the light curves. Some of the periodograms also have a significant peak at the frequency of $1/2.8$ d^{-1}, the first harmonic of the orbital period. There is a large

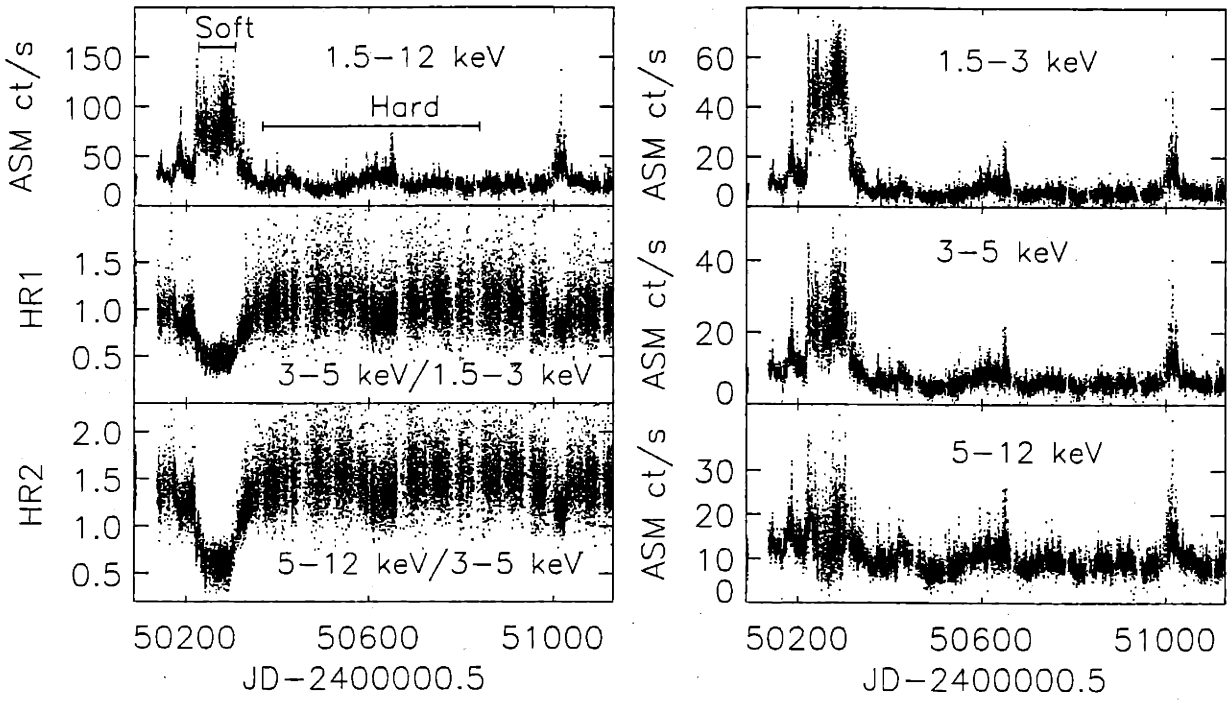

Figure 5-2 *RXTE*/ASM light curves and hardness ratios of Cyg X-1 for the period 1996 March to 1998 August. MJD 51000 corresponds to 1998 July 6. The marked intervals indicate the hard-state and soft-state data used for the analysis. An 80-day soft state is apparent.

peak at a very low frequency corresponding to a period of about 300 days, which is consistent with the reported 294 ± 4 day period by Priedhorsky, Terrell, & Holt (1983) [109] and by Kemp et al. (1983) [66]. However, the temporal span of the ASM data is too short to confirm this period; it could simply be "red noise". In fact, this peak is no longer distinct in the periodograms calculated using an extended set of data, i.e., 860 days of hard state data. No other periodicities stand out at frequencies less than 20 cycles per day except for the "peaks" at $\lesssim 0.1$ cycles per day which appear to be red noise (the spectrum for frequencies larger than 10 cycles per day is not shown).

The data were folded modulo the orbital period of 5.599829 days to study the phase-dependent variations (Figure 5-4). We used the orbital ephemeris reported recently by Brocksopp et al. (1999) [12]. The most distinctive feature in the folded light curves is the broad intensity dip. It is seen in all energy bands and is centered on the superior conjunction of the X-ray source (phase zero). The dip profiles are quite symmetric about superior conjunction. The fractional amplitude of the modulation in the light curves is larger in the lower energy band, which manifests itself as gradual spectral hardening during the dip. The fractional amplitudes of the dip relative to the average non-dip intensities (phase 0.3-0.7) are 23% for 1.5–3 keV, 14% for 3–5 keV, and 8% for 5–12 keV. The widths (FWHM) are all about 27% of the orbital period. The corresponding fractional changes of HR1 and HR2 are about 13% and 8% respectively with similar widths. Taking into account the variation of the non-dip intensity in the folded light curves, we estimated the uncertainty in the fractional orbital modulations to be less than 4%.

Complex structures are evident within the dip for at least 25% of the orbital cycles observed by the ASM. The profile of the structure also seems to vary from cycle to cycle. As the ASM data are unevenly sampled in time, we have found only a few orbital cycles that are relatively uniformly sampled. We show in Figure 5-5 one such cycle of the hard state observations with time bins of 0.1 day in the energy band

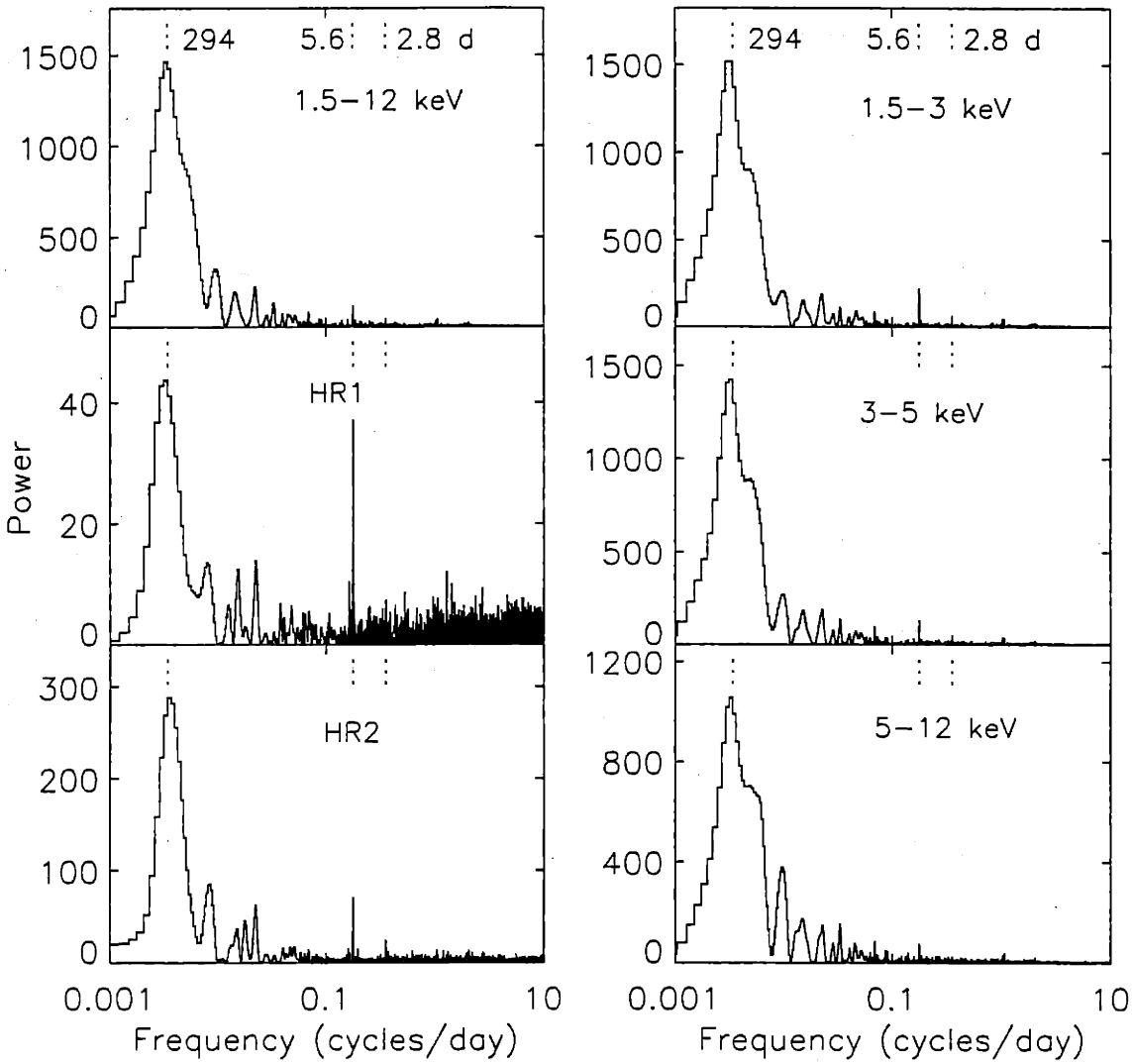

Figure 5-3 The Lomb-Scargle Periodograms of the light curves and hardness ratios for the hard state. The periods of 2.8 d, 5.6 d, and 294 d are marked by dotted lines.

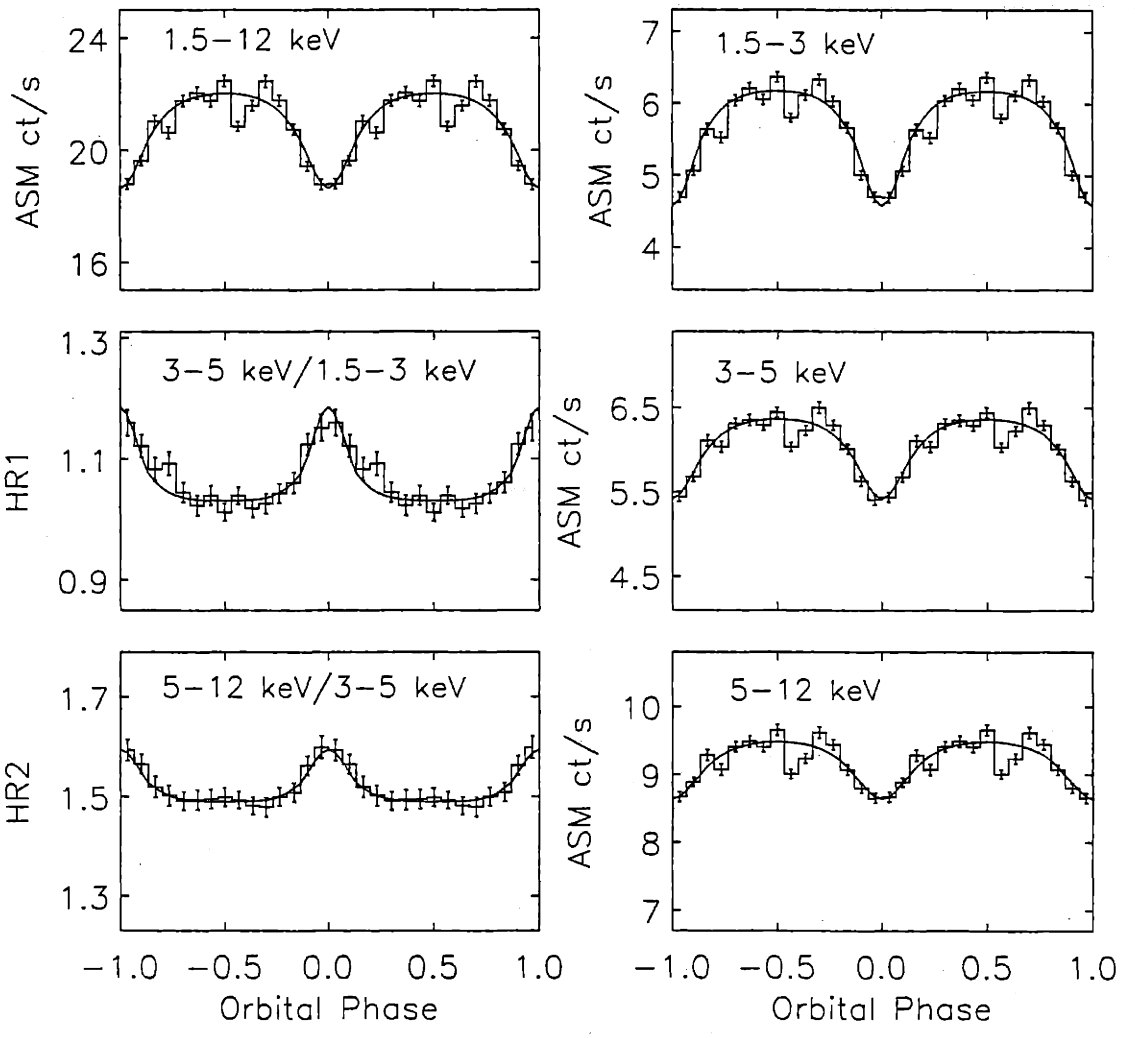

Figure 5-4 Folded light curves and hardness ratios for the hard state. The histograms represent the observations. Orbital phase zero is defined as the superior conjunction of the X-ray source. The error bars represent one standard deviation. The smooth curves show the predictions from a wind absorption model for $i = 30°$ (see text).

1.5–3 keV. There is a broad intensity dip at superior conjunction with substantial substructure. In particular, there are two narrow dips near superior conjunction: within a few hours, the intensities dropped by a factor of ~ 2, and the hardness ratios (HR1) increased by a factor of > 1.6. This indicates that the dips were much less pronounced at higher energies as might be expected from an absorption process. These smaller dip-like structures are similar to those reported from previous missions. It is possible that the broad dip may be, partially or wholly, due to the superposition of smaller dips. We do not explore this possibility further because the study of such small dips (at time scale of seconds to hours) requires more frequent sampling around superior conjunction than is provided by the ASM.

5.4.2 Soft State

In contrast with the hard state, Lomb-Scargle periodograms of the soft-state data show no large power at the orbital period compared with the neighboring powers (Figure 5-6, left panel). Neither were any other periodicities found in the frequency range of 0.1–10 cycles per day. At low frequencies, i.e. $\lesssim 0.1$ cycles per day, red noise is evident. For a direct comparison of the soft state data with the hard state data, we constructed periodograms for an 80-day segment of the hard-state data that has a comparable number of data points (Figure 5-6, right panel). The 5.6 day orbital period is clearly detected in the hard state periodogram but is not obvious in the soft state.

In comparing periodograms, we use the normalized variance, i.e., the observed total variance of the count rate divided by the average rate. For a sinusoidal modulation superposed on random noise, the expected height of a peak in the periodogram is then proportional to the product of the number of data points and square of the fractional modulation divided by the normalized variance (see equation 21 in Horne & Baliunas 1986) [56]. For the 1.5–3 keV band soft state data, the normalized variance is $\sim (0.53)^2$ that of the hard-state data. Thus, for comparable fractional orbital

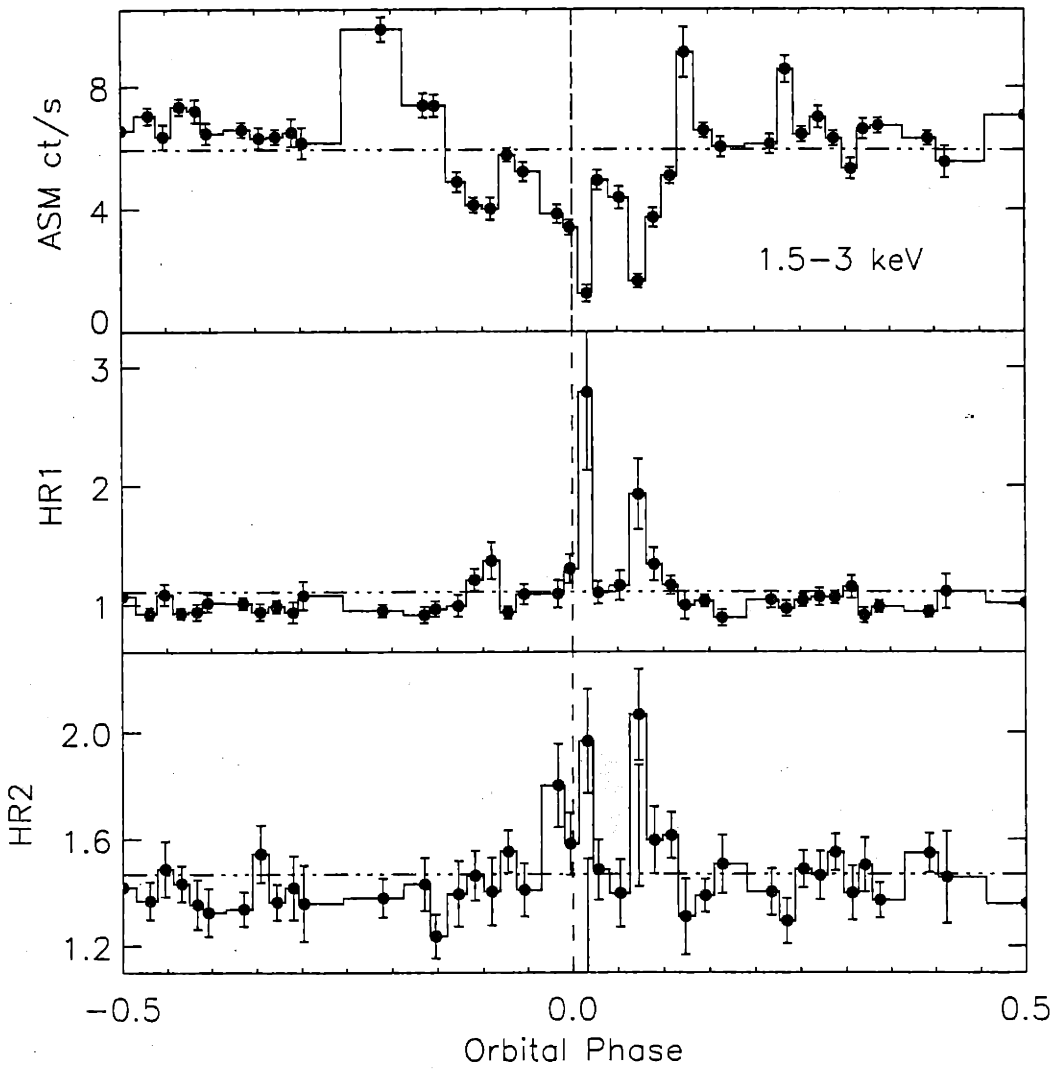

Figure 5-5 Light curve and hardness ratios for one orbital cycle of the hard state. The data are averaged in 0.1-day bins. Some phase bins contain no data points. The histograms and the overall average (horizontal lines) are to aid the eye. Note the complex structures around phase 0.

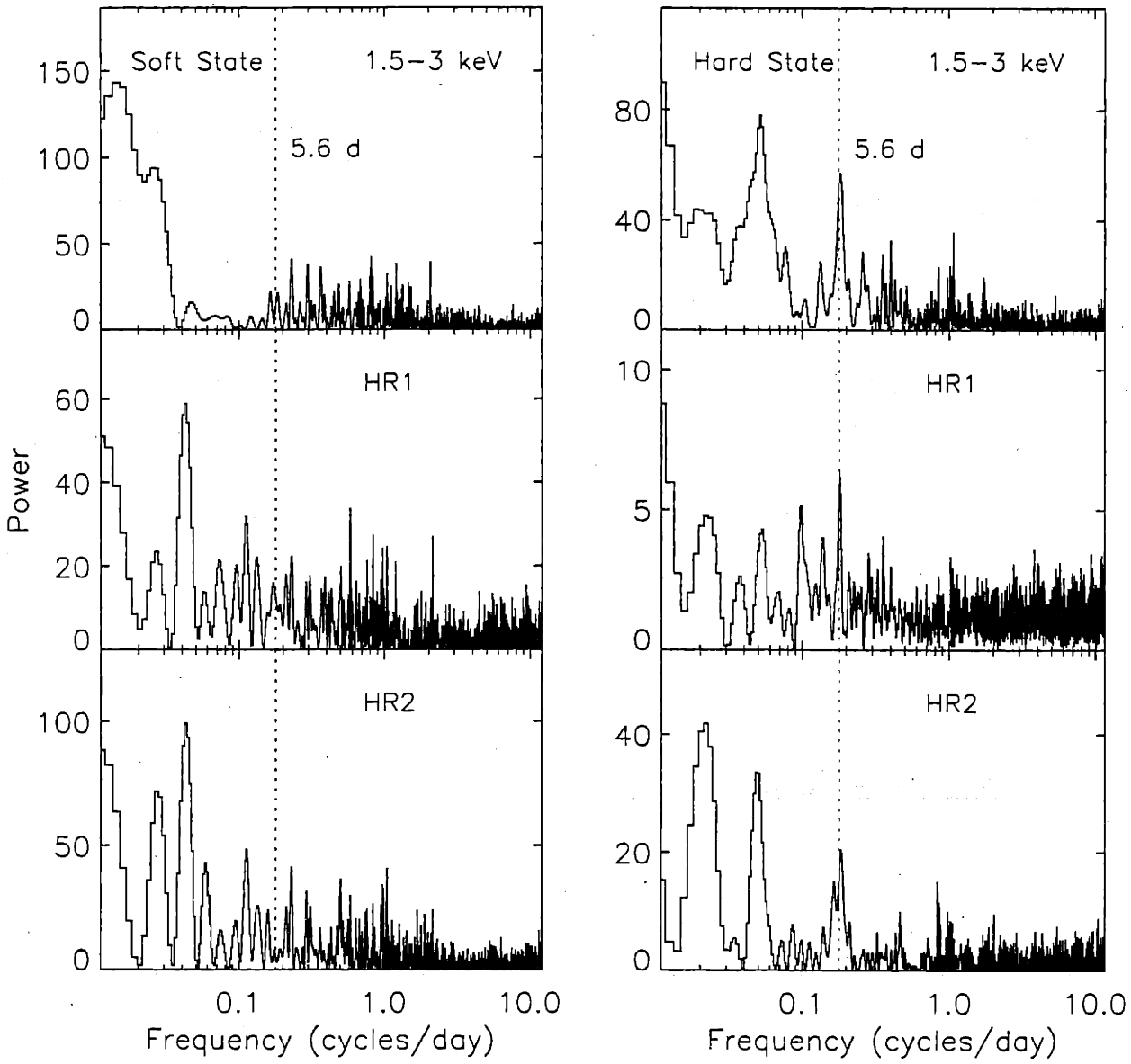

Figure 5-6 Lomb-Scargle periodograms for the soft (left) and hard state (right). The time interval for the hard state was selected to contain a number of data points comparable to that for the soft-state time interval. The 5.6-day orbital period is detected in the hard-state data but is not apparent in the soft-state data.

modulations (assumed to be nearly sinusoidal), we expect the signal power of the soft state to be $\sim (0.53)^{-2} \approx 3.6$ times that of the hard state, or $P \sim 204$ (Figure 5-6). The absence of a peak with $P > 25$ at the orbital frequency in the soft state data thus clearly excludes the presence of comparable fractional orbital modulations in the 1.5–3 keV light curves of the two states. The folded orbital light curves and hardness ratios for the soft state (Figure 5-7) also fail to reveal any significant broad dip or spectral hardening near superior conjunction.

A quantitative comparison of the fractional rms amplitude of the X-ray orbital modulation of the two states was estimated from the classic periodogram (power density spectrum estimated using FFT) of the same data used above. We have binned the data and filled data gaps with the average rate in order to apply the FFT. It is well known that the rms variation of the source signal in the data can be estimated using the FFT power spectrum assuming that the signal power can be properly separated out from the total power spectrum (cf., [80, 133]). It is therefore relevant to study the distribution of the noise power in the periodogram. In the analysis below, only the powers at frequencies ≥ 0.1 cycles per day were considered because the noise power spectrum is relatively flat in this region. The powers were first divided by the local mean which was obtained from a linear fit to the power as a function of frequency. The scaled noise powers of both the soft and hard state data were found to be consistent with a χ^2 distribution with 2 degrees of freedom. We then assumed that modulation at the orbital period would yield peaks with the same widths in the power density spectrum from both states. On this basis, we derived the fractional rms amplitude of the orbital modulation for the hard state and an upper limit for the soft state for each ASM energy band at more than 90% confidence (cf., [80, 133]). This procedure was repeated for different time-bin sizes (0.0625, 0.125, 0.25 and 0.5 days) to check for consistency of the results. We found that in the 1.5–3 keV band, the fractional rms amplitude of the orbital modulation for the soft state is at most 33% of that for the hard state. The 3–5 and 5–12 keV bands yield higher

percentages.

5.5 Models

The broad dip in the folded light curves cannot be attributed to a partial eclipse by the companion. The companion is a supergiant with a size more than 10^3 times larger than the X-ray emitting region, so an eclipse of duration nearly 27% of the orbital period would have to be total. Neither can the dip be caused by absorption by neutral material with solar elemental abundances since the observed 8% reduction in flux in the 5–12 keV band would then be accompanied by a flux decrease in the 1.5–3 keV band of more than 80% as opposed to the observed 23%.

We have modeled the broad dip assuming that it is produced by absorption and scattering of the X-rays by a smooth isotropic stellar wind from the companion star. The wind is partially ionized by the X-ray irradiation. The X-ray modulation is then caused by changes in the optical depth along the line of sight to the black hole as a function of orbital phase. For simplicity, we did not consider possible complex structures in the wind, e.g., the tidal streams which could account for the strong X-ray attenuation at late orbital phases (> 0.6) in some other wind accreting systems (e.g., [5]). In our calculation, we neglected the influence of the UV emission from the optical star upon the ionization state of the wind as we expect it to have little effect on the X-ray opacity in the ASM energy band.

The radiatively driven wind model of Castor, Abbott, & Klein (1975) [14] was adopted in our calculation. In this model, the velocity of the wind can be described by a simple power law for $R > R^*$:

$$v_{wind} = v_\infty [1 - \frac{R^*}{R}]^\alpha, \tag{5.1}$$

where v_∞ is the terminal velocity of the wind, R the distance from the center of the star, R^* the radius of the star, and α a fixed index. A spherically symmetric wind is

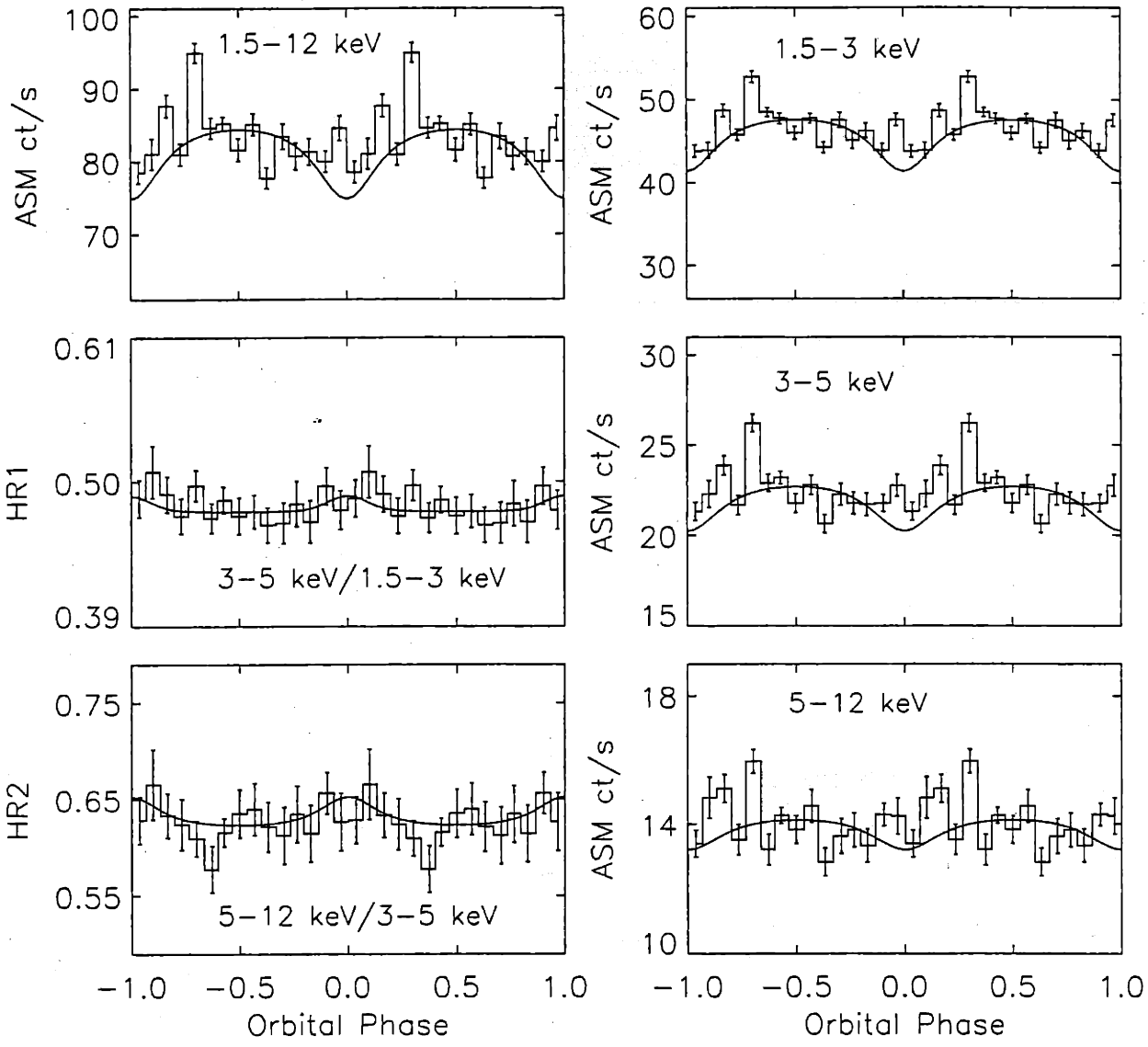

Figure 5-7 Folded light curves and hardness ratios, as in Fig. 3, but for the soft state. The simple wind absorption model produces lower fractional orbital modulation in the soft state compared with the hard state. However, a reduction of the wind density is required to explain the soft state data.

assumed for simplicity. We therefore approximate the wind density profile as:

$$n(R) = [\frac{R^*}{R}]^2 \frac{n_0}{\{1 - [R^*/R]\}^\alpha}, \tag{5.2}$$

where $n(R)$ is the number density of the wind, and n_0 is a wind density parameter, expressed in terms of the proton number density. The mass loss rate by the wind thus is $\dot{M} = m_H n_0 \times 4\pi R^{*2} v_\infty$, where m_H is the atomic hydrogen mass.

Simulated ASM light curves in the energy band E_1–E_2 were produced by integrating along the line of sight from the black hole for a given orbital phase ϕ:

$$I(\phi) = \int_{E_1}^{E_2} dE I_0(E) Q(E) \underbrace{\exp[-\int_{r_1}^{r_2} n(R(\phi, r, i)) \times \sigma(E, \zeta) dr]}_{wind\ absorption} \underbrace{\exp[-N_H \times \sigma_0(E)]}_{interstellar\ absorption} \tag{5.3}$$

where $I_0(E)$ is the intrinsic X-ray energy spectrum, $Q(E)$ is the ASM energy-dependent detection efficiency, r is the distance from the X-ray source, $\sigma(E, \zeta)$ is the photoelectric absorption cross-section per hydrogen atom for the partially ionized gas as a function of the energy and the ionization parameter $\zeta = L_x/[nr^2]$ where L_x is the effective source luminosity between 13.6 eV and 13.6 keV, $\sigma_0(E)$ is the absorption cross section per hydrogen atom for neutral gas, and N_H is the interstellar hydrogen column density.

The values for the parameters in equations (5.2) and (5.3) were determined or adopted as follows. For the wind model, we took $\alpha = 1.05$, $R^* = 1.387 \times 10^{12}$ cm, and $v_\infty = 1586$ km s^{-1} from Gies & Bolton (1986b) [48] who fitted equations (5.1) and (5.2) to the numerical results from Friend & Castor (1982) [40] for the radiative-driven wind profile of Cyg X-1. These values are for binary separation $a = 2R^*$, corresponding to a 98% Roche lobe fill-out factor of the companion, and for a wind profile that resembles a smooth wind from a single O9.7 I supergiant. The shape of $I_0(E)$ was chosen to be similar to that seen in the ASCA observations of Cyg X-1 in the hard state, i.e. with blackbody and broken power law components [36]. The

binary inclination angle was taken as $i = 30°$ from the most probable value derived by Gies & Bolton (1986a) [47]. The interstellar hydrogen column density was taken as $N_H = 5 \times 10^{21}$ cm^{-2}, slightly less than the values used in Ebisawa et al. (1996) [36], for a better fit to the ASM data . The values for $\sigma_0(E)$ are from Morrison & McCammon (1983) [93], and finally, for the wind, solar elemental abundances were assumed (as listed in [93])(Table 5-1).

The cross-section $\sigma(E, \zeta)$ depends highly on the ionization state of the wind. Under the assumption of a steady state, the ionization state of an optically thin gas illuminated by an X-ray source can be uniquely parameterized by the ionization parameter ζ for a given X-ray source spectrum [128]. For each ionization state of the optically thin gas, the local effective X-ray opacity can be uniquely determined from atomic physics calculations. The program XSTAR (v. 1.46, see [64] for theoretical basis) was used to obtain an opacity table which contains $\sigma(E, \zeta)$ for a wide range of ionization parameters and energies. For any particular ionization parameter value, $\sigma(E, \zeta)$ can be constructed by interpolation. In our model, the Thomson scattering cross section was added to the cross section derived with the use of XSTAR. The wind absorption factor in equation (5.3) was integrated over the range 10^{11} cm $< r < 10^{13}$ cm. For $r < 10^{11}$ cm the wind is highly ionized while for $r > 10^{13}$ cm the density of the wind becomes very small; thus the absorption of the X-rays by the wind is negligible in both cases.

Our procedure was to find the wind density parameter n_0 which produced light curves with fractional orbital modulations matching those obtained from the hard state ASM data. The spectral parameters from Ebisawa et al. (1996) [36] were also adjusted slightly to match the intensity levels in the three ASM energy bands. The best-fit values were obtained by minimizing the χ^2 values of each model light curve relative to the data. The range of acceptable fit, with $> 90\%$ confidence level, is then estimated based on the increase of χ^2 from the minimum (cf., [68]). Note the uncertainties in our results do not include the uncertain effects of the assumptions

and binary parameters adopted for the calculation. The expected variance of the data in calculating χ^2 was taken to be the variance of the data between phase 0.3–0.7 to account for the possible intrinsic uncertainty associated with the data.

The best-fit model light curves of the hard state for our choice of $i = 30°$ are plotted as the solid lines in Fig. 5-4 to compare with the observational data. Clearly this simple wind model can account for the observed X-ray orbital modulation in the hard state very well. The adjusted spectral parameters are listed in Table 1. For a distance of 2.5 kpc, the derived intrinsic 1.3–200 keV X-ray luminosity from this model is 6.6×10^{37} ergs s^{-1}, which is consistent with the previously reported value (e.g., [154]). The wind density parameter is estimated to be $n_0 = (6 \pm 1) \times 10^{10}$ cm^{-3}, indicating a total mass loss rate of $\sim 6 \times 10^{-6} M_\odot$ per year. This value of n_0 is a factor of ~ 3 larger than that determined by Gies & Bolton (1986b) [48]. The hydrogen (neutral+ionized) column density is about 1.0×10^{23} cm^{-2}. The ionization parameter ζ varies from 10^5 to 10^2 along the integration path.

We have studied the effect of the inclination angle i upon the quality of the fit of the model light curves to the data. The minimum of the χ^2 value was found at roughly $i = 30°$ for data of all three energy bands. The acceptable range of the inclination angle was found to be $10° \lesssim i \lesssim 40°$, determined primarily by the data in the 1.5–3 keV band. This constraint is mainly due to the fact that the width of the dip of a fixed fractional amplitude in our model decreases if we increase the inclination angle (Figure 5-8). The best-fit n_0 ranges from 3.7×10^{10} cm^{-3} for $i = 40°$ up to 1.6×10^{11} cm^{-3} for $i = 10°$. Note that n_0 decreases if we choose a larger inclination angle i. The results are relatively insensitive to the ASM efficiency $Q(E)$ and the intrinsic X-ray spectral shape.

In the BATSE band, the X-ray opacity is entirely due to electron scattering. We found that in all our acceptable fits, attenuation caused by electron scattering would modulate the apparent intensity by 4–6% peak-to-peak, which is in good agreement with the data [114].

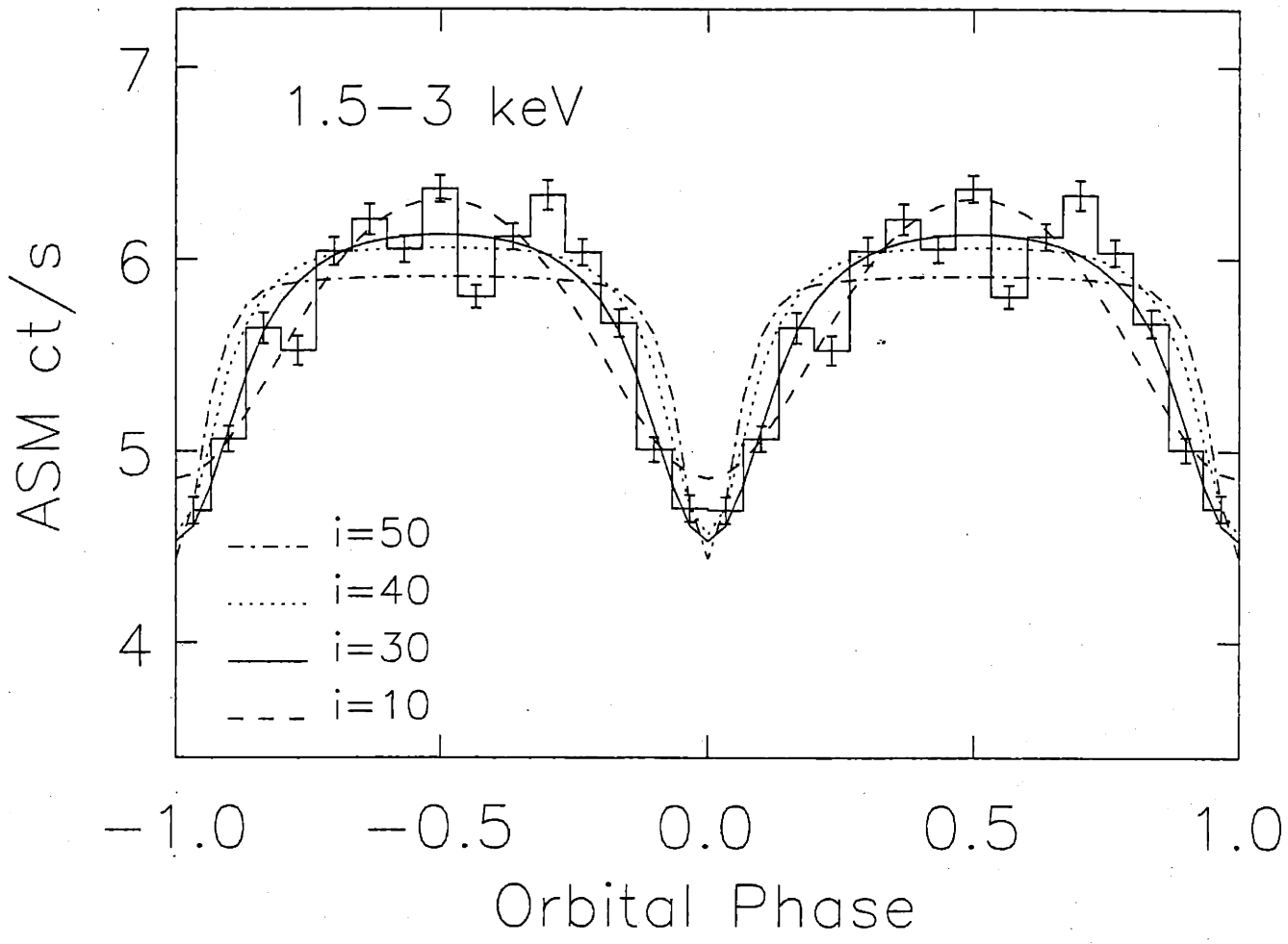

Figure 5-8 Predicted hard-state light curves from the wind absorption model for inclination angles between 10°–50°. The width of the dip decreases for larger inclination angles.

We repeated the same procedure for the soft state for $i = 30°$, assuming the same wind density profile (with $n_0 = 6.0 \times 10^{10}$ cm^{-3}) and using the energy spectrum adjusted slightly from that in Cui et al. (1997a) [27], again to match the count rates in the three energy bands. The results are plotted as solid lines in Figure 5-7. The model produces light curves of much smaller orbital modulations than in the hard state because the wind is more ionized due to a much larger flux of soft X-ray photons in the soft state. In the 1.5—3 keV band, the amplitude of the modulation ($\sim 14\%$) in the model light curve is not consistent with the upper limit ($\sim 9\%$) determined in section 3.2. Better fits to the data can be found with smaller values of n_0. For $n_0 < 4 \times 10^{10}$ cm^{-3}, the fractional modulation of the model light curve is $< 9\%$ in the 1.5–3 keV band for the soft state, which is consistent with the upper limit. A wind model with a non-variable wind density therefore cannot explain the data in the hard and soft states simultaneously in case of $i = 30°$. However, the non-detection of the orbital modulation in the soft state can be explained if the wind density is reduced by a factor of about 2 relative to the hard state.

Alternatively, the X-ray orbital modulation observed in the hard state may be caused by partial covering of a central X-ray emitting region by the accretion stream. The wind density in this model is assumed to be much less than that required in the model discussed above, therefore it does not contribute significant X-ray opacity. Hard X-rays are generally thought to be produced by upscattering of low energy photons by electrons in a hot corona (e.g., [82]). Observations seem to favor the geometry of a spherical corona centered on the black hole plus a standard thin disk (Figure 5-9) [35, 44, 102]. Recent studies indicate that the size of the corona in the hard state could be as large as 10^9 cm [57] and that it may *shrink* by more than a factor of 10 as the soft state is approached [29, 37]. For Cyg X-1 in both states, the X-ray emission observed above 1 keV is primarily from the corona. The accretion stream may have a scale height above the disk such that, viewed along the line of sight near superior conjunction of the X-ray source, it partially obscures the outer

region of the large corona in the hard state but does not do so in the soft state because the corona is much smaller (Figure 5-9). This constrains the distance of the absorber to be a few coronal radii away from the black hole. A covering factor around 23% is sufficient to explain the observed depth of the dip in the hard state with a cold absorber of line-of-sight hydrogen column density of (1–3) $\times 10^{23}$ cm^{-2}. If we take the degree of ionization into account, the hydrogen column density could be much higher, which may account for the observed modulation in the BATSE band.

5.6 Summary

Our analysis of *RXTE*/ASM observations of Cyg X-1 leads to the following conclusions: There is a broad smooth dip in the folded orbital light curves of Cyg X-1 in the hard state. The dip is symmetric about superior conjunction of the X-ray source. The depth of the dip relative to the non-dip intensity is around 23% in the 1.5–3 keV band, 14% in the 3–5 keV band, and 8% in the 5–12 keV band. The FWHM of the dip is 27% of the orbital period in the energy range 1.5–12 keV. Individual light curves show complex structures around superior conjunction in the form of dips of shorter duration. Finally, no evidence is found for orbital modulation during the 1996 soft state of Cyg X-1.

We examined the possibilities that the broad dip is produced by the absorption of the X-rays by a stellar wind from the companion star. This model reproduces the observed light curves of the hard state well for inclination angles $10^\circ \lesssim i \lesssim 40^\circ$ and can also explain the soft-state data if there was a reduction in the stellar wind density for the duration of the soft state. Alternatively, the observed X-ray modulation in the hard state may be mostly due to the partial obscuration of a central hard X-ray emitting region by the accretion stream. The lack of the observed orbital modulation in the soft state can be attributed to a significant shrinkage in the size of the X-ray emitting region such that it is no longer obscured by the accretion stream. This model

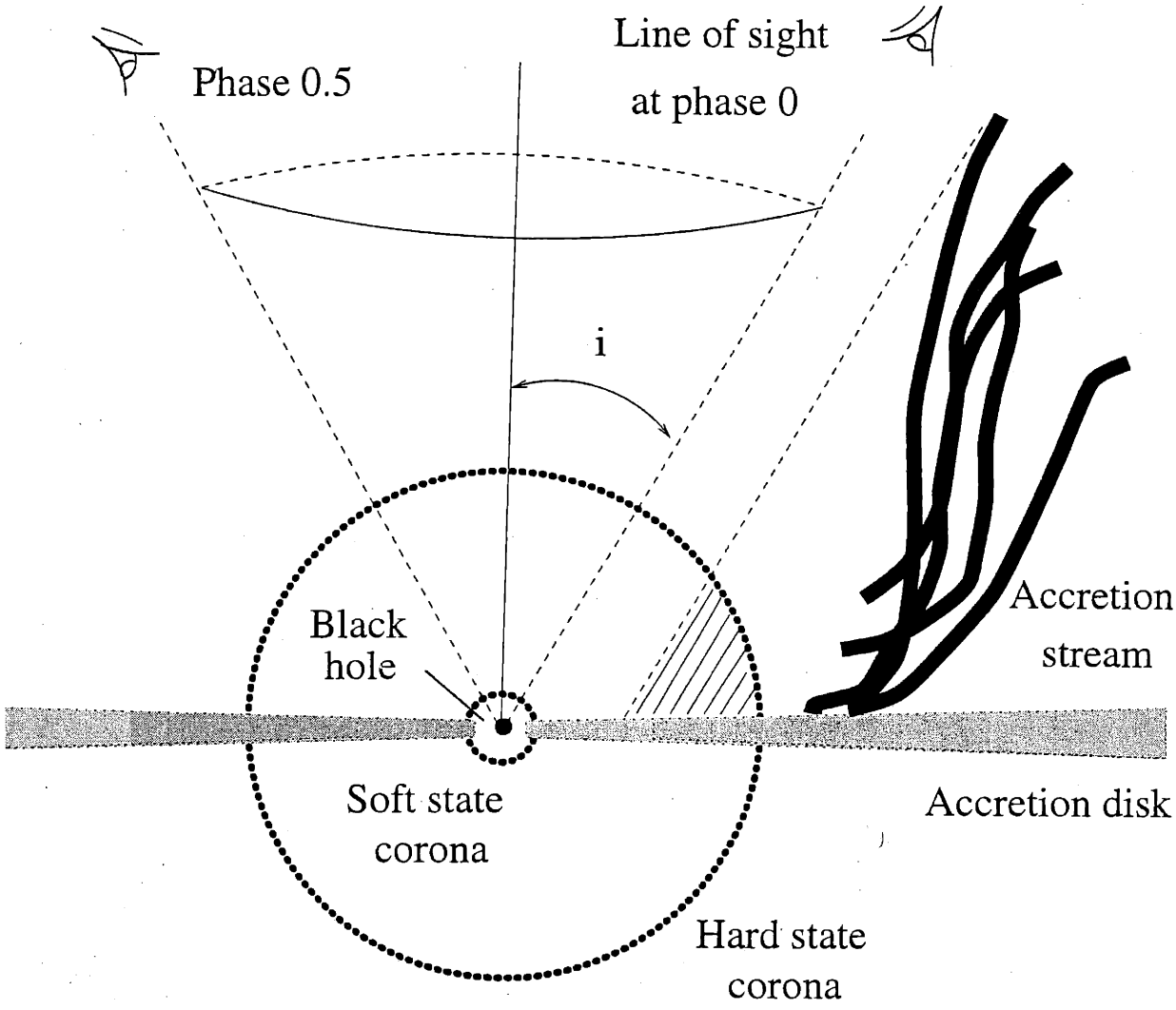

Figure 5-9 A schematic illustration of a possible geometry of the X-ray emitting region of Cyg X-1. Note that the size of the corona and the radius of the inner edge of the disk are larger in the hard state than in the soft state. The observed X-ray orbital modulation in the hard state is attributed to the partial covering of a large corona (the shaded region). The lack of modulation in the soft state may due to significant shrinkage in the size of the corona.

requires the accretion stream to have specific geometric properties, such as its scale height, width, and orientation. In both models, the required hydrogen column density can reproduce $\sim 5\%$ orbital modulation due to electron scattering as observed in the BATSE data [114].

Table 5-1: Spectral Parameters for the Hard State of CygX-1

Blackbody [1]		Broken Power Law [2]				Absorption [3]	Luminosity[4]
N_b	T_e (keV)	α_1	E_b (keV)	α_2	Np	N_H	L_X
7.5	0.16	1.84	4	1.515	2.63	5.0	3.4

[1] N_b: normalization in units of 10^{36} ergs s^{-1} at d=2.5 kpc, T_e: temperature
[2] E_b: break energy, α_1: photon index below E_b, α_2: photon index above E_b, Np: normalization in units of photon s^{-1} cm^{-2} keV^{-1} at 1 keV for $E \geq E_b$
[3] Interstellar hydrogen column density in units of 10^{21} cm^{-2}
[4] Calculated in the 13.6 eV–13.6 keV band in units of 10^{37} ergs s^{-1}

Chapter 6

The Intensity-Hardness Correlation of Cyg X-1

6.1 Introduction

In this Chapter, we report the results from a quantitative study of the correlation between the X-ray flux and the spectral properties of Cyg X-1, on time scales of 90 s to at least 10 days, in both the hard and soft states, as well as during the transition phases.

6.2 Data

The primary data set for this investigation comes from the All-Sky Monitor (ASM) on board the *Rossi X-ray Timing Explorer* (*RXTE*) [10]. We used the ASM observations of Cyg X-1 between 1996 March and 2000 April, which cover the entire 90-day 1996 soft state including its transition phases [27, 154] and four years of the hard state. The count rate in the 1.5–12 keV band and two hardness ratios HR1 and HR2 were computed. HR1 is the ratio of the count rate in the 3–5 keV band to that in the 1.5–3 keV band, and HR2 is the ratio in the 5–12 keV band to that in the 3–5 keV

band. The hardness ratios provide a rough measure of the X-ray spectral shape of the source.

The higher-quality data from the Proportional Counter Array (PCA) [62] aboard *RXTE* (with much poorer coverage) were used to verify the ASM results and to study the flux-spectral hardness evolution over a wider energy range. We used 63 PCA observations of Cyg X-1, with exposure times ranging from 700 s to 22 ks (but typically 3 ks), obtained from 1996 March 26 to 1998 April 28, nineteen of which cover the 1996 spectral state transition. To minimize the known effects of calibration uncertainties at higher energies, we limited the spectral analyses to the energy range 2.5–25 keV. Also, since the number of the proportional counter units (PCUs) that were turned on varied from observation to observation, we used data only from PCU 0 which was active during all of the selected observations, in order to facilitate comparison of different observations.

For each PCA observation, we constructed a light curve with 100 s time bins and an energy spectrum for each time bin using FTOOLS (v. 5.0). Each spectrum was then fit with an empirical model using XSPEC (v. 10.0). For the soft state, the model consists of a broken power-law component, an iron line around 6.4 keV and a fixed absorption ($n_H = 5.6 \times 10^{21}$ cm $^{-2}$, e.g., [36, 27]). For the hard state, we replaced the broken power law with a simple power law for the continuum, except for observations near the state transition or a pronounced soft flare in 1997 June. In the latter cases, the broken power law, sometimes an additional blackbody component, is required for obtaining an adequate fit. Variable absorbing column density is also necessary for some of the observations near superior conjunction of the X-ray source. All fits have reduced $\chi^2 < 1.5$. Note that our main objective here is simply to derive the energy flux of the source and its hardness ratios, as opposed to finding a physical model for the observed spectrum. The flux was calculated in the 2.5–25 keV band, as well as in the 3–5 keV, 5–12 keV, 12–17 keV, and 17–25 keV bands. The energy bands were chosen such that the first two coincide roughly with the two upper ASM

bands. Here, we defined the the hardness ratios as the ratios of energy fluxes between the first two (5–12 keV/3–5 keV) and the last two (17–25 keV/12–17 keV) energy bands.

6.3 Analysis and Results

We quantify the correlation between the source count rate and spectral hardness by means of a non-parametric method first proposed by Spearman (the Spearman ranking method [104]; see Ch.3). We computed, using Equation 3.1.3, the correlation coefficients r_s between the X-ray count rate and the spectral hardness for the ASM and the PCA data. For the ASM data with its original 90 s time bins, we calculated each correlation coefficient over a "correlation interval" for several values that ranged from 1 to 20 days. To explore the correlation relations for variability of different time scales, the calculations were repeated for time bins up to 10 days for the soft state, and up to 100 days for the hard state. In these cases, the correlation intervals were chosen to be 5 to 20 times the time bin size such that the average number of data points per interval is greater than three. For the PCA data (with 100 s time bins), we calculated one correlation coefficient for each observation, due to the limited number of data points. In all our calculations, data segments with less than 3 data points were excluded.

6.3.1 The ASM Results

The correlation coefficient r_{s1} between the X-ray count rate and the hardness ratio HR1 for a 90 s time bin and 5.6-day correlation intervals is shown in Fig. 6-1. The results for different correlation intervals are similar. For longer intervals, the correlations become statistically more significant as more data points are involved. The correlation interval of Fig. 6-1 is the 5.6-day orbital period of Cyg X-1. This allows us to compare the result to the possible contribution from the orbital modulation

of X-rays by the stellar winds [145]. Both r_{s1} and r_{s2} (count rate vs HR2) evolve similarly during the state transition.

The ASM count rate and spectral hardness in Fig. 6-1 are positively correlated in the soft state with an average r_{s1} about +0.7, corresponding to a false alarm possibility $< 10^{-30}$. Significant positive correlation was also found for time bins of 0.1 days, 1 day, 5 days and 10 days. In other words, the positive correlation in the soft state holds for variability on time scales from 90 s up to at least 10 days. In the hard state, the correlation in Fig. 6-1 turns weak and negative with an average r_{s1} about -0.2. Calculations with time bins of 5.6 days (to eliminate the orbital effect), 20 days, and 100 days also show negative correlation. In both states, the coefficient r_{s2} behaves similarly but with relatively weaker strength; about 0.5 for the soft state and -0.12 for the hard state for 90-s time bins and 5.6 d correlation intervals.

The evolution of the correlation during the state transition is a gradual one, as shown in Fig. 6-1. The entire episode of the 1996 state transition can be roughly divided into three distinct phases: (1) a 15–20 day transition phase from the hard state to the soft state, where r_{s1} goes from negative to positive, (2) a $\sim$ 50 day soft state with a steady positive r_s, and (3) a 15–25 day transition phase back to the hard state. The start time of phase (1) and end time of phase (3) indicated in Fig. 6-1 were chosen to be the times when the hardness ratios are roughly at the mid-point between the mean levels of the hard and soft states. This yields a $\sim$ 20 day time scale for phases (1) and (3), similar to what we would get if we were to choose the start (end) time to be when the correlation coefficient just started (ended) its sharp rise (drop). We obtain roughly the same results with smaller time bins (0.1 and 1 day), so the conclusions seem quite robust.

6.3.2 The PCA Results

The evolution of the two PCA hardness ratios with the energy flux is shown in Fig. 6-2. As expected, the energy flux and spectral hardness for $E < 12$ keV (left panel)

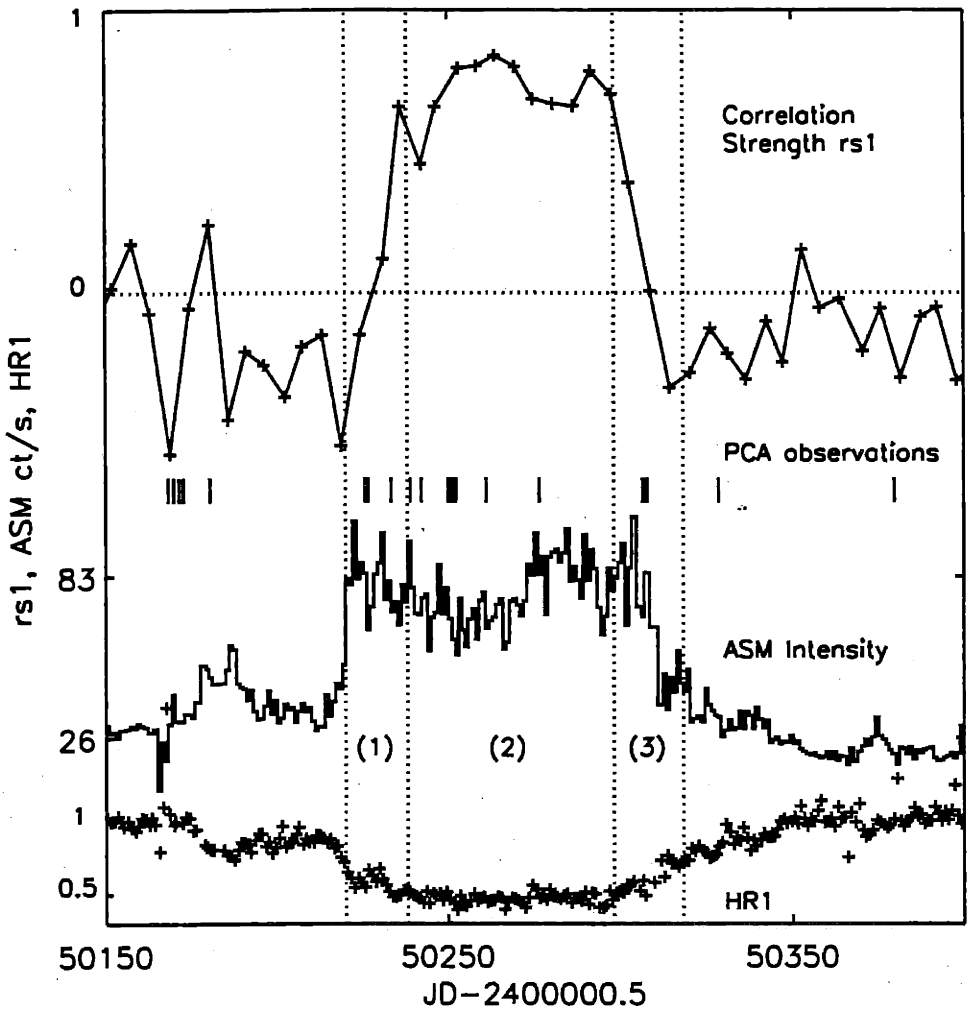

Figure 6-1 Correlation coefficients of the 1.5-12 keV ASM count rate and the hardness ratio HR1 for 90 s time bins and a 5.6 day correlation interval (see text). Also shown are the ASM count rate and hardness ratio HR1 with 1-day time bins. For this time bin, the typical relative uncertainty is 2% for the count rate and 5% for HR1. The PCA observations are indicated with vertical lines.

is strongly correlated in the soft state (large filled circles) but weakly anti-correlated in the hard state (small filled circles). The evolution of the flux-hardness correlation between the two states is apparent during the transition phases 1 and 3 (defined in Fig. 6-1) (open circles). These confirm the ASM results.

To investigate possible orbital effects, we separated out the hard state data at phases 0.2–0.8, where phase 0 is defined as superior conjunction of the X-ray source. The results are shown in the inset of Fig. 6-2. The anti-correlation seems to become less pronounced at low fluxes, indicating the importance of the orbital effects. On the other hand, the overall anti-correlation is still prominent, mostly due to the cluster of data points to the lower right, which come from observations 10-60 days proceeding or following the state transition (labeled with "T"). Interestingly, one group of data points is from observations of Cyg X-1 during a 50-day long soft flare that occurred about one year after the state transition (labeled with "F"). It is also worth noting that within the remaining two data groups the correlation is absent (or very weak).

Data from the higher PCA energy bands ($E > 12$ keV) show no strong correlations in all states (right panel, Fig. 6-2). There may be a slight anti-correlation in the hard state data, again mostly due to observations near the state transition and during the soft flare. This is consistent with the fact that, within each state, the general shape of the observed spectrum above $\sim$12 keV seems insensitive to the change of the flux.

6.4 Discussion

The ASM results show that the transition phases lasted for about 20 days during the 1996 state transition of Cyg X-1, as opposed to $\lesssim 7$ days as indicated by the change in the soft X-ray flux (see Fig. 1). That is, for about 20 days at the beginning and near the end of the state transition episode, the system was in a transitional process even though the soft flux was generally high. A similar conclusion was drawn by Cui et. al (1997a, 1997b) [27, 29] based on the evolution of the power density spectra

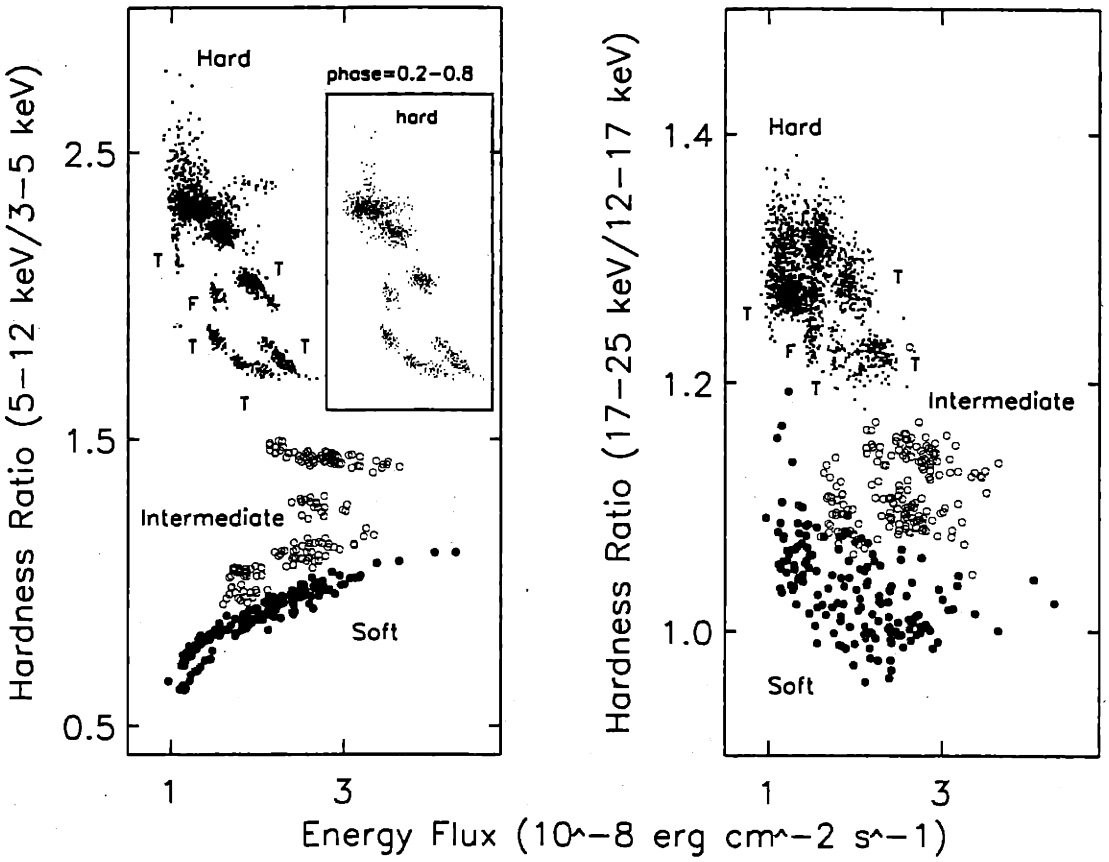

Figure 6-2 Evolution of the two PCA spectral hardness ratios with the 2.5–25 keV incident energy flux (see text). Labels "T" and "F" indicate data near the state transition and during the soft flare, respectively. The inserted window in the left panel shows the hard state data at phase 0.2–0.8 (with X-axis shifted to the right by one tick mark), where phase 0 is superior conjunction of the X-ray source.

(PDS). We therefore suggest that the spectral states of Cyg X-1 are better defined by the correlation between the soft X-ray flux and the spectral hardness of the source than by the soft flux alone.

The PCA results confirm our findings based on the ASM data. Furthermore, they reveal that the orbital effects could account for the observed negative correlations on time scales less than 5.6 days, for time periods sufficiently far away from the soft flare or the state transition. This is consistent with the fact that there is a broad absorption-like dip in the orbital light curves obtained from the ASM data, likely caused by absorption and scattering of the X-rays by the stellar wind (e.g., [145]). Our best-fit model ASM orbital light curve and hardness ratios (without noise) would yield r_{s1} to be around -0.6 with a 0.1 day time bin in a 5.6 day correlation interval. The observed correlation strength is weaker ($r_{s1} \sim -0.2$), probably reduced by noise. On the other hand, the observed positive correlation in the soft state is the opposite to what we would expect from the orbital effect. This is consistent with our previous conclusion [145] that orbital modulation is much smaller (if present at all) in the soft state.

Both the ASM and the PCA data indicate the existence of the flux-hardness anti-correlation in the hard state on time scales longer than the 5.6 day orbital period. Moreover, the hard state data near the state transition episode and during the soft flare both contribute to this observed anti-correlation in a similar fashion (Fig. 6-2). The PCA spectral fitting indicates that these observations also share similar spectral properties, which deviate somewhat from that of typical hard state data (see data section). This seems to lend support to the notion that soft flares are "failed" state transitions. Similar soft flares occur randomly on time scales of months to years in the ASM light curve. We therefore conclude that the anti-correlation in the hard state on time scales longer than the orbital period is intrinsic to the source and is probably related to the mechanism that causes the state transition.

Models employing a simple disk–corona geometry predict that, as the mass ac-

cretion rate through the disk increases, the soft X-ray flux increases, which provides more seed photons for the inverse-Comptonization process and thus cools the hot electrons in the corona. This would be manifested observationally as the "pivoting" of the energy spectrum of the source. Such spectral pivoting is known to occur in Cyg X-1 during a state transition (e.g., [82, 154]), and the pivoting energy is in the range of 10–20 keV. This may explain the observed flux-hardness anti-correlation at low energies (below the pivoting energy) for the state transition (and perhaps soft flares). The same might also be true for the general long-term evolution of the source in the hard state, if the pivoting phenomenon is universal (but more pronounced during a state transition). Interestingly, this may also explain the apparent lack of correlations around 12–25 keV (Fig. 6-2), since the pivoting energy is right in this energy range. Clearly, the same scenario cannot be applied to the soft state, where the correlation is observed to be (strongly) positive, unless the pivoting energy has moved to a very low energy (below the ASM pass band). Such a reduction in the pivoting energy is not apparent in our PCA data and is inconsistent with the lack of correlations in the 12–25 keV band. It is, therefore, likely that different physical processes are involved in the soft state (see [152] for a follow-up investigation of possible models).

Li, Feng, & Chen (1999) [81] discovered similar correlations between the count rate and hardness for Cyg X-1, using the PCA data, but on much shorter time scales (0.01–100 s) and with little coverage in the hard state. In their study, they chose two energy bands: 2–6 keV and 13–60 keV, from which the hardness ratio was derived. Such a choice of energy bands unfortunately masks the difference in the correlations between the count rate and the spectral shape above and below 12 keV for the soft state. Using the BATSE data (20-200 keV), on the other hand, Crary et al. (1996) [24] did see a lack of correlation between the 45–140 keV energy flux and the photon index within both data groups of high and low flux, which were presumed to correspond to the hard and soft states, respectively. However, they did not have the necessary soft-X-ray data to see the count rate-hardness correlation that we found. In this

regards, our work bridges critical gaps in those two investigations and provides new insight into the overall spectral behavior of this system.

Chapter 7

X 1908+075: An X-ray Binary with a 4.4 day Period

7.1 Introduction

X-ray surveys have consistently indicated the existence of a moderately bright X-ray source near the galactic longitude 41.97° and latitude −0.80°. This source, which we refer to as X 1908+075, was cataloged as 4U 1909+07 in the results from *Uhuru*, the first earth-orbiting mission dedicated to celestial X-ray astronomy [39]. Subsequent determinations were cataloged as 1M 1912+077 with MIT/OSO 7 [88], 3A 1907+074 with *Ariel* 5 [140, 4], 1H 1907+074 with *HEAO* A-1/LASS [151], GPS 1908+075 with *EXOSAT*/ME [141]. There are large uncertainties in the position determinations of these survey instruments, as shown in Fig. 7-1. The *HEAO* A-2 experiment on *HEAO*-1 scanned this region and detected X-ray flux of $\sim$ 13 mCrab in the 1.5–20 keV band (HEASARC archival data). The source was also detected with the modulation collimator experiment (*HEAO* A-3) on *HEAO*-1, with an 8σ detection in each of the two collimators for the energy range of 3–13 keV (HEASARC archival data). The *HEAO* A-3 instrument yields a multiplicity of relatively precise error regions which appear as a grid of diamonds in Fig 7-1.

The *Einstein* Imaging Proportional Counter (IPC) imaged a portion of this region and detected a source, 1E 1908.4+0730, the brightest source in the center of the field, at a significance level of $\sim 7\sigma$ (HEASARC archival data). The IPC flux is about 0.3 mCrab (0.5–3.5 keV), possibly highly attenuated by interstellar absorption (see Table 7-1). The position (J2000) is $\alpha = 19^h10^m46^s$ and $\delta = +07°36'07''$ with a positional accuracy of 50″. This position overlaps one of the *HEAO* A-3 "diamonds". There are a few other 5-σ detections at the edge of the field of view (1° square) of the IPC, and these sources are located well beyond the celestial map provided in Fig. 7-1. Furthermore, none of these sources have positions that are consistent with the *HEAO* A-3 diamonds. It is thus highly likely that the *Einstein*/IPC detection represents the same source as the X-ray survey detections. No optical counterpart has been identified within the error circle of 1E 1908.4+0730.

The X-ray spectra and flux available from the hard X-ray survey detections are roughly consistent with each other as summarized in Table 7-1. The fluxes are about 5 mCrab in the 2–6 keV band and 7–14 mCrab in the 2–20 keV band. The spectrum obtained form an *EXOSAT*/ME observation of 4U 1909+07 in the 1–15 keV band (at the *Uhuru* position) indicates excessive absorption at photon energies below 6 keV compared with that of the Crab Nebula (HEASARC archival data). The observations from the *Ariel* 5 spectrometer show that 3A 1907+074 has a hard spectrum which can be fitted with a power law of photon index 1.6 ± 0.15, hydrogen column density of $3^{+1.5}_{-1.2} \times 10^{22}$ cm^{-2}, and an iron line emission with equivalent width 660 ± 220 eV [4]. None of these pointed observations were long enough to investigate the long-term variability of this source.

In this paper, we use the data from the All Sky Monitor (ASM) [76] on board *RXTE* [10] to confirm the position and to study the nature of X 1908+075. We show that the coded mask patterns for the ASM, processed for the *Einstein*/IPC position, yield a persistent $\sim$ 8 mCrab X-ray source with a coherent 4.4-day periodicity for over 3 years. We then discuss the implications of this discovery.

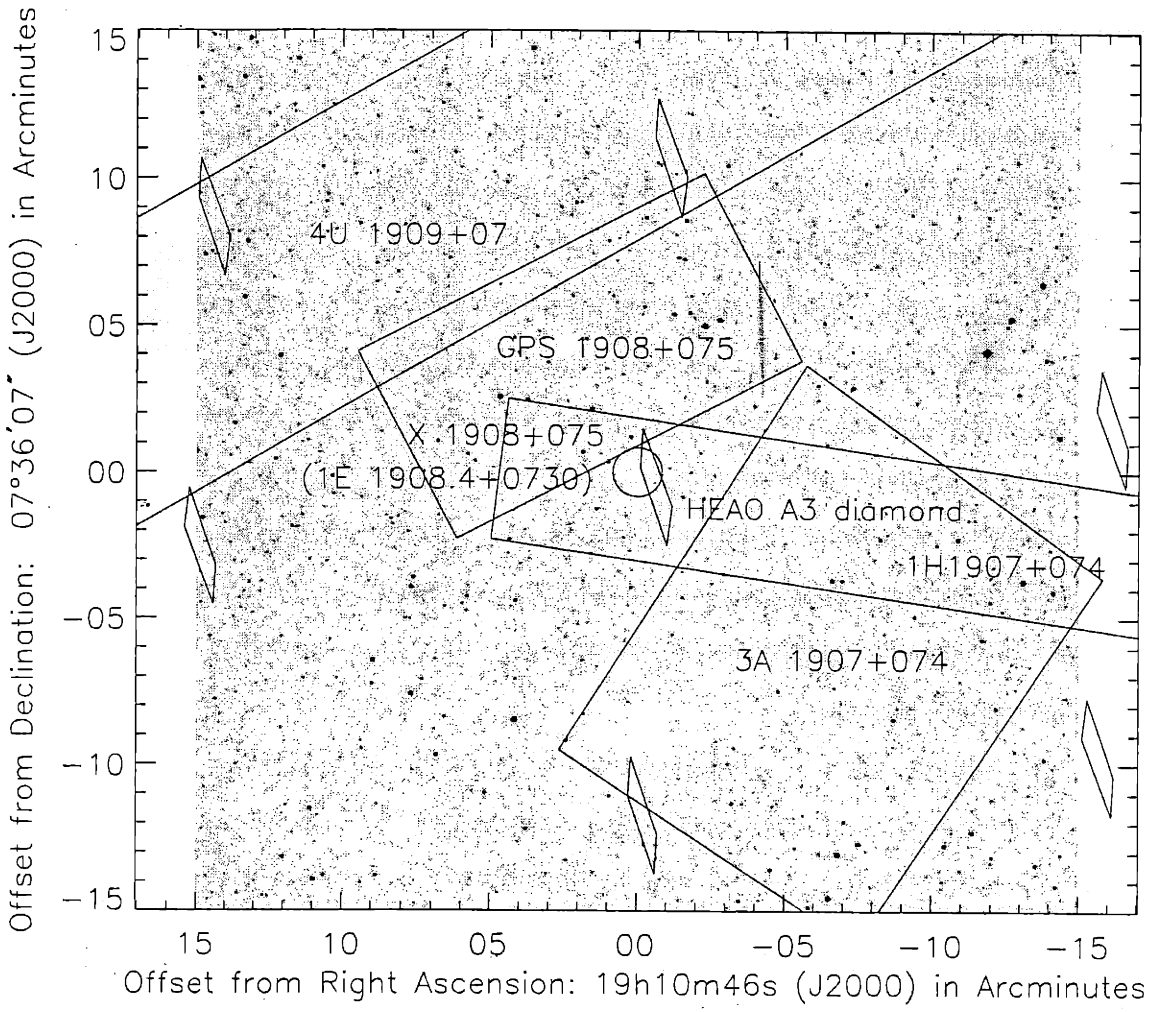

Figure 7-1 Positions of X 1908+075 and other X-ray sources detected previously, with reported error boxes superposed on an optical image taken from the Digitized Sky Survey. The degenerate positions determined with *HEAO* A-3 can be seen as a grid of diamonds. The position of X 1908+075 used in the ASM analysis was taken to be that of *Einstein*/IPC source 1E 1908.4+0730, represented as a small circle.

7.2 Analysis and Results

The X-ray light curve from the ASM observations of X 1908+075 (1996 March to 1999 January) is shown in Fig. 7-2. The intensity points are 5.0-d averages of the intensities derived from the individual 90-s dwells for the assumed position of the *Einstein*/IPC source. It is apparent that X 1908+075 has generally persisted at an intensity level of about 0.6 ct/s, or 8.0 mCrab in the 1.5-12 keV band for about three years. The spatial response function of the ASM implies that these photons arise within 12 arcmin of the *Einstein*/IPC source position, thus confirming its association with X 1908+075. The average X-ray intensity of X 1908+075 is well below the detection threshold (30 mCrab) for a single camera exposure of the ASM. The effort to determine an independent source position using ASM data alone, e.g., with the superposition of cross-correlation maps, would be limited by the appearance of systematic noise features with amplitudes that are a substantial fraction of the average source intensity.

The average values of the hardness ratios of X 1908+075 are HR1=1.0 $\pm$ 0.2, HR2=3.6 $\pm$ 0.3 respectively, where HR1 is defined as the ratio of the ASM count rate in the 3–5 keV band to that of the 1.5–3 keV band, and HR2 is the ratio of the count rate in the 5–12 keV band relative to that of the 3–5 keV band. X 1908+075 has a much harder X-ray spectrum than either the Crab Nebula (HR1=0.9, HR2=1.1) or Cyg X-1 in the low-hard state (HR1=1.0, HR2=1.5). This large value of HR2 mostly resembles that of the X-ray pulsars detected with the ASM, such as Vela X-1 (HR2=3.6) and OAO 1657-415 (HR2=3.1). The black hole candidates and the X-ray bursters generally have much smaller values of HR2 (< 2.0).

Periodicities of X 1908+075 were sought by means of Lomb-Scargle periodograms of both the light curves and the derived hardness ratios. The Lomb-Scargle periodogram [83, 119, 104] was used for the calculation instead of the Fast Fourier Transform (FFT) since the ASM data points are unevenly spaced in time. With this periodogram, a maximum in the power occurs at the frequency which gives the least

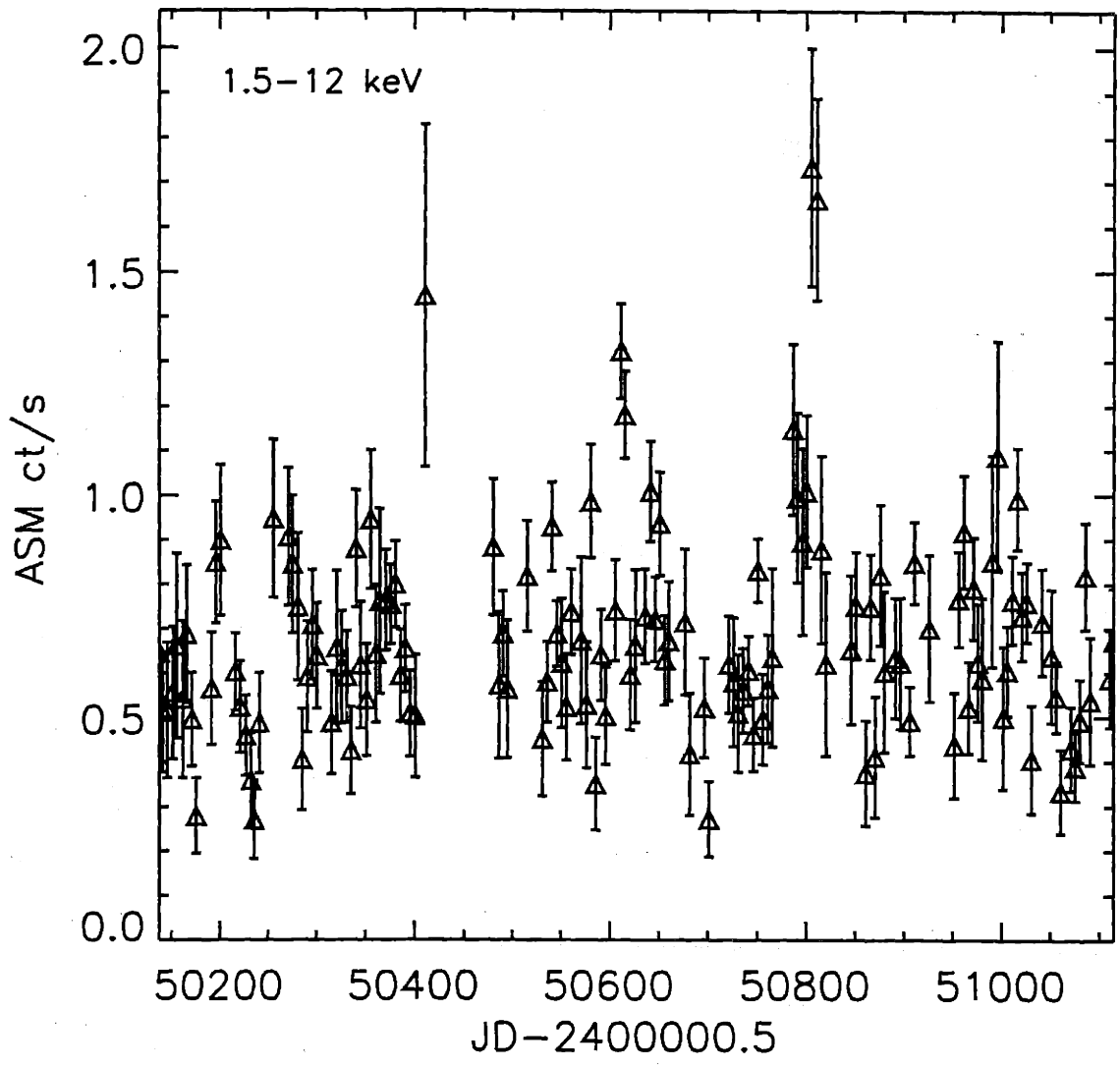

Figure 7-2 *RXTE*/ASM light curves of X 1908+075 for the period 1996 February to 1998 November. The data are binned in 5.0-day bins. Only 5σ detected data points are plotted. MJD 51000 (MJD=JD-2400000.5) corresponds to 1998 July 6. There is a persistent X-ray emission at $\sim$ 0.6 ct/s (8 mCrab) for 3 years.

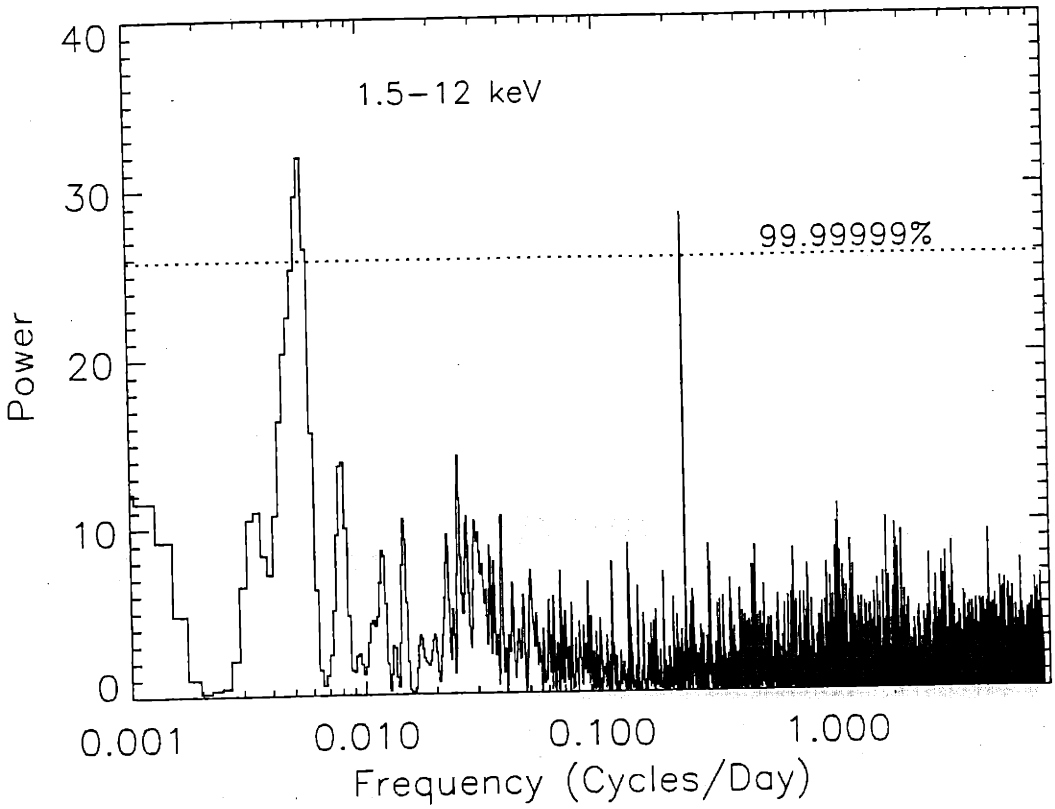

Figure 7-3 The Lomb-Scargle periodogram of the light curves of X 1908+075. The dotted line indicates the 99.99999% confidence level assuming an exponential distribution of the noise powers. There is a distinct peak at 4.4-d period. The 180-d period is probably caused by scattered solar X-ray contamination.

squares fit to a sinusoidal function. The expected average power for random noise is 1.0. We oversampled the power spectrum so that the frequencies are a factor of 4 more closely spaced than $1/T$, where T is the total duration of the data used. The goal is to ensure the detection of a peak for a signal that is of marginal statistical significance and to best locate the peak. The result is shown in Fig. 7-3.

There is a distinct narrow peak in the power spectra at a frequency that corresponds to a period of 4.400 d. The width of the power peak is 0.009 d, consistent with that of a pure sinusoidal wave. The uncertainty of this period is estimated to be

0.001 d, assuming a single signal with Gaussian noise. With 3 years of coverage, the uneven data spacing would not degrade the uncertainty to any noticeable degree [56]. If we assume the noise follows an exponential distribution as expected for random noise, the false-alarm probability of this detection is less than 10^{-7}. In addition, there is a low-frequency peak corresponding to about 180-d period. Except for these two peaks the overall power is flat with an average of about 1.06.

The detected 180-d period seems to be caused by scattered solar X-ray contamination. We found from the ASM light curve that three major flares happened at the times when the sun was near the field of view of this source, while flares with smaller amplitudes are evident when the sun is 180° away from the source position. The latter may be caused by the back-scattering of the solar X-rays off the earth's atmosphere and the instrument.

We have also conducted another independent periodicity search using the epoch folding technique [73, 30]. The data were folded modulo a trial period and then grouped by phases. The resulting deviation from uniform random noise can then be detected using a χ^2 test. For periods between 0.01–7 days, a distinct peak indicating the maximum deviation was found around 4.400 d with $< 10^{-6}$ false alarm probability. This is consistent with the results of the Lomb-Scargle periodogram.

The data were then folded modulo the period of the best-fit value of 4.39986 days from the Lomb-Scargle periodogram to study the intensity variations with phase (Fig. 7-4). The most distinctive feature in the folded light curves is the nearly sinusoidal modulation of large amplitude. We fitted a sinusoidal wave plus a constant to the folded light curves. The best fit yields a $26 \pm 3\%$ amplitude of the sinusoidal wave in the 1.5–12 keV band, $51 \pm 14\%$ in the 1.5–3 keV band, $49 \pm 8\%$ in the 3–5 keV band, and $22 \pm 3\%$ in the 5–12 keV band. The best-fit epoch for the minimum flux is:

$$T_0 = 2450440.419 \pm 0.068 + n \times (4.400 \pm 0.001\ )\ \text{(JD)}$$

The persistence and coherence of this periodic variation were tested by subdividing the ASM light curves into four consecutive 250-d intervals and then searching for

Table 7-1. Historical Observations of X 1908+075

Name	Instrument	Observation Time	Energy Band (keV)	Flux (mCrab)
X 1908+075	*RXTE*/ASM	1996-present	1.5-12	7.7 ± 2.0
GPS 1908+075	*EXOSAT*/ME	1983	2-6	5.4 ± 0.5
1E 1908.4+0730	*Einstein*/IPC	1980	0.5-3.5	0.27± 0.04
1H 1907+074	*HEAO* A2	1977	1.5-20	13.1 ± 0.1
3A 1907+074	*Ariel* 5/SSI	1977	2-10	8 ± 4
4U 1909+07	*Uhuru*	1971–1973	2-6	4.9 ± 0.5

Note. — Data were taken from the HEASARC archive. Each count rate was normalized with respect to that of the Crab Nebula detected by the same instrument in the specified energy band. The errors were estimated based on the given values and scatter of the measurements.

Table 7-2. Sinusoidal Modulations of X 1908+075

Time range (d) [a]	Fractional Amplitude (%)	$\Delta\phi$ [b]	χ^{2c}_{ν}
0–250	31.0 ± 7.4	0.046 ± 0.034	0.9
250–500	25.9 ± 5.4	-0.011 ± 0.032	0.8
500–750	22.7 ± 10.0	-0.065 ± 0.077	2.0
750–1000	30.0 ± 5.6	0.029± 0.028	0.9

[a] The start time is 2450088.871 (JD)

[b] Difference between the best-fit phase 0 and the epoch given in the text. The error for interval 500–750 d was multiplied by a factor of 2 to take into account of the large value of χ^2

[c] Reduced Chi-square with 12 degrees of freedom

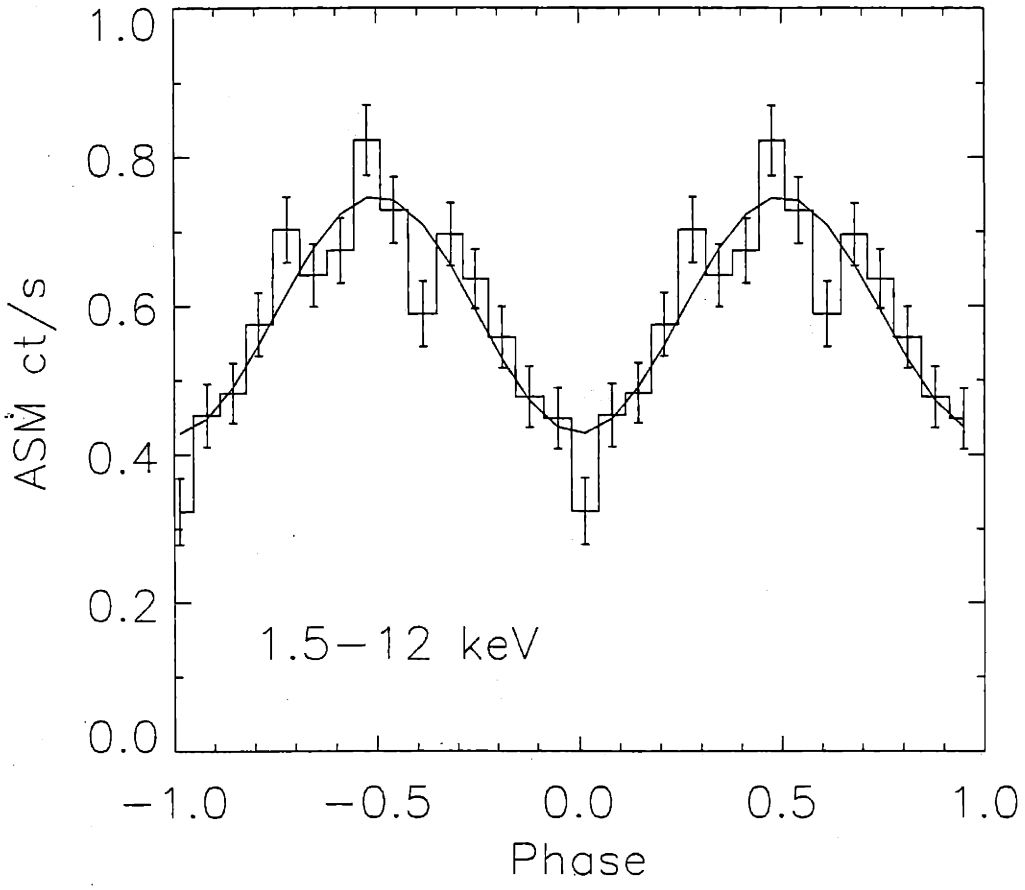

Figure 7-4 Folded light curve of X 1908+075. Observational data points are represented as histograms. Phase zero is defined as the phase of the minimum X-ray flux. The error bars represent one standard deviation. The solid line is the best-fit sinusoidal wave. The most distinctive feature is the nearly sinusoidal modulation with large amplitude.

periodicities. The same analyses described above were applied to each of the 250-d light curves. In the calculated power density spectra, the signals are still visible as narrow peaks near $P = 4.40$ d in the power density spectra even though they are no longer independently significant. The best-fit amplitudes and phases of the sinusoidal waves are roughly consistent with each other (see Table 7-2 for a summary). We thus conclude that the modulation is persistent and coherent over the 3-year time interval.

7.3 Discussion

The X-ray emission detected by the ASM has been found to arise from the immediate region of the *Einstein*/IPC source, to exhibit a hard spectrum and intensity similar to the historical survey detections, and to be persistent over $\sim$ 3 years. This together with the *Einstein* IPC and *HEAO* A-3 positional correspondence strongly suggest that the position of 1E 1908.4+0730 is the accurate location of the sources seen in the historical X-ray surveys.

It is natural to link the observed 4.4-day period of X 1908+075 to the orbital period of a binary. The periods of X-rays from known sources are believed to be associated with one of the following [148]: (1) rotational periods of neutron stars in X-ray pulsars, ranging between milliseconds to hundreds of seconds; (2) orbital periods of binary systems, ranging from tens of minutes to tens of days, and possibly hundreds of days; and (3) "superorbital" orbital periods from $\sim$ 30 days to hundreds of days, which in some cases are believed to be the precession period of the accretion disk (e.g., [77]). It is clear that the coherence and the timescale of the 4.4-day X-ray oscillation in X 1908+075 can be best interpreted as the orbital period of a binary system.

We can then picture X 1908+075 as a binary system consisting of a compact object and a mass-donor companion star. An X-ray binary with a low mass companion (LMXB) is unlikely the scenario for X 1908+075, since the known orbital periods of

most LMXBs [148] are on the order of hours, much shorter than the detected 4.4 days. There are only a few known LMXBs having orbital periods longer than a day, among them only Cir X-1 ($P \sim 16.6$ d) and Her X-1 ($P \sim 1.7$ d, a possible LMXB) exhibit orbital modulations in X-rays. The modulation in X-rays of Cir X-1 manifests itself as periodic flares and dips likely due to a highly eccentric orbit, while Her X-1 is an eclipsing system. Such dramatic modulations are not evident in the orbital light curves of X 1908+075. On the other hand, most HMXBs have orbital periods on the orders of days. The smooth and nearly sinusoidal modulations in X 1908+075 have a lot in common with supergiant systems such as Cyg X-1. We therefore suggest that X 1908+075 is a high mass X-ray binary (HMXB).

We further suggest that the companion star is a supergiant rather than a Be star for the following reasons. (1) The 4.4-d orbital period fits in the range favored more by supergiant systems than by Be-star systems, as the known orbital periods of the latter are much longer than 4.4 days ($\geq$ 16.7-d) [148]. (2) The known orbital light curves of Be-star systems are all outburst-like rather than sinusoidal (e.g., EXO 2030+375), probably due to the enhanced accretion caused by the the compact object's periastron passage around the Be star. (3) The orbital modulations of supergiant systems are known to be persistent while this is generally not true in Be-star systems (e.g., 4U 0115+63 in ASM light curves during 1996 March to 1998 November).

The smooth and roughly sinusoidal orbital modulation in the X-rays of X 1908+075 suggests that the system could be embedded in a strong stellar wind from the companion star (e.g., a supergiant O or B star), which absorbs and scatters the X-rays. The X-ray modulation is then caused by changes in the optical depth along the line of sight to the X-ray source as a function of orbital phase. For X 1908+075, absorption of X-rays probably dominates over scattering, as the amplitude of the modulation in the 1.5–5 keV band is larger than in the 5–12 keV band. To explain a modulation with an amplitude of nearly $\sim$ 22% in the 5–12 keV band, the difference in the hydrogen column densities between phases 0 and 0.5 is expected to be more than 10^{23} cm^{-2}

for an absorption and scattering process. The mechanism of the orbital modulation of X 1908+075 could be very similar to that of Cyg X-1, wherein hard state orbital modulation in the ASM light curves can be well explained with absorption and scattering in a stellar wind [145]. Another example of such a system could be the newly discovered X-ray pulsar XTE J1855-026 [19]. In this system, the orbital period is proposed to be 6.1-d as detected by the ASM. The modulation is roughly sinusoidal with an amplitude about 23% in the 1.5–12 keV band. It has also been proposed as a supergiant wind accretion system.

The hydrogen column density n_H can be used to estimate the optical extinction in the V band using the empirical relation between the n_H and the color excess E_{B-V} [118]. It is found that $A_V = 15$ for $n_H = 3 \times 10^{22}$ cm^{-2}, as indicated from the *Ariel* 5 observation of 3A 1907+074. The optical objects within the *Einstein*/IPC error circle have magnitudes $V \geq 19$ in the Palomar sky survey. To estimate the distance to X 1908+075, we first investigated the possible range of the absolute V-band magnitudes M_V (from [70]) known for supergiant stars in binaries with known orbital periods. We found that $M_V \leq -5.2$. Together with $A_V = 15$ and $V \geq 19$, we obtained 0.7 kpc as the lower-limit for the distance. The X-ray luminosity, estimated from the ASM count rate (1.5–12 keV), is then $L_{1.5-100keV} \geq 5 \times 10^{34}$ erg s^{-1} if we assume the *Ariel* 5 spectrum. Given the A_V value, a more likely scenario is a distance $\sim$ 7 kpc estimated from the formula provided by Allen (1973) [2], where the relation between the extinction of the star light near the galactic plane and the distance is estimated based on the average properties of interstellar absorbing clouds and the grains between them. We obtained similar distance by comparing directly the n_H value of X 1908+075 with that of another galactic plane source GRS 1915+105, which is 3° away from X 1908+075 and is believed to have a kinetic distance of 12.5 kpc and $n_H = 5 \times 10^{22}$ cm^2 [17]. At the distance of 7 kpc, the estimated X-ray luminosity of X 1908+075 is $L_{1.5-100keV} \sim 5 \times 10^{36}$ erg s^{-1}.

Finally, the nature of the compact object is yet to be determined. As mentioned

in the previous section, the large HR2 value of X 1908+075 suggests an X-ray pulsar and therefore a neutron star system. This remains to be confirmed using future *RXTE*/PCA observations which provide better timing and spectral resolutions.

7.4 Conclusions

Persistent hard X-ray emission ($\sim$ 8 mCrab at 1.5–12 keV) from X 1908+075 has been detected with the *RXTE*/ASM at the *Einstein*/IPC position of $\alpha = 19^h10^m46^s$, $\delta = 7°36'07''$ (J2000) for a 3-year period. A 4.4-d period has been discovered from the ASM light curves. The modulation is nearly sinusoidal, persistent and coherent for 3 years. The amplitude of the best-fit sinusoidal wave is $26\pm3\%$ in the 1.5–12 keV band. Our results support the simple interpretation that X 1908+075 is the same source as 4U 1909+07, 3A 1907+074, 1H 1907+074, GPS 1908+075, 1E 1908.4+0730, as well as the source detected by *HEAO* A-3. We argue that the 4.4-d period is the orbital period of a high mass binary system. We also suggest that this system consists of a neutron star and a supergiant star that produces a strong stellar wind. The X-ray modulation is then caused by changes in the optical depth along the line of sight to the X-ray source as a function of orbital phase.

Chapter 8

XTE J1716-389: A System with a 98-day Period

8.1 Introduction

The X-ray source XTE J1716-389 is probably the same source as KS 1716-389. KS 1716-389 was discovered in 1994 with the TTM X-ray telescope aboard the orbiting Mir-Kvant module [1]. Like the ASM, the TTM X-ray telescope consists of a coded aperture and a position-sensitive detector. During 17 days of observation with the TTM, the 2–27 keV flux of this source was found to vary between 20 and 80 mCrab with an average flux of 47 ± 4 mCrab. The total energy spectrum was best fit by a power law with a photon index of -3.5 ± 0.5 for a hydrogen column density $n_H = (1.2 \pm 0.5) \times 10^{23}$ cm^{-2}. The position of KS J1716-389 was found [1] to be $\alpha = 17^h15^m59^s$, $\delta = -38°53'$ (at epoch 2000.0) with a positional accuracy of $1.5'$. The source lies in Scorpius, at an angular distance of 11° from the Galactic Center.

A source (1RXH J171556.7-385150) was detected within the error circle of KS J1716-389 with the *ROSAT* High Resolution Imager (HRI) in 1997. The position of the source was found to be $\alpha = 17^h15^m56.7^s$, $\delta = -38°51'51''$ with an accuracy of $1''$ (at epoch 2000.0) [138]. Within $30'$ of this position, no other X-ray source was found.

The 0.1–2.4 keV flux was found to be 4.5 $\times 10^{-13}$ erg cm^{-2}s^{-1} if the source spectrum is a power-law with photon index of -3. Prior to 1997, little else was known about this source.

KS J1716-389 was then "re-discovered" [112] as XTE J1716-389 in 1997 in an *RXTE* All Sky Monitor (ASM) deep skymap. A position was derived that was later found to be consistent with that of KS 1716-389 and the *ROSAT* source. An ASM light curve extending over 4.5 years have been derived for the *ROSAT* position. In this chapter, we present a detailed study of this source with over 4.5 years of *RXTE*/ASM observations and 300 ks of PCA observations that sampled this source uniformly at $\sim$ 10 d interval for one year. Throughout this paper, the name XTE J1716-389 will be used. We present our discovery of intensity dips that exhibit a 98-d periodicity and also the spectral and timing evolution during the dip. The nature of this system will be discussed.

8.2 ASM Analyses and Results

The ASM light curve (Fig. 8-1) shows the source to have generally maintained an intensity of $\sim$ 25 mCrab for over 4.5 years (1996 March – 2000 November). Despite its relatively low intensity, the source exhibits prominent dips in the ASM light curve approximately every 100 days (indicated by vertical lines). During these dips, the intensity may decrease to less than 10% of the average count rate. The total duration of a dip may be as much as $\sim$40 days (FWHM). Several of the dips are missing, which leads to a few 200-d intervals.

A 97.51 $\pm$ 0.12 d period is detected in a Lomb-Scargle periodogram with a false alarm probability less than 3×10^{-7} (Figure 8-2). The signal power is narrow (with a FWHM of 5 days), indicating a detection of a highly periodic modulation. The uncertainty of the period is the estimated standard deviation assuming a single sinusoidal signal with Gaussian noise [56]. The first harmonic is also visible. No other

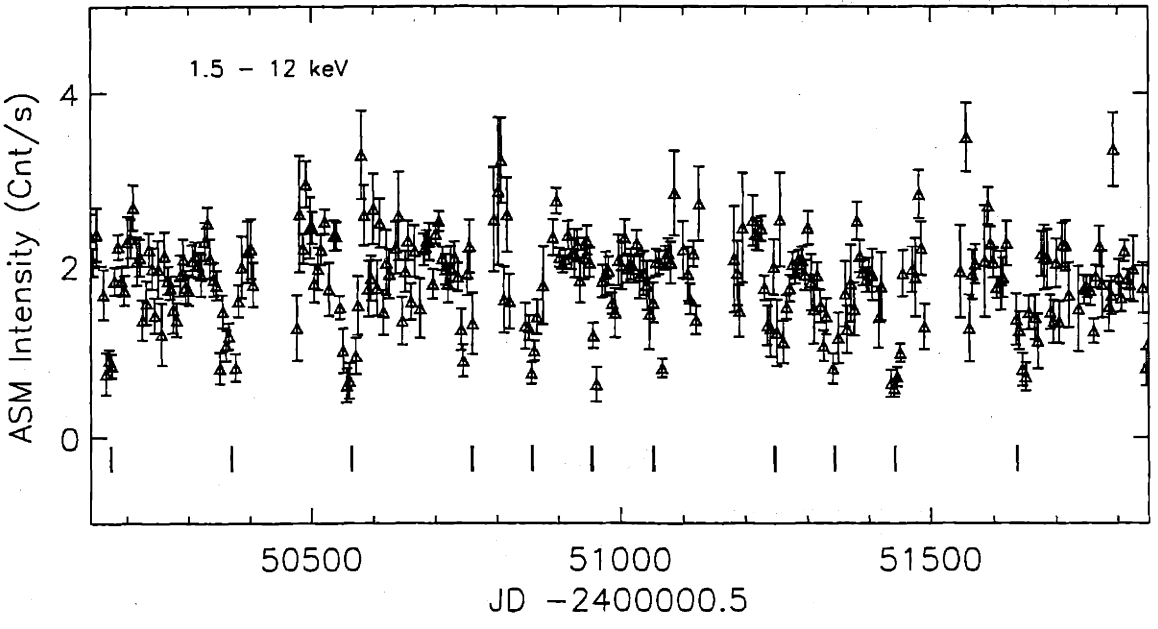

Figure 8-1 RXTE/ASM light curve of XTE J1716-389. XTE J 1716-389 has generally maintained an intensity of ~25 mCrab for over 4.5 years. The data are binned in 5-day bins. Only data of 3σ detection and of errors < 1cnt/s are shown. Broad dips are apparent in the light curve for every ~100 days, sometimes every ~200 days.

periods have been detected in the ASM data for frequencies of 0.001–35 cycles per day (with known artifacts excluded).

The ASM light curve folded at the period $P = 97.51411$ d is shown in Figure 8-3. A broad dip is apparent in the folded data. The width of the dip is about 40% (FWHM) of the cycle. The dip profiles are quite symmetric about the minimum intensity. The transition to the dip appears to be sharp for energies > 3 keV, during which there is a $\sim$45% drop in the intensity within 15% of the cycle at 3–5 keV band. The fractional amplitudes of the dip relative to the average non-dip intensities (phase 0.3–0.7) are 48% for 1.5–3 keV, 60% for 3–5 keV, and 43% for 5–12 keV. This can not be explained by simple absorption of X-rays by un-ionized intervening matter, as such a model would predict 100% absorption in the 1.5–3 keV band for 43% modulation in the 5–12 keV band. This is also apparent in the (soft) hardness ratio HR1, the spectrum softens around the dip, opposite to what one expects for absorption. The ephemeris for the minimum of the dip is:

$$T_n\,(\mathrm{MJD}) = 50174.24 \pm 0.72 + n \times (97.51 \pm 0.12). \qquad (8.1)$$

This minimum is defined as that of a sinusoidal wave best-fit to the data with the Levenberg-Marquardt (L-M) method [104] which utilizes the χ^2 minimization. The uncertainty for T_n is the estimated standard deviation from the fit.

8.3 PCA Analyses and Results

We carried out 45 pointed PCA observations roughly 1–2 times every 10 days between 1999 January and 2000 January. They provided uniform coverage of three complete cycles of the 98-d period. Each observation lasts 400 s to 10 ks (typically 1 ks).

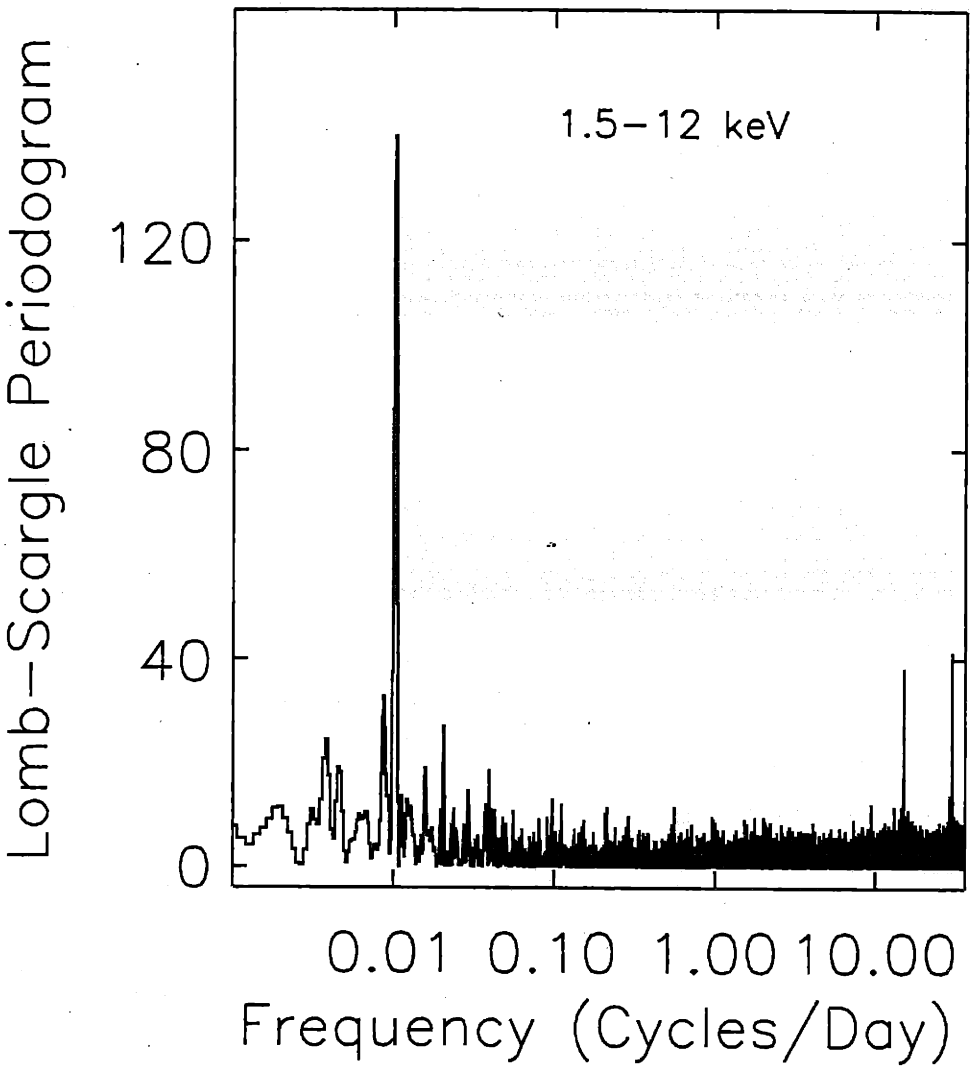

Figure 8-2 The Lomb-Scargle Periodogram of the light curve for XTE J1716-389. A ~98 d peak is apparent. The peaks at 15 cycles per day and at 30 cycles per day are due to the 96 min *RXTE* orbital period and its first harmonic (see Chapter 4).

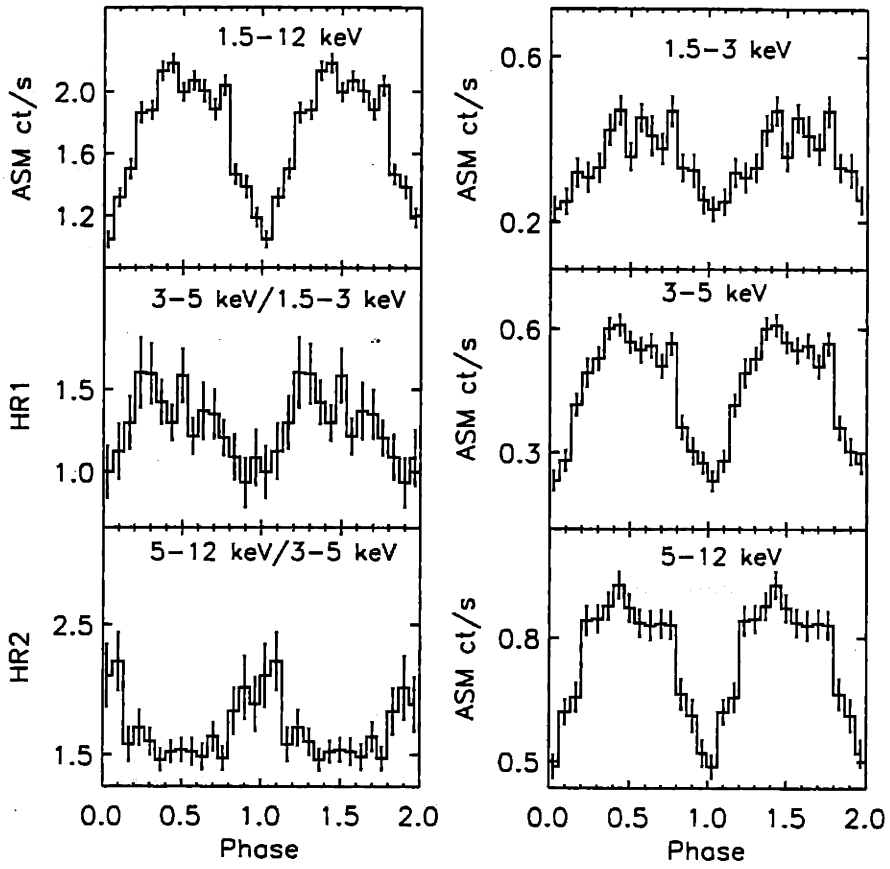

Figure 8-3 *RXTE*/ASM light curve and hardness ratios of XTE J1716-389 for $P =$ 97.51411 d.

8.3.1 Analysis

We organized the PCA observations into three groups consisting of observation sequences 1–11, 12–24, and 25–45 respectively. Each group contains data from roughly one 98-d cycle and contains one intensity dip. We refer to these groups as dip cycles 1, 2, and 3.

For each PCA observation, we use FTOOLS (v. 5.0) to construct light curves in terms of count rates vs time in the 2.5–25 keV band and in five energy bands (3–5 keV, 5–8 keV, 8–12 keV, 12–17 keV, and 17–25 keV) with 16 s time bins. The hardness ratios of the count rates between the subsequent energy bands were also calculated (5–8 keV/3–5 keV, 8–12 keV/5–8 keV, 12–17 keV/8–12 keV, and 17–25 keV/12–17 keV). We define the soft color as the ratio of the PCA count rates in the 5–8 keV band to that of the 3–5 keV band, and hard color as the ratio of the 8–25 keV band to the 5–8 keV band. Color-intensity and color-color diagrams (Figures 8-4, 8-5, 8-6) are constructed to display the relation between the 2.5–25 keV count rate and the hard and soft colors. Each diagram consists of three panels, one for each dip. Each panel contains data points of 16 s time bins from the three groups defined above, except that we omit obs. 10–11 from group 1 because of a PCA gain change occurred between obs. 9 and 10 (MJD 51259).

We also constructed one average energy spectrum for each of the 45 observations using FTOOLS (v. 5.0). The average energy flux for each observation is estimated by fitting each spectrum with a modified bremsstrahlung spectrum including an iron line at 6.4 keV (the "compLS" plus "gauss" model in XSPEC v. 10.0). We obtained a reduced chi-square statistics $\chi^2_\nu < 1.5$ for all observations. The derived 2.5–25 keV PCA energy fluxes vs. time are displayed as circles in Figure 8-7. The ASM data points rescaled to match the PCA data points are also shown this figure. The rescale factor is: 1 ASM count = 4.34×10^{-10} erg cm^{-2}, derived from the ratio of the mean PCA flux to the mean ASM count rate over the time interval MJD 51170–51510.

Typical energy spectra selected from each data group (dip cycles 1, 2, and 3)

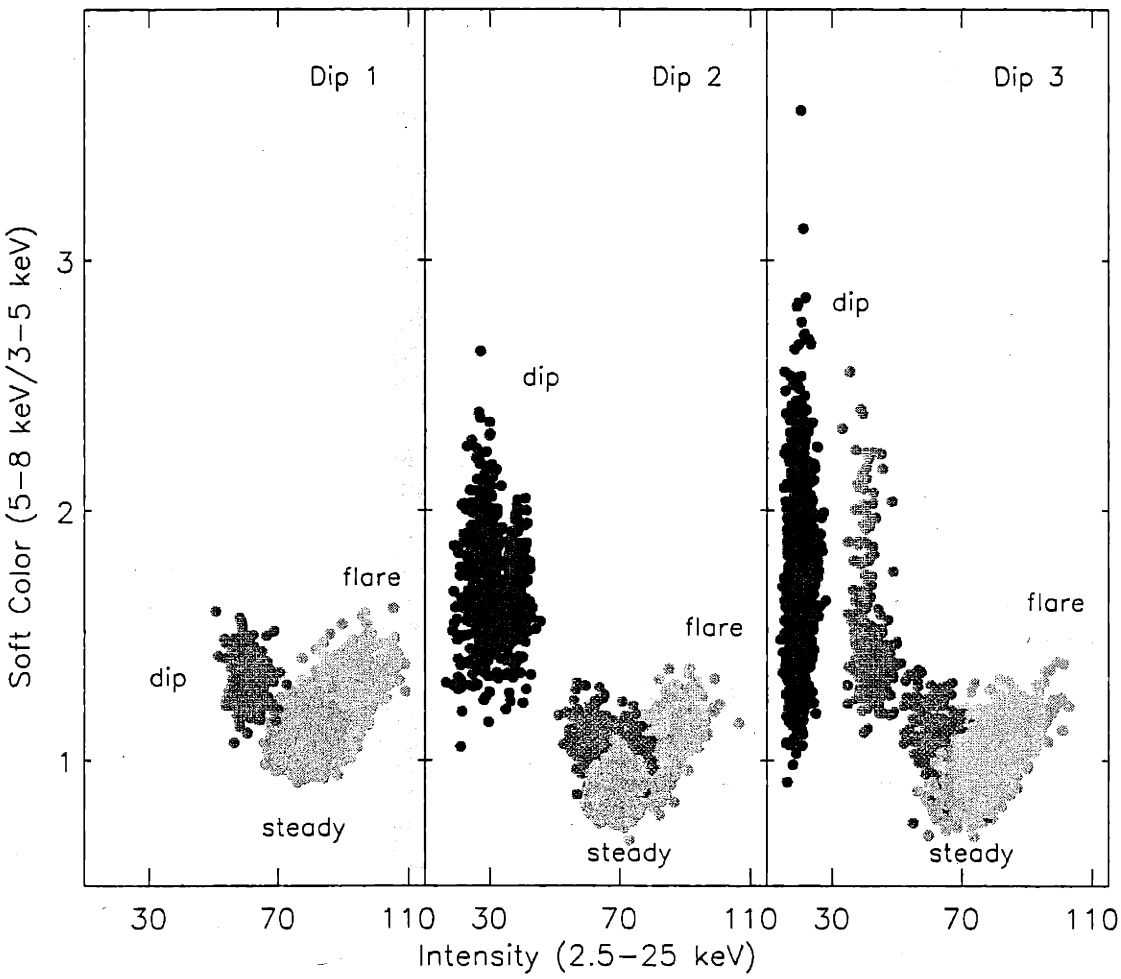

Figure 8-4 The soft color-intensity diagram of XTE J1716-389. The soft color is defined as the ratio of the count rates in the 5–8 keV band to that in the 3–5 keV band. The system follows distinct track during its flaring (the lightest shade), steady (the second lightest shade), and dipping states (two kinds of darker shade). Each point is averaged over a 16 s interval.

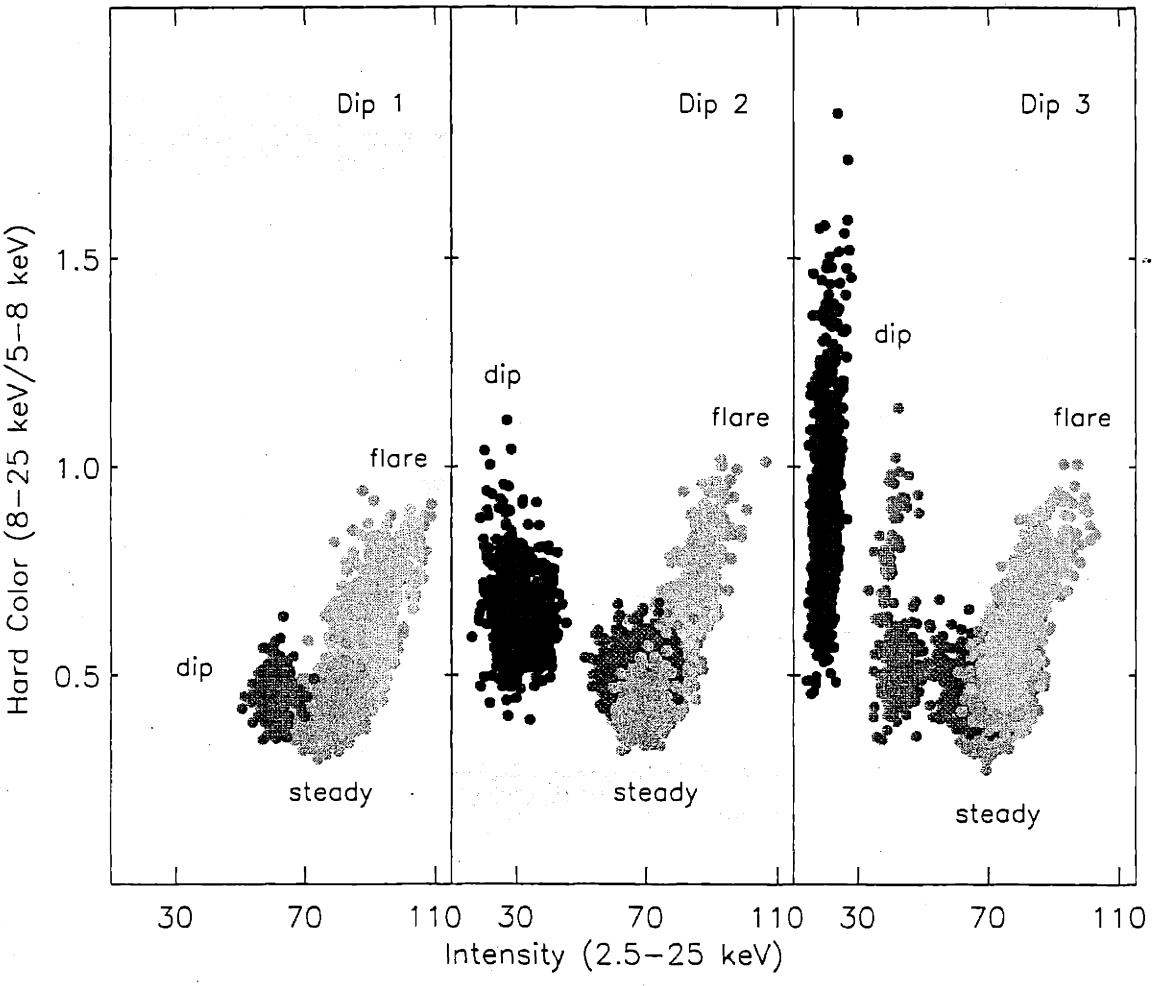

Figure 8-5 The hard color-intensity diagram of XTE J1716-389. The hard color is defined as the ratio of the count rates in the 8–25 keV band to that in the 5–8 keV band. The system exhibits similar behavior as in Figure 8-4.

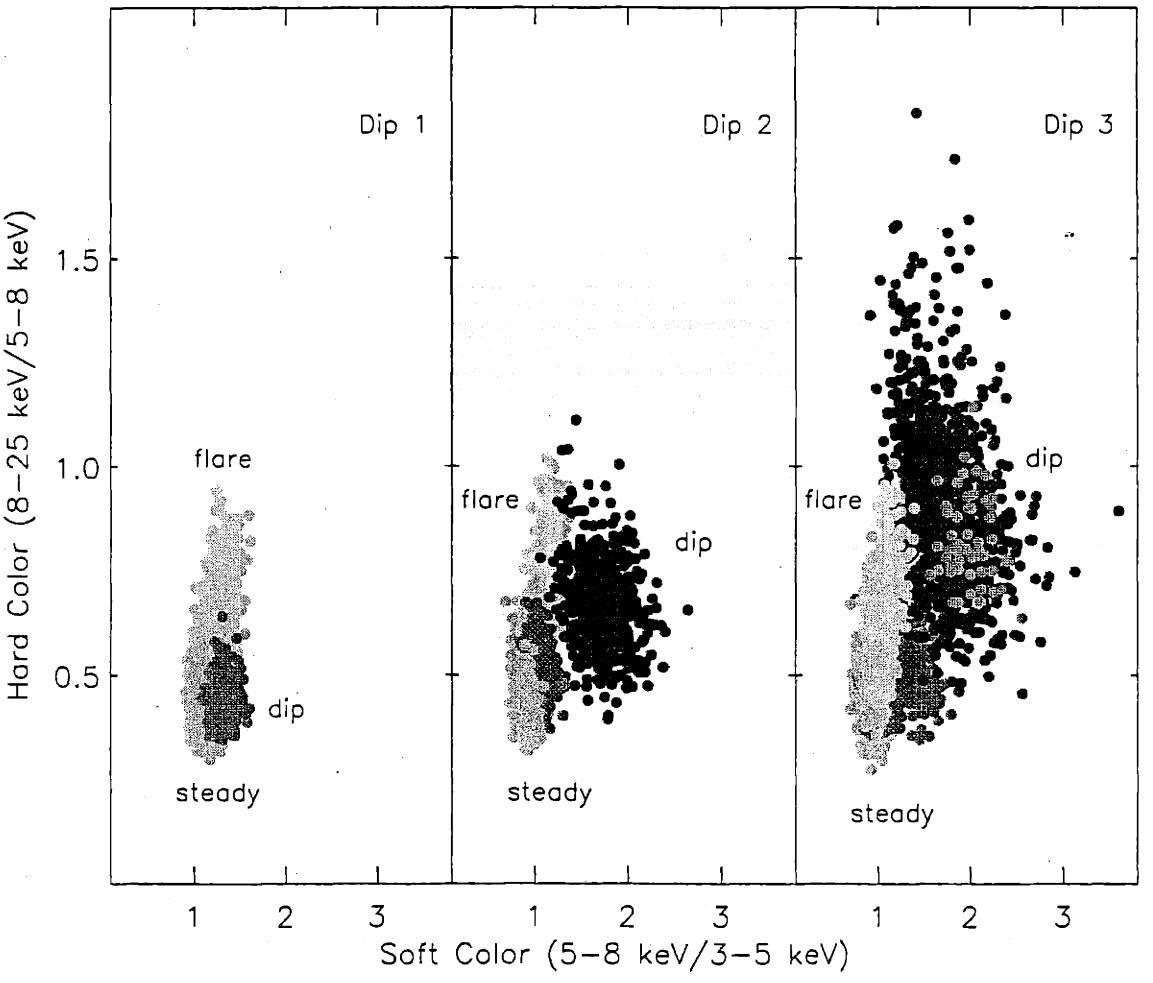

Figure 8-6 The color-color diagrams of XTE J1716-389. The data points of different states occupy distinct locations.

are shown in Figures 8-9, 8-10, and 8-11. Spectral analyses are normally conducted separately within each PCA gain epochs. We used epoch 3 response matrices for obs. 1–9, epoch 4 began after observation 9. The new epoch 4 response matrix is relatively untested and bugs were just reported 2 weeks before this writing. Thus, the detailed spectral modeling from epoch 4 data is not included in this thesis but will be published in the future. Instead, we present evolutions of the count-rate spectra within this epoch.

8.3.2 PCA Light Curve and Spectral States

The 2.5–25 keV average PCA energy fluxes vs time, derived from each of the 45 observations, are shown in Figure 8-7 together with a rescaled ASM light curve. The variation in the PCA energy fluxes traces that of the ASM light curve very well. Three broad intensity dips are apparent at times consistent with the ASM light curve. The transitions to or out of the broad intensity dips appear to be sharp. During the transitions, the 2.5–25 keV PCA flux could drop (or increase) by a factor of 3–4 within 10% of the 98-d cycle, similar to the sharp edges observed in the average ASM profile. The widths of the dips (FWHM) are consistent with that of the average ASM profile.

In addition, however, each PCA dip is seen to consist of 2–3 smaller dips which last 5–30 days (FWHM) and are separated by 10–20 d intervals. The energy flux between the smaller dips can reach the pre-dip level. The times it takes for the system to re-emerge from the bottom of the smaller dip to the pre-dip level range from $\sim$ 1.7 hours to $\sim$ 20 days. In Figure 8-7, we used two different dark shades to identify the data points within each of the three broad dips. Data points within deeper small dips are assigned the darkest shade. Those within shallower small dips and those between small dips are assigned the second darkest shade. Two light shades were assigned to data outside the dips depending on their states as discussed below.

A close examination of the variability of the PCA intensity and hardness ratios at

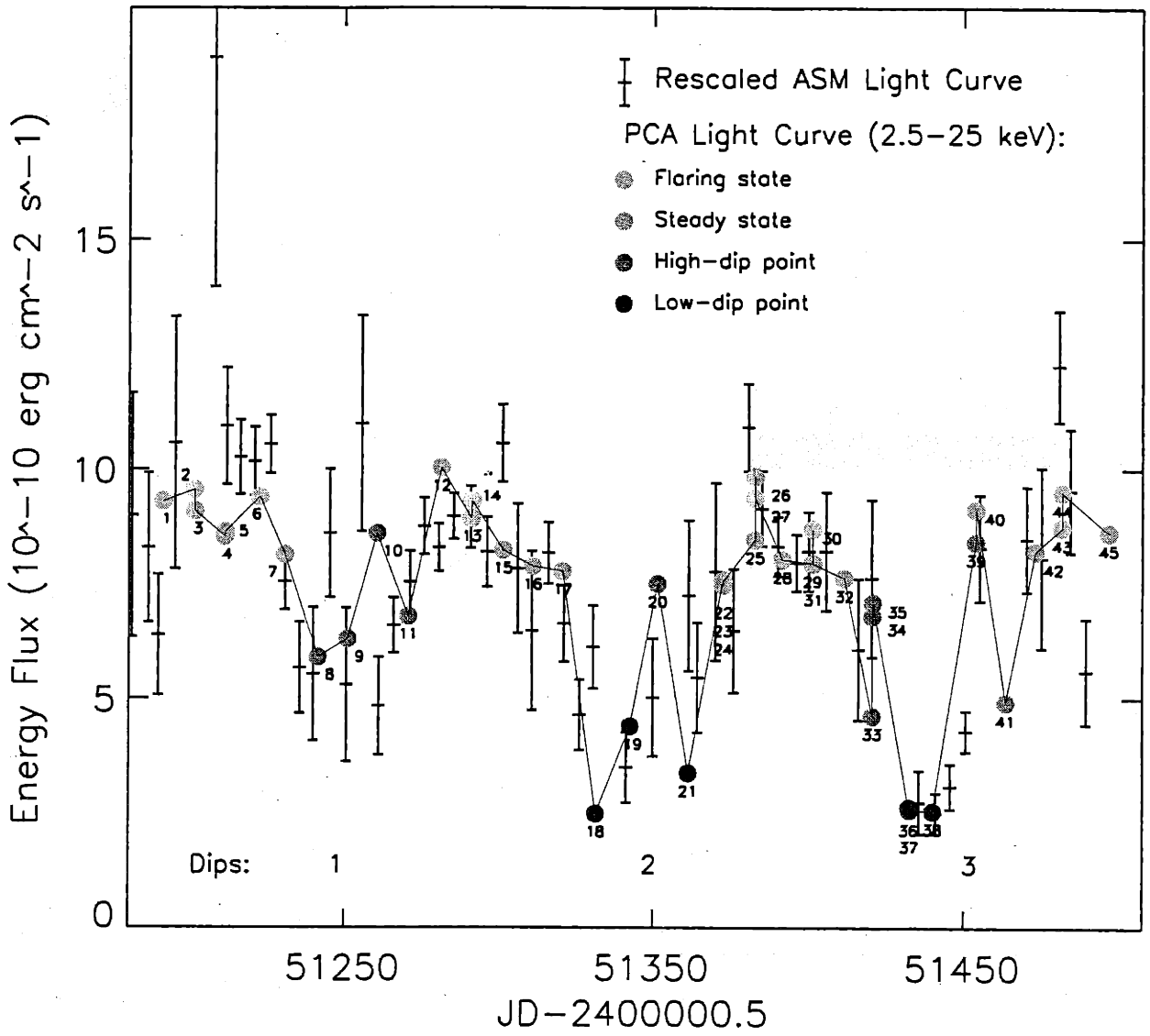

Figure 8-7 The 2.5–25 keV PCA energy flux of XTE J1716-389 vs time. The observation sequences are labeled. The rescaled ASM light curve in 5-d time bins is also plotted. Three broad dips are apparent in both light curves. The lightest, second lightest, and the two darker shades represent flaring, steady, and dipping states respectively (see text).

16 s timebins within each observation reveals that, outside the dip, the system falls into either a steady or a flaring states. In 19 out of the 28 observations outside the dip, the system exhibits the "steady" state behavior, where there is little variability in either the count rate or the hardness ratios on time scales of 16 s to a few hours. The remaining 9 PCA observations (assigned the lightest shade in Figure 8-7) exhibit hard flares in the light curves on time scales of hours. During flares, the 2.5–5 keV flux typically decreases and the 5–25 keV flux, in particular the 8–25 keV flux, increases by a factor up to 2 (see Fig. 8-8). The occurrence times of the flares seem to be randomly distributed outside the dips, independent of the phase of the 98-d period. In addition, no eclipses or periodic intensity dips have been found on time scales between 16 s and a few hours.

The soft color-intensity, hard color-intensity, and color-color behavior of this system illustrate the various behavior discussed above (Figures 8-4, 8-5, and 8-6). The shades of the 16-s data points correspond to those assigned to the observations in Figure 8-7. Data points from steady, flaring, and dipping states occupy distinct positions in the color-intensity diagrams. The flaring state data points tend to have higher intensity and are harder. There is an apparent positive correlation between the count rate and the colors. The correlation is more pronounced for the hard color. The steady state data have overall softest color and intermediate intensity. There is little correlation between the count rate and the color for steady-state data. Data points from the dipping state falls into two categories. Those from deeper (small) dips occupy distinct vertical stripes in the low intensity side of both color-intensity diagrams (shown as the darkest shade). Those from shallower (small) dips and those from between the small dips (second darkest shade) partially overlap with the steady state data and show an apparent color-intensity anti-correlation. This anti-correlation is more pronounced in the soft colors. The color for these data points are also slightly harder on average than the steady-state data. There is a smooth transition between the steady state data and the shallow-dip data.

In the intensity-color diagrams (Figures 8-4, 8-5), there is a clear difference between the first PCA dip and the second or the third dips. The first dip apparently have failed to reach the low-intensity level in the other two dips. Instead, they are very similar to data from the shallower small dips in those two dips. It is certainly possible that the PCA failed to sample the minimum intensity data points with a 10 day sampling interval. However, the ASM light curve is consistent with the PCA energy fluxes (Figure 8-7) supporting the idea that the first dip is indeed shallower. This is also consistent with the fact that a total of 3–4 dips are missing (or too shallow) in the ASM data at expected times.

8.3.3 Spectral and Timing Evolution

The energy spectra from nine gain epoch-3 PCA observations during dip cycle 1 can be well-fit with a thermal bremsstrahlung spectrum (emission due to the acceleration of electrons by protons or ions in an optically thin plasma cloud) at a plasma temperature (T_b) around 4–6 keV, interstellar absorption with n_H values of 1–7$\times 10^{22}$ cm^{-2}, and a Gaussian line around 6.4 keV (presumably the iron K_α line) (see Table 8-1 for the best-fit parameters). The unabsorbed 2.5–25 keV energy flux ($\sim 10^{-9}$ erg cm^{-2}s^{-1}) indicates that if the system resides within 10 kpc of the earth, the 2.5–25 keV luminosity is less than 10^{37} erg cm^{-2}s^{-1}. With this spectral model, spectra containing hard flares generally exhibit higher plasma temperature (T_b) than that of the steady states. There seems to be increased absorption for the two observations (obs. 8,9) residing at the bottom of the dip compared with a preceding steady-state observation (obs. 7).

Four spectra from the three different states for dip cycle 1 are shown in Figure 8-9. Compared with the steady state data, the flares exhibit excessive photons at energies $\gtrsim 5$ keV. The dip spectra exhibit an increased reduction of the soft flux towards the lower energies.

The evolution of the spectra during dip cycles 2 and 3 are shown in Figures 8-10

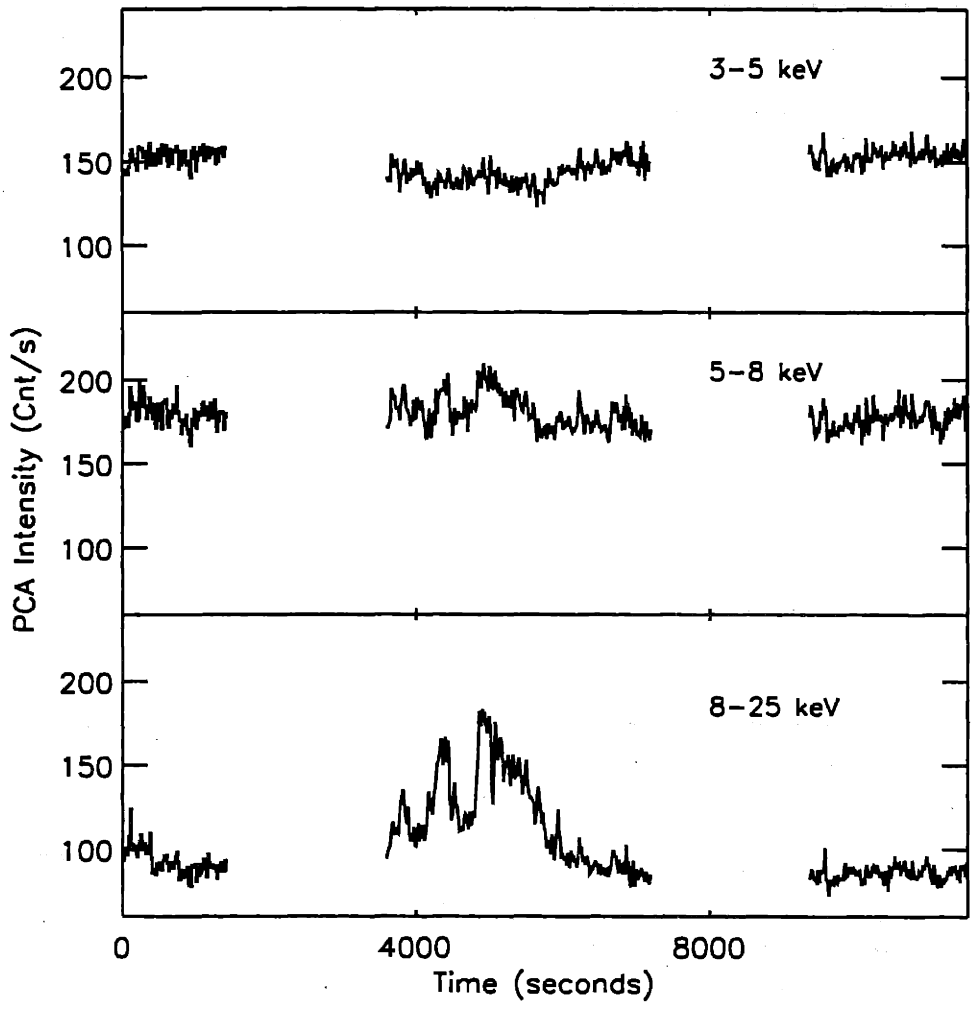

Figure 8-8 Hard flares of XTE J1716-389 observed with *RXTE*/PCA. The flares occurred between 3600 s and 7200 s. Typical steady state data can be seen between 9400 s and 12000 s. The intensity of the system in the 8–25 keV band increased dramatically during the flares.

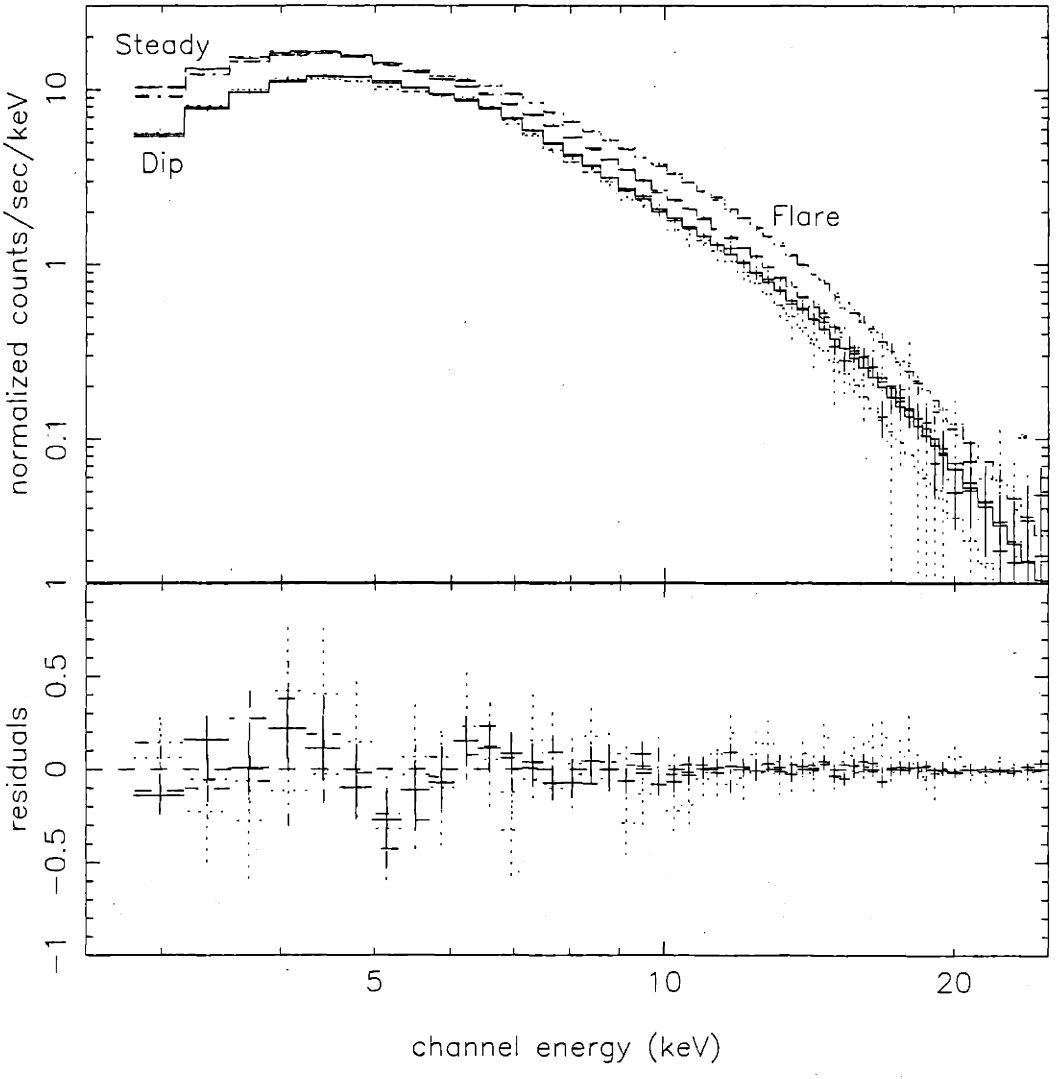

Figure 8-9 Typical spectra for dip cycle 1 (Epoch 3). The best-fit models and the residuals of the fits are also plotted. The four observations at a top-down order (at $\sim$ 15 keV) are observation 2 (dash-dot-dot-dot line, flaring state), 4 (dash line, steady state), 9 (solid line, dipping state), and 8 (dots, dipping state).

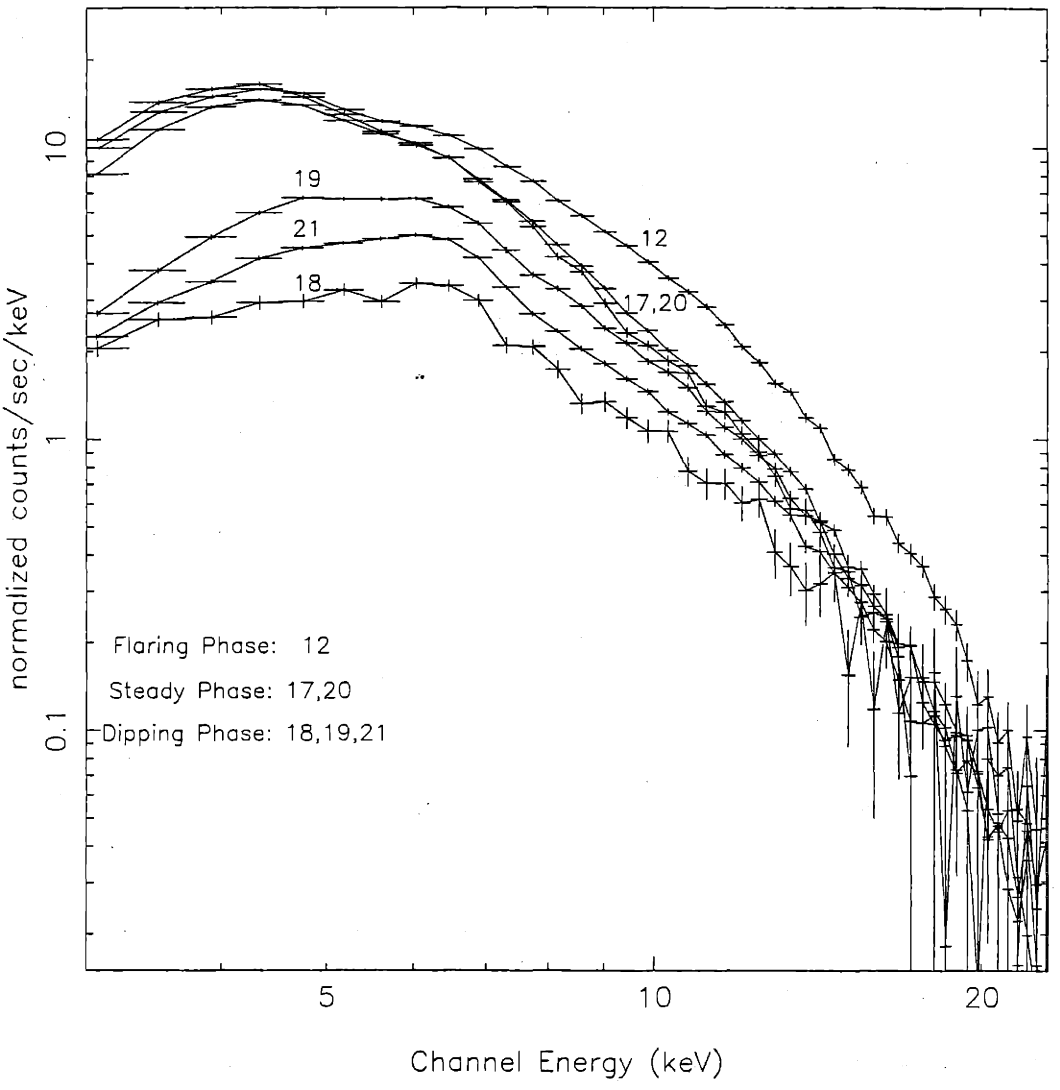

Figure 8-10 Spectral evolution in dip cycle 2. The data points are connected for illustration. The observation sequences and their states are labeled.

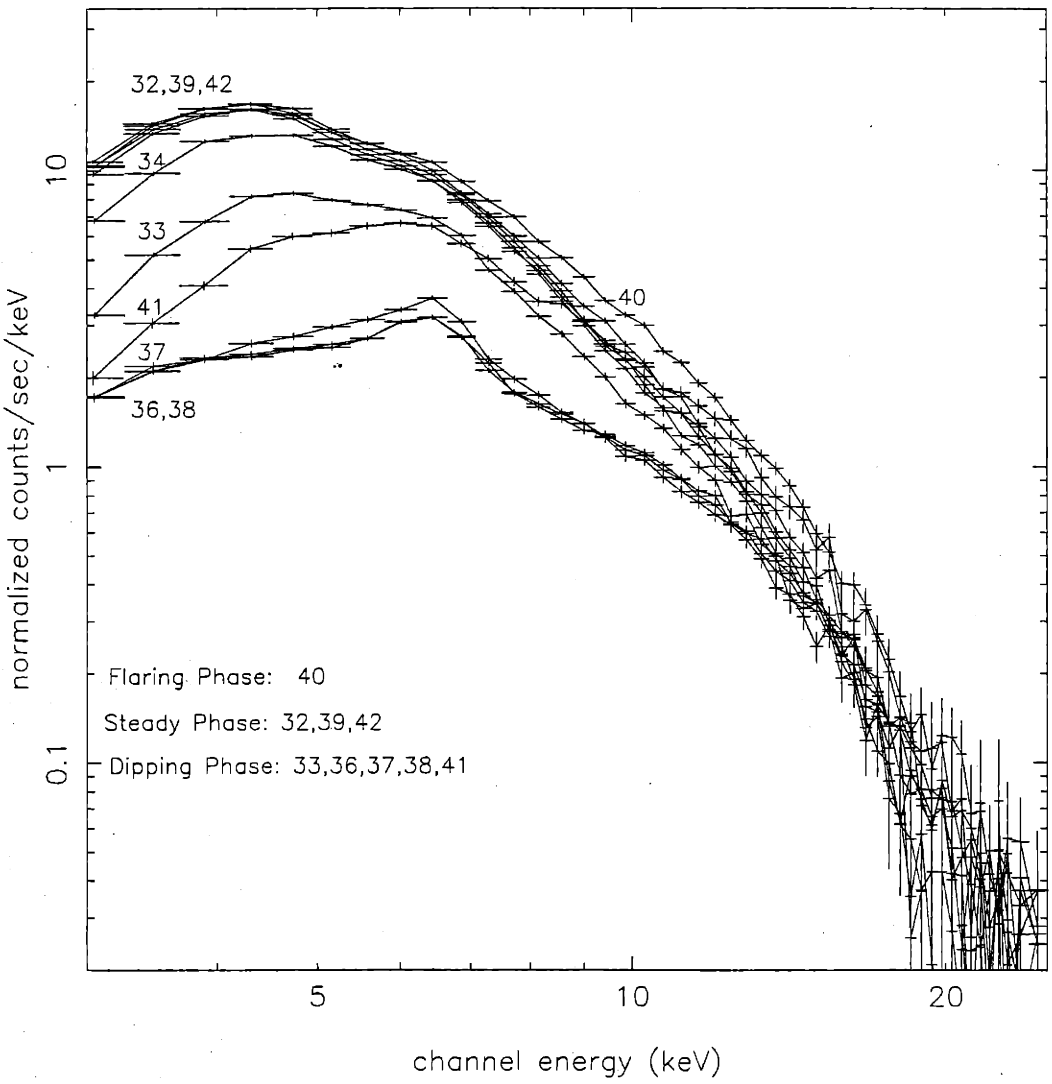

Figure 8-11 Spectral Evolution in dip cycle 3. The data points are connected for illustration. The observation sequences and their states are labeled.

and 8-11. Compared with the steady-state spectra outside the dip, the spectra within the dip exhibit an overall reduced intensity at low energies. At intermediate levels within the dips (e.g., obs. 19, 33, 41), the intensity decreases more rapidly at low energies than at higher energies. This is consistent with absorption by cold materials. However, at the bottom of both the dips 2 and 3 (observations 18, 36, 37, and 38), the system maintains a substantial level of X-ray emission at low energies that is inconsistent with what the same absorption model would predict based on reduction of intensities in 5–12 keV. This bottoming-out of the intensity within the dip at low energies is also seen in the hardness ratio HR1 in the ASM folded light curve (Figure 8-3). The spectra for observations between smaller dips within the broad dips can be very similar to those outside. Some have spectral shapes and intensities similar to those in the steady state (obs. 20, 39) or in the flaring state (obs. 40). Other data points between small dips exhibit intermediate properties (e.g., obs. 34) similar to the steady state data but with slight reduction in the soft photons. In all cases, there is little difference between the intensities of steady-state and the dipping state spectra at energies > 15 keV. The feature of the iron lines become pronounced at lowest broad-band intensity levels.

Fourier power density spectra (PDSs) were computed for every consecutive 1 ks time segment of the count rate for all observations. Each transform used 256 μs timebins and covered the full 2–32 keV energy range. The expected Poisson noise due to counting statistics is subtracted from each PDS. An average PDS for each state was calculated and rebinned logarithmically (Figure 8-12). The PDSs for all states may be characterized by simple power-laws with no significant features. No pulsations have been found in the frequency range of 0.001–2000 Hz. The low-frequency power in the dipping state of dip cycle 2 is reduced. Therefore, there is no fundamental difference in the PDSs in all states.

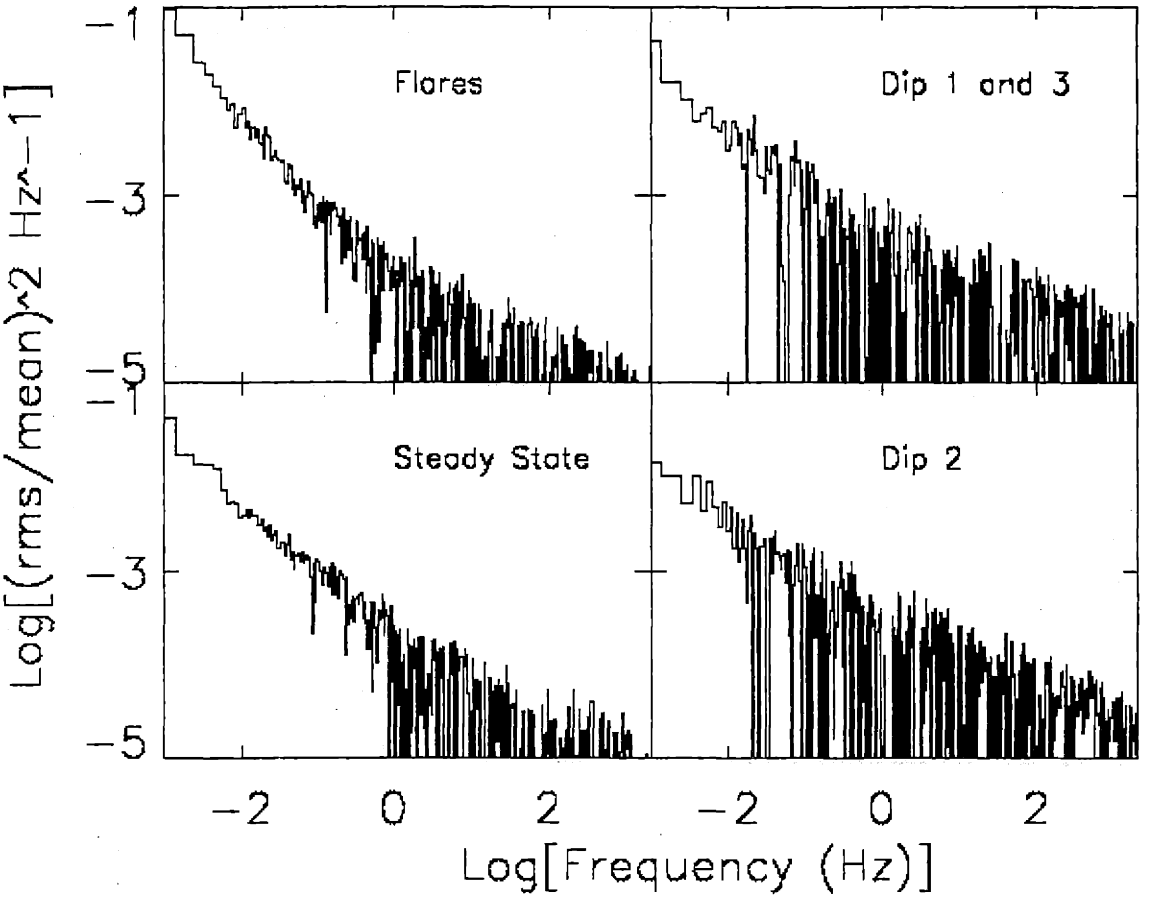

Figure 8-12 Averaged and rebinned power density spectra (2–32 keV) for each observed states. Poisson noise has been subtracted from each PDS. The power density spectra is roughly a power-law. The low-frequency power decreased when the system was inside the dips

8.4 Discussion

The *RXTE*/ASM long-term monitoring of the system XTE J1716-389 establishes that this system has been a persistent X-ray source for the past 4.5 years. The system is likely to be a LMXB because of its characteristic soft thermal bremsstrahlung spectra with a plasma temperature around 6 keV and the lack of any signatures of a HMXB (see Chapter 1). The system likely contains a NS instead of a BHC because of the lack of any signature for a BHC such as fast intensity variability, ultra-soft spectral component, or high-energy power-law tail. The X-rays from this system seem to be highly absorbed ($n_H \sim 10^{22}$ cm^{-2} outside the dip), which could be due to the heavy interstellar absorption in the galactic plane near the direction to the galactic center.

A 98-d period has been firmly established for this source with the 4.5 years of *RXTE*/ASM data and with the *RXTE*/PCA data. The modulation is found to be caused by the periodic appearance of a broad intensity dip, each of which may consist of 2 to 3 smaller sharp dips. Between the smaller dips, the system could regain the same intensity level and spectral shape as when it is outside the broad dip. These broad dips have relatively long duty cycle (40% of the 98-d cycle), abrupt onset and ending time, and large modulations (57% peak-to-peak modulation at 1.5–12 keV). Some dips might be shallower than the others. This is supported by the facts that at least 3 to 5 such broad dips seem to be missing or are very shallow in the ASM light curve at the expected times and that the first dip observed with the PCA is much shallower than the other two (see Figure 8-7).

These intensity dips are probably caused by heavy absorption of the X-rays by some external structures. This can naturally explain the fact that during the transition into (or out of) the broad dips, the PCA spectra exhibit an enhanced absorption (or the reverse behavior). The blockage of X-rays starts and ends at similar phases from cycle to cycle. This is indicated by the individual PCA dip profiles and the sharp ASM average dip profiles. The blocking structure probably consists of several high absorption column density regions that are separated by intervals mostly trans-

parent to the X-rays. Each such absorbing regions could last 5–30 % of the cycle. The locations of the transparent intervals relative to the cycles are apparently not stable as they do not appear in the average ASM dip profile. The blocking structures probably vary in the profiles (e.g. column density, number of transparent intervals) from cycle to cycle. This is may account for those missing (or shallower) dips in the ASM data and that one dip is shallower than the others in the PCA data.

The evolution of the spectra during each dip can be explained naturally by a two-component model for the X-ray emission. Outside the dip, we observe a dominating central component. Within the dip, the bottoming-out of the energy spectra at low energies well above the background suggests the presence of an unblocked faint X-ray component. This component possibly originates from scattering of the radiation from the central component off an extended corona surrounding the NS or a weak stellar wind.

We first consider the possibility that the 98-d period is the orbital period of a binary system. If the system is indeed a LMXB, the persistent X-ray emission would require in general that the companion star fills its Roche lobe. The orbital period would be restricted to be less than 12 days for a main sequence companion star with a mass less than $10M_{\odot}$ [137] in a circular (or nearly circular) binary orbit. Shorter periods would be predicted for He main sequence or a white dwarf companion. A 98-d orbital period would indicate that the companion has a radius much larger than a main sequence star, e.g., a giant. The periodic modulation may be caused by absorption and scatter of X-rays by a stellar wind from the companion. If this is true, this would be the first clear detection of an orbital period > 20 days for a LMXB as the longest known period to date for a LMXB is 17 d (Cir X-1, a possible LMXB). If the system is a HMXB instead, the most likely solution is also a giant with a strong wind.

Disk precession is perhaps a more viable model to explain the 98-d period in XTE J1716-389. The super-orbital modulation in several sources (e.g. Her X-1 and LMC

X-4) has been ascribed to a tilted precessing accretion disk that periodically obscures the line of sight to the X-ray source. In this scenario, the broad intensity dip in XTE J1716-389 is caused by the blockage of a precessing tilted disk. The re-emergence of the X-rays within the dip is perhaps caused by the patchy structures on the disk. It is also possible that the X-rays re-emerge from below the disk. However, this is very unlikely as the phases of the re-emergence of the X-rays is apparently different from cycle to cycle and is not observed in the average profile. In either case, the inclination angle of our line of sight is probably very close to that of the disk but not so low as to yield eclipses by the companion.

Table 8-1. Model Parameters for the Best-fit Spectra of XTE J1716-389 Near Dip 1 (Epoch 3).

			Bremsstrahlung[2]		Guaussian Line[3]			
Obs.	State	n_H[1] (10^{22} cm^{-2})	T_b (keV)	N_b	E_g (keV)	σ_g (keV)	N_g	flux[4]
1	flare	$3.34^{+0.36}_{-0.39}$	$6.00^{+0.18}_{-0.15}$	$0.349^{+0.017}_{-0.019}$	$6.23^{+0.18}_{-0.24}$	$0.978^{+0.219}_{-0.186}$	$4.12^{+1.49}_{-0.99}$	9.32
2	flare	$4.06^{+0.31}_{-0.33}$	$6.20^{+0.14}_{-0.12}$	$0.358^{+0.013}_{-0.014}$	$6.56^{+0.14}_{-0.17}$	$0.919^{+0.201}_{-0.173}$	$3.21^{+0.90}_{-0.66}$	9.54
3	steady	$3.79^{+0.54}_{-0.60}$	$5.41^{+0.22}_{-0.18}$	$0.391^{+0.026}_{-0.029}$	$6.49^{+0.20}_{-0.25}$	$0.819^{+0.247}_{-0.197}$	$3.46^{+1.45}_{-0.94}$	9.09
4	steady	$1.50^{+0.45}_{-0.43}$	$5.69^{+0.31}_{-0.27}$	$0.279^{+0.030}_{-0.028}$	$5.02^{+0.34}_{-0.41}$	$1.68^{+0.22}_{-0.20}$	$15.74^{+5.92}_{-4.25}$	8.54
5	steady	$3.79^{+0.55}_{-0.81}$	$4.77^{+0.27}_{-0.15}$	$0.431^{+0.032}_{-0.052}$	$6.24^{+0.23}_{-0.45}$	$0.84^{+0.38}_{-0.25}$	$3.66^{+2.97}_{-1.17}$	8.62
6	flare	$3.63^{+0.34}_{-0.37}$	$6.05^{+0.16}_{-0.13}$	$0.353^{+0.016}_{-0.017}$	$6.35^{+0.16}_{-0.20}$	$1.02^{+0.19}_{-0.17}$	$4.23^{+1.26}_{-0.90}$	9.41
7	steady	$1.34^{+0.46}_{-0.44}$	$5.41^{+0.27}_{-0.24}$	$0.277^{+0.029}_{-0.027}$	$5.20^{+0.25}_{-0.28}$	$1.57^{+0.16}_{-0.15}$	$15.38^{+4.20}_{-3.32}$	8.19
8	dip	$6.82^{+1.13}_{-2.01}$	$4.38^{+0.58}_{-0.26}$	$0.376^{+0.054}_{-0.097}$	$6.27^{+0.17}_{-0.48}$	$0.579^{+0.547}_{-0.297}$	$3.67^{+4.43}_{-1.23}$	5.91
9	dip	$3.89^{+0.62}_{-0.60}$	$6.17^{+0.49}_{-0.42}$	$0.198^{+0.0289}_{-0.026}$	$5.05^{+0.268}_{-0.30}$	$1.61^{+0.18}_{-0.17}$	$17.80^{+5.11}_{-3.99}$	6.32

[1]Derived from the photo-electric absorption model "wabs" in XSPEC (v. 10)

[2]It refers to the thermal Bremsstrahlung spectrum model "bremss" in XSPEC (v. 10). T_b is the plasma temperature. N_b is the normalization defined as $(3.0 \times 10^{-15}/(4\pi D^2)) \int n_e n_I dV$, where D is the distance to the source (cm) and n_e, n_I are the electron and ion densities (cm^{-3}).

[3]It refers to the Gaussian line profile "gaussian" in XSPEC (v. 10). E_g is the line energy, σ is the line width, N_g is the normalization in units of 10^{-3}photon cm^{-2} s^{-1}.

[4] PCA energy flux (2.5–25 keV) in units of 10^{-10} ergs cm^{-2}s^{-1}.

Note. — The sequential numbers for the observations are the same as those in Figure 8-7. The combined reduced χ^2 is 0.77 for fit to all observations. The errors are derived based on a 90% confidence range for a single parameter in the χ^2-fit.

Chapter 9

Conclusions

This thesis presents results of several investigations of the long-term behavior of galactic X-ray sources using the *RXTE*/ASM and PCA data. I have conducted a global search for periodicities in the *RXTE*/ASM database which have led to a detection of 37 periods with high confidence levels. The detection strategies and a summary of the results are presented in Chapter 4. We then have pursued follow-up investigations of several discoveries we made in the sources Cyg X-1, X 1908+075, and XTE J1716-389. The results of the investigation and implications for each case are presented separately in Chapters 5,6,7, and Chapter 8.

In Chapter 5, we have analyzed over 2 years of *RXTE*/ASM data for the black hole candidate Cygnus X-1. We have detected the 5.6-day orbital period in Lomb-Scargle periodograms of both light curves and hardness ratios when Cyg X-1 was in the hard state. This detection was made with improved sensitivity and temporal coverage compared with previous detections by other X-ray missions. The folded light curves and hardness ratios show a broad intensity dip accompanied by spectral hardening centered on superior conjunction of the X-ray source. The dip has a duration of about 27% of the orbital period and depth ranging from 8% to 23% of the non-dip intensities in three energy bands. Variability on time scales of hours is often evident within the broad dip in the unfolded data. In contrast, no feature at the orbital period is evident

in the periodograms or folded light curves for the soft state. Absorption of X-rays by a stellar wind from the companion star can reproduce the observed X-ray orbital modulations in the hard state. To explain the low orbital modulation in the soft-state data, a reduction of the wind density during the soft state would be required. As an alternative, a partial covering scenario is described which could also account for the lack of the orbital modulation in the soft state.

Using data from the All-Sky Monitor aboard the *Rossi X-ray Timing Explorer* (*RXTE*), we found, in Chapter 6, that the 1.5–12 keV X-ray count rate of Cyg X-1 is, on time scales from 90 seconds to at least 10 days, strongly correlated with the spectral hardness of the source in the soft state, but is weakly anti-correlated with the latter in the hard state. The correlation shows an interesting evolution during the 1996 spectral state transition. The entire episode can be roughly divided into three distinct phases: (1) a 20-d transition phase from the hard state to the soft state, during which the correlation changes from being negative to positive, (2) a 50-d soft state with a steady positive correlation, and (3) a 20-d transition back to the hard state. The pointed *RXTE* observations confirmed the ASM results but revealed new behaviors of the source at energies beyond the ASM pass band. We suggest that physical processes involved are different in the soft state than in the hard state.

In Chapter 7, we investigated a new 4.4-d period we discovered in the ASM light curves of the X-ray source X 1908+075. X 1908+075 is an optically unidentified and highly absorbed X-ray source that appears in early surveys such as Uhuru, OSO-7, Ariel V, HEAO-1, and the EXOSAT Galactic Plane Survey. These surveys measured a source intensity in the range of 2–12 mCrab at 2–10 keV, and the position was localized to $\sim 0.5°$. We use the Rossi X-ray Timing Explorer (*RXTE*) All Sky Monitor (ASM) to confirm our expectation that a particular Einstein IPC detection (1E 1908.4+0730) provides the correct position for X 1908+075. The analysis of the coded mask shadows from the ASM for the position of 1E 1908.4+0730 yields a persistent intensity $\sim$ 8 mCrab (1.5–12 keV) over a 3 year interval beginning in 1996

February. Furthermore, we detect a period of 4.400 ± 0.001 days with a false alarm probability $< 10^{-7}$. The folded light curve is roughly sinusoidal, with an amplitude that is 26% of the mean flux. The X-ray period may be attributed to the scattering and absorption of X-rays through a stellar wind combined with the orbital motion in a binary system. We suggest that X 1908+075 is an X-ray binary with a high mass companion star.

In Chapter 8, we investigated a 98-d period we discovered in the ASM light curves of the X-ray source XTE J1716-389. We have analyzed 4.5 years of RXTE/ASM 2-12 keV light curve and about 300 ks PCA data for this source. The ASM light curve shows the source to have generally persisted at an intensity of ~25 mCrab for about 4.5 years. Despite its relatively low intensity, it exhibits variability, seen as prominent dips in the ASM light curve, which may have an associated period of ~100 days. The intensity in the dips may decrease to less than 10% of the average count rate and the total duration of a dip may be as much as ~40 days. We present the ASM light curve and the PCA spectral and timing behavior of this source. The 98-d period is established. We show the spectral and timing evolution during broad dips. We conclude that the system is likely a LMXB containing a NS. The 98-d period is likely caused by the presence of a precessing tilted accretion disk around the NS.

Bibliography

[1] N. L. Aleksandrovich, V. A. Aref'ev, K. N. Borozdin, R. A. Syunyaev, and G. K. Skinner. Detection of the X-ray sources KS J1748-248 and KS J1716-389 near the galactic center. *Astronomy Letters*, 21:431–434, July 1995.

[2] C. W. Allen. *Astrophysical quantities*. London: University of London, Athlone Press, c1973, 3rd ed., 1973.

[3] M. Balucinska and G. Hasinger. EXOSAT observations of Cygnus X-1 - study of the soft X-ray excess. *Astronomy and Astrophysics*, 241:439–450, January 1991.

[4] S. J. Bell Burnell and L. Chiappetti. A catalogue of X-ray spectra observed with the Ariel V proportional counter (experiment C). *Astronomy and Astrophysics Supplement Series*, 56:415–439, June 1984.

[5] J. M. Blondin, I. R. Stevens, and T. R. Kallman. Enhanced winds and tidal streams in massive X-ray binaries. *The Astrophysical Journal*, 371:684–695, April 1991.

[6] C. T. Bolton. Identifications of Cygnus X-1 with HDE 226868. *Nature*, 235:271, 1972.

[7] C. T. Bolton. Orbital elements and an analysis of models for HDE 226868 = Cygnus X-1. *The Astrophysical Journal*, 200:269–277, September 1975.

[8] S. Bowyer, E. T. Byram, T. A. Chubb, and H. Friedman. Cosmic X-ray sources. *Science*, 147:394–398, 1965.

[9] H. V. Bradt, A. M. Levine, R. A. Remillard, and D. A. Smith. Transients observed with the RXTE All-Sky Monitor. In *Rossi 2000: Astrophysics with the Rossi X-ray Timing Explorer. March 22-24, 2000 at NASA's Goddard Space Flight Center, Greenbelt, MD USA*, page E114, 2000.

[10] H. V. Bradt, R. E. Rothschild, and J. H. Swank. X-ray Timing Explorer mission. *Astronomy and Astrophysics Supplement Series*, 97:355–360, January 1993.

[11] G. Branduardi, K. O. Mason, and P. W. Sanford. Further copernicus X-ray observations of 3u 1700-37. *Monthly Notices of the Royal Astronomical Society*, 185:137–142, October 1978.

[12] C. Brocksopp, A. E. Tarasov, V. M. Lyuty, and P. Roche. An improved orbital ephemeris for Cygnus X-1. *Astronomy and Astrophysics*, 343:861–864, March 1999.

[13] S. Campana, G. Israel, and L. Stella. Evidence for an $\tilde{8}0$ day periodicity in the X-ray transient pulsar XTE J1946+274. *Astronomy and Astrophysics*, 352:L91–L94, December 1999.

[14] J. I. Castor, D. C. Abbott, and R. I. Klein. Radiation-driven winds in of stars. *The Astrophysical Journal*, 195:157–174, January 1975.

[15] D. Chakrabarty, J. M. Grunsfeld, T. A. Prince, L. Bildsten, M. H. Finger, R. B. Wilson, G. J. Fishman, C. A. Meegan, and W. S. Paciesas. Discovery of the orbit of the X-ray pulsar OAO 1657-415. *The Astrophysical Journal Letters*, 403:L33–L37, January 1993.

[16] D. Chakrabarty and E. H. Morgan. The 2 hour orbit of the bursting millisecond X-ray pulsar SAX J1808-3658. Submitted to *Nature*, 1998.

[17] S. Chaty, I. F. Mirabel, P. A. Duc, J. E. Wink, and L. F. Rodriguez. Infrared and millimeter observations of the galactic superluminal source GRS 1915+105. *Astronomy and Astrophysics*, 310:825–830, June 1996.

[18] L. Cominsky, G. W. Clark, F. Li, W. Mayer, and S. Rappaport. Discovery of 3.6-s X-ray pulsations from 4U 0115+63. *Nature*, 273:367–369, June 1978.

[19] R. H. D. Corbet, F. E. Marshall, A. G. Peele, and T. Takeshima. Rossi X-ray Timing Explorer observations of the X-ray pulsar XTE J1855-026: A possible new supergiant system. *The Astrophysical Journal*, 517:956–963, June 1999.

[20] R. H. D. Corbet and A. G. Peele. RXTE observations of the Be star X-ray transient X0726-260 (4U 0728-25): Orbital and pulse periods. *The Astrophysical Journal Letters*, 489:L83, November 1997.

[21] R. H. D. Corbet and A. G. Peele. The orbital period of the Be/neutron star binary RX J0812.4-3114. *The Astrophysical Journal Letters*, 530:L33–L36, February 2000.

[22] R. H. D. Corbet, J. W. Woo, and F. Nagase. The orbit and pulse period of X1538-522 from GINGA observations. *Astronomy and Astrophysics*, 276:52, September 1993.

[23] D. Crampton, J. B. Hutchings, and A. P. Cowley. The supergiant X-ray binary system 2S 0114 + 650. *The Astrophysical Journal*, 299:839–844, December 1985.

[24] D. J. Crary, C. Kouveliotou, J. van Paradijs, F. van der Hooft, D. M. Scott, S. N. Zhang, B. C. Rubin, M. H. Finger, B. A. Harmon, M. van der Klis, and W. H. G. Lewin. 1100 days of BATSE observations of Cygnus X-1. *Astronomy and Astrophysics Supplement Series*, 120:C153, November 1996.

[25] W. Cui. Cygnus X-1 and GRS 1915+105. *The IAU Circular*, 6404:1, May 1996.

[26] W. Cui, W. Chen, and S. N. Zhang. Cygnus X-1: a spinning black hole? In *ASP Conf. Ser. 138: 1997 Pacific Rim Conference on Stellar Astrophysics*, page 75, 1998.

[27] W. Cui, W. A. Heindl, R. E. Rothschild, S. N. Zhang, K. Jahoda, and W. Focke. Rossi X-ray Timing Explorer observation of Cygnus X-1 in its high state. *The Astrophysical Journal Letters*, 474:L57, January 1997.

[28] W. Cui, S. N. Zhang, and W. Chen. Evidence for frame dragging around spinning black holes in X-ray binaries. *The Astrophysical Journal Letters*, 492:L53, January 1998.

[29] W. Cui, S. N. Zhang, W. Focke, and J. H. Swank. Temporal properties of Cygnus X-1 during the spectral transitions. *The Astrophysical Journal*, 484:383, July 1997.

[30] S. R. Davies. An improved test for periodicity. *Monthly Notices of the Royal Astronomical Society*, 244:93–95, May 1990.

[31] J. E. Deeter, P. E. Boynton, S. Miyamoto, S. Kitamoto, F. Nagase, and N. Kawai. Decrease in the orbital period of Hercules X-1. *The Astrophysical Journal*, 383:324–329, December 1991.

[32] J. E. Deeter, P. E. Boynton, N. Shibazaki, S. Hayakawa, F. Nagase, and N. Sato. Pulse-timing study of Vela X-1 based on Hakucho and Tenma data - 1980-1984. *The Astronomical Journal*, 93:877–889, April 1987.

[33] H. Delgado-Marti, Levine A. M., E. Pfahl, and S. A. Rappaport. The orbit of X Per and its neutron star companion. Submitted to *apj*, 2000. astro-ph/0004258.

[34] T. di Matteo, A. Celotti, and A. C. Fabian. Magnetic flares in accretion disc coronae and the spectral states of black hole candidates: the case of GX 339-4. *Monthly Notices of the Royal Astronomical Society*, 304:809–820, April 1999.

[35] J. B. Dove, J. Wilms, M. Maisack, and M. C. Begelman. Self-consistent thermal accretion disk corona models for compact objects. *The Astrophysical Journal*, 487:759, October 1997.

[36] K. Ebisawa, Y. Ueda, H. Inoue, Y. Tanaka, and N. E. White. ASCA observations of the iron line structure in Cygnus X-1. *The Astrophysical Journal*, 467:419, August 1996.

[37] A. A. Esin, R. Narayan, W. Cui, J. E. Grove, and S. N. Zhang. Spectral transitions in Cygnus X-1 and other black hole X-ray binaries. *The Astrophysical Journal*, 505:854–868, October 1998.

[38] M. H. Finger. Cited in PhD thesis: Hard X-ray Detection and Timing of Accretion-Powered Pulasars with BATSE (1995) by Chakrabarty, D. 1993.

[39] W. Forman, C. Jones, L. Cominsky, P. Julien, S. Murray, G. Peters, H. Tananbaum, and R. Giacconi. The fourth UHURU catalog of X-ray sources. *The Astrophysical Journal Supplement Series*, 38:357–412, December 1978.

[40] D. B. Friend and J. I. Castor. Radiation-driven winds in X-ray binaries. *The Astrophysical Journal*, 261:293–300, October 1982.

[41] R. Giacconi. Scorpius X-1. *Monthly Notices of the Royal Astronomical Society*, 9:L439, 1962.

[42] R. Giacconi, H. Gursky, E. Kellogg, R. Levinson, E. Schreier, and H. Tananbaum. Further X-ray observations of her X-1 from UHURU. *The Astrophysical Journal*, 184:227, August 1973.

[43] R. Giacconi, E. Kellogg, P. Gorenstein, H. Gursky, and H. Tananbaum. An X-ray scan of the galactic plane from UHURU. *The Astrophysical Journal Letters*, 165:L27, April 1971.

[44] M. Gierlinski, A. A. Zdziarski, C. Done, W. N. Johnson, K. Ebisawa, Y. Ueda, F. Haardt, and B. F. Phlips. Simultaneous X-ray and Gamma-Ray observations of Cygnus X-1 in the hard state by GINGA and OSSE. *Monthly Notices of the Royal Astronomical Society*, 288:958–964, July 1997.

[45] M. Gierliński, A. A. Zdziarski, J. Poutanen, P. S. Coppi, K. Ebisawa, and W. N. Johnson. Radiation mechanisms and geometry of Cygnus X-1 in the soft state. *Monthly Notices of the Royal Astronomical Society*, 309:496–512, October 1999.

[46] D. R. Gies and C. T. Bolton. The optical spectrum of HDE 226868 = Cygnus X-1. I - radial velocities and orbital elements. *The Astrophysical Journal*, 260:240–248, September 1982.

[47] D. R. Gies and C. T. Bolton. The optical spectrum of HDE 226868 = Cygnus X-1. II - spectrophotometry and mass estimates. *The Astrophysical Journal*, 304:371–393, May 1986.

[48] D. R. Gies and C. T. Bolton. The optical spectrum of HDE 226868=Cygnus X-1. III. a focused stellar wind model for He II λ 4686 emission. *The Astrophysical Journal*, 304:389, May 1986.

[49] T. A. Hall, J. P. Finley, R. H. D. Corbet, and R. C. Thomas. RXTE observations of the X-ray binary 2S 0114+650. *The Astrophysical Journal*, 536:450–454, June 2000.

[50] J. Heise, R. Mewe, A. C. Brinkman, A. den Boggende, J. Schrijver, E. Gronenschild, D. Parsignault, J. Grindlay, E. Schreier, and H. Schnopper. X-ray observations of Cyg X-1 with ans. *Nature*, 256:107, July 1975.

[51] J. Heise and F. Verbunt. Ultraviolet observations of ÄM Her. *Astronomy and Astrophysics*, 189:112–118, January 1988.

[52] A. Herrero, R. P. Kudritzki, R. Gabler, J. M. Vilchez, and A. Gabler. Fundamental parameters of galactic luminous OB stars. II. a spectroscopic analysis of HDE 226868 and the mass of Cygnus X-1. *Astronomy and Astrophysics*, 297:556, May 1995.

[53] S. S. Holt, E. A. Boldt, L. J. Kaluzienski, and P. J. Serlemitsos. Observations of a new transition in the emission from Cyg X-1. *Nature*, 256:108, July 1975.

[54] S. S. Holt, L. J. Kaluzienski, E. A. Boldt, and P. J. Serlemitsos. A return to the pre-1971 intensity level and a 5.6-d modulation for Cyg X-1. *Nature*, 261:213–215, May 1976.

[55] S. S. Holt, L. J. Kaluzienski, E. A. Boldt, and P. J. Serlemitsos. Long-term studies with the Ariel 5 ASM. II - the strong Cygnus sources. *The Astrophysical Journal*, 233:344–349, October 1979.

[56] J. H. Horne and S. L. Baliunas. A prescription for period analysis of unevenly sampled time series. *The Astrophysical Journal*, 302:757–763, March 1986.

[57] X. M. Hua, D. Kazanas, and W. Cui. Probing the structure of accreting compact sources through X-ray time lags and spectra. *The Astrophysical Journal*, 512:793–803, February 1999.

[58] S. Ichimaru. Bimodal behavior of accretion disks - theory and application to Cygnus X-1 transitions. *The Astrophysical Journal*, 214:840–855, June 1977.

[59] S. A. Ilovaisky, M. Auriere, L. Koch-Miramond, C. Chevalier, J. . Cordoni, and R. A. Crowe. The 17.1-h optical and X-ray orbital period of AC 211/X 2127 + 119 in M15. *Astronomy and Astrophysics*, 270:139–150, March 1993.

[60] S. A. Ilovaisky, C. Chevalier, C. Motch, M. Pakull, J. van Paradijs, and J. Lub. LMC X-4 - the optical 30-day cycle and its implications. *Astronomy and Astrophysics*, 140:251–258, November 1984.

[61] G. L. Israel and L. Stella. A new technique for the detection of periodic signals in "colored" power spectra. *The Astrophysical Journal*, 468:369, September 1996.

[62] K. Jahoda, J. H. Swank, A. B. Giles, M. J. Stark, T. Strohmayer, W. Zhang, and E. H. Morgan. In-orbit performance and calibration of the Rossi X-ray Timing Explorer (RXTE) proportional counter array (PCA). *Proc. SPIE*, 2808:59–70, October 1996.

[63] P. C. Joss and S. Rappaport. Highly compact binary X-ray sources. *Astronomy and Astrophysics*, 71:217–220, January 1979.

[64] T. R. Kallman and R. McCray. X-ray nebular models. *The Astrophysical Journal Supplement Series*, 50:263–317, December 1982.

[65] J. L. Katz. *Nature Phys. Sci.*, 246:87, 1973.

[66] J. C. Kemp, M. S. Barbour, G. D. Henson, D. J. Kraus, I. G. Nolt, J. V. Radostitz, W. C. Priedhorsky, J. Terrell, and E. N. Walker. Cygnus X-1 - optical variation on the 294 day X-ray period. *The Astrophysical Journal Letters*, 271:L65–L68, August 1983.

[67] S. Kitamoto, S. Miyamoto, Y. Tanaka, T. Ohashi, Y. Kondo, Y. Tawara, and M. Nakagawa. Transient dips of Cygnus X-1 observed from Tenma. *Publications of the Astronomical Society of Japan*, 36:731–740, 1984.

[68] M. Lampton, B. Margon, and S. Bowyer. Parameter estimation in X-ray astronomy. *The Astrophysical Journal*, 208:177–190, August 1976.

[69] F. L. Lang, A. M. Levine, M. Bautz, S. Hauskins, S. Howe, F. A. Primini, W. H. G. Lewin, W. A. Baity, F. K. Knight, R. E. Rotschild, and J. A. Petterson. Discovery of a 30.5 day periodicity in LMC X-4. *The Astrophysical Journal Letters*, 246:L21–L25, May 1981.

[70] K. R. Lang. *Astrophysical Data I. Planets and Stars.* Springer-Verlag Berlin Heidelberg New York, 1992.

[71] J. Lasala, P. A. Charles, R. A. D. Smith, M. Balucinska-Church, and M. J. Church. The orbital period of HDE 226868/Cyg X-1. *Monthly Notices of the Royal Astronomical Society*, 301:285–288, November 1998.

[72] D. A. Leahy and A. G. Ananth. Detection of Infrared variability in Cygnus X - 1. *Monthly Notices of the Royal Astronomical Society*, 256:39P–42P, May 1992.

[73] D. A. Leahy, W. Darbro, R. F. Elsner, M. C. Weisskopf, P. G. Sutherland, S. Kahn, and J. E. Grindlay. On searches for pulsed emission with application to four globular cluster X-ray sources: NGC 1851, 6441, 6624, and 6712. *The Astrophysical Journal*, 266:160–170, 1983.

[74] A. Levine, S. Rappaport, J. E. Deeter, P. E. Boynton, and F. Nagase. Discovery of orbital decay in SMC X-1. *The Astrophysical Journal*, 410:328–341, June 1993.

[75] A. Levine, S. Rappaport, A. Putney, R. Corbet, and F. Nagase. LMC X-4 - GINGA observations and search for orbital period changes. *The Astrophysical Journal*, 381:101–109, November 1991.

[76] A. M. Levine, H. Bradt, W. Cui, J. G. Jernigan, E. H. Morgan, R. Remillard, R. E. Shirey, and D. A. Smith. First results from the All-Sky Monitor on the Rossi X-ray Timing Explorer. *The Astrophysical Journal*, 469:L33–L36, 1996.

[77] A. M. Levine and J. G. Jernigan. On the orbital phase dependence of the turn-on times of Hercules X-1. *The Astrophysical Journal*, 262:294–300, November 1982.

[78] A. M. Levine, S. A. Rappaport, and G. Zojcheski. Orbital decay in LMC X-4. *The Astrophysical Journal*, 541:194–202, September 2000.

[79] W. G. H. Lewin, J. van Paradijs, and E. P. J. van den Heuvel, editors. *X-ray Binaries*. Number 26 in Cambridge Astrophysics Series. Cambridge University Press, Cambridge, 1995.

[80] W. H. G. Lewin, J. van Paradijs, and M. van der Klis. A review of quasi-periodic oscillations in low-mass X-ray binaries. *Space Science Reviews*, 46:273–378, 1988.

[81] T. P. Li, Y. X. Feng, and L. Chen. Temporal and spectral correlations of Cygnus X-1. *The Astrophysical Journal*, 521:789–797, August 1999.

[82] E. P. Liang and P. L. Nolan. Cygnus X-1 revisited. *Space Science Reviews*, 38:353–384, August 1984.

[83] N. R. Lomb. Least-squares frequency analysis of unequally spaced data. *The Astrophysical Journal*, 39:447–462, 1976.

[84] K. S. Long, G. A. Chanan, and R. Novick. The X-ray polarization of the Cygnus sources. *The Astrophysical Journal*, 238:710–716, June 1980.

[85] K. Makishima, N. Kawai, K. Koyama, N. Shibazaki, F. Nagase, and M. Nakagawa. Discovery of a 437.5-s X-ray pulsation from 4U 1907 + 09. *Publications of the Astronomical Society of Japan*, 36:679–689, 1984.

[86] B. Margon, S. A. Grandi, R. P. S. Stone, and H. C. Ford. Enormous periodic doppler shifts in SS 433. *The Astrophysical Journal Letters*, 233:L63–L68, October 1979.

[87] T. H. Markert, C. R. Canizares, G. W. Clark, W. H. G. Lewin, H. W. Schnopper, and G. F. Sprott. Observations of the highly variable X-ray source GX 339-4. *The Astrophysical Journal Letters*, 184:L67, September 1973.

[88] T. H. Markert, F. N. Laird, G. W. Clark, D. R. Hearn, G. F. Sprott, F. K. Li, H. V. Bradt, W. H. G. Lewin, H. W. Schnopper, and P. F. Winkler. The MIT/OSO 7 catalog of X-ray sources - intensities, spectra, and long-term variability. *The Astrophysical Journal Supplement Series*, 39:573–632, April 1979.

[89] K. O. Mason, P. Seitzer, I. R. Tuohy, L. K. Hunt, J. Middleditch, J. E. Nelson, and N. E. White. A 5.57 hr modulation in the optical counterpart of 2S 1822-371. *The Astrophysical Journal Letters*, 242:L109–L113, December 1980.

[90] T. Matsuda, M. Inoue, and K. Sawada. Spin-up and spin-down of an accreting compact object. *Monthly Notices of the Royal Astronomical Society*, 226:785–811, June 1987.

[91] M. Milgrom. On the nature of the galactic bulge X-ray sources. *Astronomy and Astrophysics*, 67:L25–L28, July 1978.

[92] E. H. Morgan, R. A. Remillard, and J. Greiner. RXTE observations of QPOs in the black hole candidate GRS 1915+105. *The Astrophysical Journal*, 482:993–1010, 1997.

[93] R. Morrison and D. McCammon. Interstellar photoelectric absorption cross sections, 0.03-10 kev. *The Astrophysical Journal*, 270:119–122, July 1983.

[94] M. Oda. Cyg X-1 - a candidate of the black hole. *Space Science Reviews*, 20:757–813, September 1977.

[95] M. Oda. Cygnus X-1. *The IAU Circular*, 3491:2, July 1980.

[96] M. Oda. Cygnus X-1. *The IAU Circular*, 3502:2, August 1980.

[97] J. A. Orosz and C. D. Bailyn. Optical observations of GRO J1655-40 in quiescence. I. a precise mass for the black hole primary. *The Astrophysical Journal*, 477:876, March 1997.

[98] J. M. Paredes, J. Marti, M. Peracaula, and M. Ribo. Evidence of X-ray periodicity in LSI+61°303. *Astronomy and Astrophysics*, 320:L25–L28, April 1997.

[99] A. N. Parmar, A. P. Smale, F. Verbunt, and R. H. D. Corbet. The orbital ephemeris and eclipse transitions of the low-mass X-ray binary EXO 0748 - 676. *The Astrophysical Journal*, 366:253–260, January 1991.

[100] A. N. Parmar, N. E. White, P. Giommi, and M. Gottwald. The discovery of 3.8 hour periodic intensity dips and eclipses from the transient low-mass X-ray binary EXO 0748-676. *The Astrophysical Journal*, 308:199–212, September 1986.

[101] G. G. Pooley, R. P. Fender, and C. Brocksopp. Orbital modulation and longer term variability in the radio emission from Cygnus X-1. *Monthly Notices of the Royal Astronomical Society*, 302:L1–L5, January 1999.

[102] J. Poutanen, J. H. Krolik, and F. Ryde. The nature of spectral transitions in accreting black holes - the case of Cyg X-1. *Monthly Notices of the Royal Astronomical Society*, 292:L21–L25, November 1997.

[103] S. H. Pravdo, N. E. White, R. H. Becker, Y. Kondo, E. A. Boldt, S. S. Holt, P. J. Serlemitsos, and G. E. McCluskey. X-ray and Ultraviolet spectroscopy of Cygnus X-1 = HDE 226868. *The Astrophysical Journal Letters*, 237:L71–L75, May 1980.

[104] W. H. Press, S. A. Teukolsky, W. T. Vetterling, and B. P. Flannery. *Numerical Recipes in C. The Art of Scientific Computing.* Cambridge: University Press, 1992, 2nd ed., 1992.

[105] W. Priedhorsky and J. Terrell. Discovery of a 176 day period in 4U 1820-30. *The Astrophysical Journal Letters*, 284:L17–L20, September 1984.

[106] W. C. Priedhorsky, S. Brandt, and N. Lund. Time series analysis of bright galactic X-ray sources. *Astronomy and Astrophysics*, 300:415, August 1995.

[107] W. C. Priedhorsky and J. Terrell. Long-term X-ray observations of Cen X-3, GX 301-2 (4U 1223-62), GX 304-1 (4U 1258-61) and 4U 1145-61. *The Astrophysical Journal*, 273:709–715, October 1983.

[108] W. C. Priedhorsky and J. Terrell. Long-term observations of X-ray sources - the Aquila-Serpens-Scutum region. *The Astrophysical Journal*, 280:661–670, May 1984.

[109] W. C. Priedhorsky, J. Terrell, and S. S. Holt. Evidence for an about 300 day period in Cygnus X-1. *The Astrophysical Journal*, 270:233–238, July 1983.

[110] S. Rappaport, G. W. Clark, L. Cominsky, F. Li, and P. C. Joss. Orbital elements of 4U 0115+63 and the nature of the hard X-ray transients. *The Astrophysical Journal Letters*, 224:L1–L4, August 1978.

[111] R. A. Remillard and C. R. Canizares. SAS 3 observations of Cygnus X-1 - the intensity dips. *The Astrophysical Journal*, 278:761–768, March 1984.

[112] R. A. Remillard and A. M. Levine. The RXTE All Sky Monitor: First year of performance. In *All-Sky X-ray Observations in the Next Decade*, page 29, 1997.

[113] R. A. Remillard, E. H. Morgan, J. E. McClintock, C. D. Bailyn, and J. A. Orosz. RXTE observations of 0.1-300 HZ quasi-periodic oscillationsin the microquasar GRO J1655-40. *The Astrophysical Journal*, 522:397–412, September 1999.

[114] C. R. Robinson, B. A. Harmon, M. L. McCollough, and et al. Long-term variability in bright hard X-ray sources: 5 + years of BATSE data. In *The Transparent Universe*, page 249, 1997.

[115] M. Ruffert. Non-axisymmetric wind-accretion simulations. I. velocity gradients of 3% and 20% over one accretion radius. *Astronomy and Astrophysics*, 317:793–814, February 1997.

[116] P. W. Sanford, J. C. Ives, S. J. B. Burnell, K. O. Mason, and P. Murdin. Ariel V and Copernicus measurements of the X-ray variability of Cyg X-1. *Nature*, 256:109–111, July 1975.

[117] N. Sato, F. Nagase, N. Kawai, R. L. Kelley, S. Rappaport, and N. E. White. Orbital elements of the binary X-ray pulsar GX 301-2. *The Astrophysical Journal*, 304:241–248, May 1986.

[118] B. D. Savage and J. S. Mathis. Observed properties of interstellar dust. *Annual Review of Astronomy and Astrophysics*, 17:73–111, 1979.

[119] J. D. Scargle. Studies in astronomical time series analysis. II - statistical aspects of spectral analysis of unevenly spaced data. *The Astrophysical Journal*, 263:835–853, December 1982.

[120] A. P. Smale and J. C. Lochner. Long-term variability in low-mass X-ray binaries - a study using data from Vela 5B. *The Astrophysical Journal*, 395:582–591, August 1992.

[121] D. A. Smith, A. M. Levine, H. V. Bradt, R. Remillard, J. G. Jernigan, K. C. Hurley, L. Wen, M. Briggs, T. Cline, E. Mazets, S. Golenetskii, and D. Frederics. Localizations of 13 Gamma-ray bursts by the All-Sky Monitor on the Rossi X-ray Timing Explorer. *The Astrophysical Journal*, 526:683–696, December 1999.

[122] R. T. Stewart, G. J. Nelson, W. Penninx, S. Kitamoto, S. Miyamoto, and G. D. Nicolson. On the puzzling nature of the X-ray binary Circinus X-1. *Monthly Notices of the Royal Astronomical Society*, 253:212–216, November 1991.

[123] M. T. Stollberg, M. H. Finger, R. B. Wilson, D. M. Scott, D. J. Crary, and W. S. Paciesas. BATSE observations and orbit determination of the Be/X-ray transient EXO 2030+375. *The Astrophysical Journal*, 512:313–321, February 1999.

[124] R. E. Taam and B. A. Fryxell. On nonsteady accretion in stellar wind-fed X-ray sources. *The Astrophysical Journal Letters*, 327:L73–L76, April 1988.

[125] W. H. G. Tanaka, Y. & Lewin. Black-hole binaries. In W. G. H. Lewin, J. van Paradijs, and E. P. J. van den Heuvel, editors, *X-ray Binaries*, pages 126–174. Cambridge University Press, 1995.

[126] Y. Tanaka and N. Shibazaki. X-ray novae. *Annual Review of Astronomy and Astrophysics*, 34:607–644, 1996.

[127] H. Tananbaum, H. Gursky, E. Kellogg, R. Giacconi, and C. Jones. Observation of a correlated X-ray transition in Cygnus X-1. *The Astrophysical Journal Letters*, 177:L5, October 1972.

[128] C. B. Tarter, W. H. Tucker, and E. E. Salpeter. The interaction of X-ray sources with optically thin environments. *The Astrophysical Journal*, 156:943, June 1969.

[129] A. R. Taylor and P. C. Gregory. Two-frequency radio spectra during an outburst of the periodic radio star LSI +61°303. *The Astrophysical Journal*, 283:273–278, August 1984.

[130] L. Titarchuk. Generalized comptonization models and application to the recent high-energy observations. *The Astrophysical Journal*, 434:570–586, October 1994.

[131] A. Treves, L. Chiappetti, E. G. Tanzi, M. Tarenghi, H. Gursky, A. K. Dupree, L. W. Hartmann, J. Raymond, R. J. Davis, and J. Black. Ultraviolet, X-ray, and Infrared observations of HDE 226868 = Cygnus X-1. *The Astrophysical Journal*, 242:1114–1123, December 1980.

[132] H. Tsunemi, S. Kitamoto, S. Okamura, and D. Roussel-Dupre. Discovery of a bright X-ray nova, GS 2000+25. *The Astrophysical Journal Letters*, 337:L81–L84, February 1989.

[133] M. van der Klis. Fourier techniques in X-ray timing. In H. Ogelman and E. P. J. van den Heuvel, editors, *Timing Neutron Stars*, pages 27–69. Kluwer Academic Publishers, 1989.

[134] M. van der Klis. Rapid aperiodic variability in X-ray binaries. In W. G. H. Lewin, J. van Paradijs, and E. P. J. van den Heuvel, editors, *X-ray Binaries*, pages 252–307. Cambridge University Press, 1995.

[135] M. van der Klis. Kilohertz quasiperiodic oscillations in low-mass X-ray binaries. In R. Buccheri and J. van Paradijs, editors, *The Many Faces of Neutron Stars*, page (in press). Dordrecht: Kluwer, 1998.

[136] M. van der Klis and J. M. Bonnet-Bidaud. The X-ray ephemeris of Cygnus X-3. *Astronomy and Astrophysics*, 214:203–208, April 1989.

[137] F. Verbunt and E. P. J. van den Henvel. Formation and evolution of neutron stars and black holes in binaries. In W. G. H. Lewin, J. van Paradijs, and E. P. J. van den Heuvel, editors, *X-ray Binaries*, pages 457–494. Cambridge University Press, 1995.

[138] W. Voges, B. Aschenbach, T. Boller, H. Bräuninger, U. Briel, W. Burkert, K. Dennerl, J. Englhauser, R. Gruber, F. Haberl, G. Hartner, G. Hasinger, M. Kürster, E. Pfeffermann, W. Pietsch, P. Predehl, C. Rosso, J. H. M. M. Schmitt, J. Trümper, and H. U. Zimmermann. The ROSAT all-sky survey bright source catalogue. *Astronomy and Astrophysics*, 349:389–405, September 1999.

[139] E. N. Walker. B and V photometry of Cygnus X-1. *Monthly Notices of the Royal Astronomical Society*, 160:9P, 1972.

[140] R. S. Warwick, N. Marshall, G. W. Fraser, M. G. Watson, A. Lawrence, C. G. Page, K. A. Pounds, M. J. Ricketts, M. R. Sims, and A. Smith. The Ariel V 3 A catalogue of X-ray sources. I - sources at low galactic latitude /absolute value of B less than 10 deg. *Monthly Notices of the Royal Astronomical Society*, 197:865–891, December 1981.

[141] R. S. Warwick, A. J. Norton, M. J. L. Turner, M. G. Watson, and R. Willingale. A survey of the galactic plane with EXOSAT. *Monthly Notices of the Royal Astronomical Society*, 232:551–564, June 1988.

[142] M. G. Watson, R. Willingale, A. R. King, J. E. Grindlay, and J. Halpern. The big dipper - 4U 1624 - 49. *Space Science Reviews*, 40:195–200, February 1985.

[143] B. L. Webster and P. Murdin. *Nature*, 235:37, 1972.

[144] L. Wen, W. Cui, and H. V. Bradt. The correlated intensity and spectral evolution of Cyg X-1 during state transitions. *The Astrophysical Journal Letters*, page in press, 2000.

[145] L. Wen, W. Cui, A. M. Levine, and H. V. Bradt. Orbital modulation of X-rays from Cyg X-1 in its hard and soft states. *The Astrophysical Journal*, 525:968–977, November 1999.

[146] L. Wen, R. A. Remillard, and H. V. Bradt. X1908+075: An X-ray binary with a 4. 4 day period. *The Astrophysical Journal*, 532:1119–1123, April 2000.

[147] N. E. White, R. H. Becker, E. A. Boldt, S. S. Holt, P. J. Serlemitsos, and J. H. Swank. A 5.57 hour modulation of the X-ray flux of 4U 1822-37: A new model for Cyg X-3. *STIN*, 81:20001, January 1981.

[148] N. E. White, F. Nagase, and A. N. Parmar. The properties of X-ray binaries. In W. G. H. Lewin, J. van Paradijs, and E. P. J. van den Heuvel, editors, *X-ray Binaries*, pages 1–49. Cambridge University Press, 1995.

[149] C. A. Wilson, M. H. Finger, B. A. Harmon, D. Chakrabarty, and T. Strohmayer. Discovery of the 198 second X-ray pulsar GRO J2058+42. *The Astrophysical Journal*, 499:820, May 1998.

[150] P. Wojdowski, G. W. Clark, A. M. Levine, J. W. Woo, and S. N. Zhang. Quasi-periodic occultation by a precessing accretion disk and other variabilities of smc X-1. *The Astrophysical Journal*, 502:253, July 1998.

[151] K. S. Wood, J. F. Meekins, D. J. Yentis, H. W. Smathers, D. P. McNutt, R. D. Bleach, H. Friedman, E. T. Byram, T. A. Chubb, and M. Meidav. The HEAO A-1 X-ray source catalog. *The Astrophysical Journal Supplement Series*, 56:507–649, December 1984.

[152] A. A. Zdziarski, L. Wen, and W. S. Paciesas. *The Astrophysical Journal*, 2000. in preparation.

[153] S. N. Zhang, W. Cui, and W. Chen. Black hole spin in X-ray binaries: Observational consequences. *The Astrophysical Journal Letters*, 482:L155, June 1997.

[154] S. N. Zhang, W. Cui, B. A. Harmon, W. S. Paciesas, R. E. Remillard, and J. van Paradijs. The 1996 soft state transition of Cygnus X-1. *The Astrophysical Journal Letters*, 477:L95, March 1997.

[155] S. N. Zhang, C. R. Robinson, and W. Cui. Cygnus X-1. *The IAU Circular*, 6510:1, November 1996.